PHYSICAL PARAMETERS OF NARROW PHOTON BEAMS IN RADIOSURGERY

by

Katharina E. Sixel
Department of Physics
McGill University, Montréal
August, 1990

A Thesis
submitted to the
Faculty of Graduate Studies and Research
in partial fulfillment of the
requirements for the degree of
Master of Science
in
Physics

ABSTRACT

Radiosurgery is a radiation treatment modality in which a high radiation dose (few 1000 cGy) is given to a small volume (few cm^3) within the patient's brain during a single treatment. The main physical characteristics of radiosurgery are narrow circular radiation beams, stringent requirements on the numerical (±2%) and spatial (±1 mm) accuracy of dose delivery to the target and the need for sharp dose fall-offs outside the target volume.

Physical aspects of radiosurgery based on isocentric linear accelerators (linacs) are presented. The equipment and techniques used in the measurement of various radiosurgical beam parameters are discussed. Also discussed is the accuracy of radiation beam delivery to the target, the calculation and measurement of 3-dimensional isodose distributions obtained from circular beams, and the production of cylindrical dose distributions with rectangular beams. It is shown from the physics point-of-view that linac-based radiosurgery is a viable alternative to radiosurgery with the commercially available Gamma unit.

RESUMÉ

La radiochirurgie est une technique de traitement utilisant la radiation par laquelle une grande dose (~1000 cGy) est délivrée en un seul traitement à un petit volume (~cm^3) à l'intérieur du cerveau d'un patient. Les principales caractéristiques physiques de la radiochirurgie sont l'utilisation de faisceaux de radiation de très petits diamètres, une précision numérique (±2%) et spatiale (±1 mm) très rigoureuse de la dose délivrée au volume traité et le besoin d'une chute abrupte de la dose delivré à l'extérieur du volume traité.

Les aspects physiques de la radiochirurgie utilisant sur les accélérateurs linéaires isocentriques sont présentés. L'équipements et les techniques utilisées pour la mesure des différents paramètres associés aux faisceaux de radiation utilisés sont discutées. On discute également de la précision spatiale du faisceau de radiation delivrée au volume traité, le calcul et la mesure de distributions isodoses en trois dimensions obtenues à partir de faisceaux circulaires, et la production de distributions cylindriques de dose à partir de faisceaux rectangulaires. Il est démontré d'un point de vue physique que la radiochirugie par l'accélerateur linéaire est un technique alternative à la radiochirurgie basée sur l'unité Gamma disponible commercialement.

ACKNOWLEDGEMENTS

I sincerely thank Dr. E. B. Podgorsak for offering me this project as well as the position of research assistant, and for his guidance and assistance throughout the course of this work. His vast wealth of experience and knowledge has taught me much. I appreciate his help and direction not only with this particular work, but also with my developement as a member of the scientific community.

I wish to thank Mr. Lajos Palotay for the construction of several tissue equivalent phantoms which I used in taking measurements. I also thank Dr. B. G. Fallone for the use of his computing equipment.

I am grateful to all members of the Medical Physics department at the Montreal General Hospital for numerous and valuable discussions on various aspects of my work. The benefits of working within a community of fellow scientists, engineers and technicians manifested themselves almost daily. In particular, I wish to mention M. Noël Blais who has been most generous with his time, patience and help in response to my sometimes tedious questions.

During the course of this two year program, I received financial assistance from the Physics department at McGill University for the first year of study, and from the Medical Physics department of the Montreal General Hospital for the second. This assistance was much appreciated and I thank both parties sincerely.

TABLE OF CONTENTS

CHAPTER 1

INTRODUCTION

1.1 Introduction

Radiosurgery is an external beam irradiation technique using stereotactic apparatus for accurate target localization within the brain and patient immobilization. Radiation in the form of a narrow diameter photon or heavy charged particle beam is applied in a single high dose to the treatment of brain disease. The initial aim of radiosurgery was to produce necrosis in the intracranial target volume with a very high dose (several thousand cGy) delivered in a single fraction without adversely affecting the surrounding brain tissue. Currently, the radiosurgical doses are somewhat lower (on the order of 2000 cGy) and the aim is to control disease without producing necrosis. The lesions treated are those not amenable to conventional surgery, usually because of their inaccessible location in the brain. By far the most common lesions treated with radiosurgery are inoperable arterio-venous malformations (AVM), although small tumours, such as pituitary adenomas and acoustic neurinomas, are also treated. Lately, attempts have been made to use radiosurgery in small, well circumscribed metastatic brain lesions. With the recent advances in brain imaging and mapping, the role of radiosurgery has expanded to treatment of functional disorders, such as epilepsy and pain.

Radiosurgery is used to selectively destroy small intracranial structures with diameters of several mm to several cm. Given the small size of the target volumes and the high doses involved, the requirements for successful radiosurgery are very stringent with regard to target localization and to dose delivery to the target. The target volume of pathological tissue must be accurately located in 3-dimensions. This is done by means of a stereotactic frame affixed to the patient's skull and through the use of modern imaging techniques, such as computed tomography (CT), magnetic resonance imaging (MRI), and digital subtraction angiography (DSA). The dose delivery to the target volume must be accurate, both spatially and numerically. Finally, the dose fall-off in the regions immediately outside the target volume must be sharp, in order to spare the adjacent, healthy tissue. A variety of modern radiosurgical techniques, used clinically today, meet these requirements. All techniques rely on stereotactic localization techniques to guide a number of well collimated radiation beams onto a pre-determined target.

Radiosurgery was introduced in 1951 by Lars Leksell (1,2) who proposed the use of orthovoltage radiation to produce local destruction of tissue in the target volume. The target was irradiated by 200-300 kVp x rays from a number of different angles to produce a focal effect at the lesion. It soon became evident that radiation in the orthovoltage range was not penetrating enough to give the required rapid dose fall-off outside the target. Cobalt-60 gamma rays, however, are energetic enough for this purpose and a special unit based on 179 focused gamma ray beams was introduced in 1968 by Leksell (3). This unit has later evolved into the commercially available Gamma unit (4) which presently incorporates 201 ^{60}Co sources.

A sharp dose fall-off outside the target volumes can also be achieved with beams of heavy charged particles produced by cyclotrons. The advantages of using heavy charged particles are the sharp collimation of the beam edges and the Bragg peak dose distribution, resulting in relatively low doses outside the target volume even for a small number of beams. This type of radiosurgery was started in the late 1950's in Uppsala by Larsson et al. (5), in Berkeley by Lawrence et al. (6) and later-on in Boston by Kjellberg et al. (7), all using proton beams produced in cyclotrons. More recently, the technique has been extended to heavier ions such as helium and carbon in Berkeley (8).

The high capital and operating costs of Gamma units and cyclotrons, combined with difficulties in accurate target localization, ensured that until recently radiosurgery was available in only a few specialized centers around the world. However, the success rate of radiosurgical treatments over the past three decades has stimulated the search for less expensive and more accessible means of performing radiosurgery. In 1974 Larsson introduced the idea of using isocentric linear accelerators (linacs) as radiation sources in radiosurgery (9). Since the mid 1980's a variety of linac-based radiosurgical techniques have been introduced clinically. All linac techniques require stereotactic frames for target localization, and for patient set-up and immobilization during the treatment.

1.2 Stereotactic frames

The stereotactic frames used in radiosurgery are usually those used for general neurological stereotaxy with minor adaptations. Typical frames are cubical in shape with an orthogonal coordinate system affixed to the structure. They are attached to the patient's head by means of several pins that penetrate the frame's cubic structure diagonally and are held in burr-holes in the skull. The position of points within the head is then related to the coordinate system defined by the frame.

To enable visualization of these structures, the frame must be compatible with modern imaging techniques, such as CT, MRI, and DSA. This implies several design considerations that must be taken into account. Closed electrical loops and ferrous components that would distort the magnetic field must be avoided for MRI. Material that is structurally strong but of low x-ray attenuation coefficient should be chosen to minimize CT artifacts. CT especially is highly suitable for stereotaxy, as it is inherently free of geometric distortions (10), eliminating the need for corrections for differential magnification as needed for MRI.

Accurate location of the imaged section within the frame is accomplished by simultaneously imaging appropriate reference markers usually affixed to the stereotactic frame and referred to as *fiducial markers*. The markers consist of a suitable contrast material fixed in a Z- or N-shape to plates which attach to the frame. During imaging with CT or MRI, at least three Z-shaped marker sets intersect each transverse slice. These three sets define the position of the transverse plane of scan in relationship to the stereotactic frame. The relative positions of the three rods of each Z-marker set define the section position at that point. This allows the third coordinate of any point of interest to be determined with the other two coordinates within the

2-dimensional transverse image plane.

The fiducial marker plates are removed after the patient has been imaged. Once the diagnostic information and target position are obtained, orthogonal acrylic *target localization plates* are attached to the cubical frame structure in the same way as the fiducial marker plates, so that the diagnostic image information on the target position (coordinates of the target center) can be transfered to the stereotactic frame and thus to the patient, and the target subsequently positioned with respect to the radiosurgical beam delivery system. The frame is used to position the target center into the appropriate point on the treatment unit which is the focus of the Gamma unit, point of intersection between the beam central axis and couch rotation on a cyclotron, or the isocenter of a linac. Once the correct treatment position is achieved, the frame is used to immobilize the patient such that the target remains in position for the duration of the treatment.

A variety of commercially available frames are presently used for radiosurgery, most notably the Leksell frame (11), the Brown-Robert-Wells (BRW) stereotactic system (12,13), the Riechert/Mundiger stereotactic system (14,15) and the OBT stereotactic frame (10,16). All frames have essentially the same cubical structure and associated coordinate system. They each incorporate similar target localization principles based on fiducial markers immbedded in a Z-shaped pattern on the plates which are attached to the frame during imaging.

In most techniques patients are treated in a supine position on a treatment couch, although techniques with patients sitting in a treatment chair have also been developed (17,18). The stereotactic frame is immobilized through a direct attachment either to the treatment couch or to a floor stand which is fixed to the pedestal of the couch. The latter method is commonly used on linacs. It is, however, more hazardous since the motions of the couch and floor stand are not connected and any inadvertent motion of the couch could cause a serious injury to the patient. Adjustment of the treatment couch or chair with the stereotactic frame fixed to it will bring the target center to the appropriate treatment point.

An example of a stereotactic frame attached to a patient's head and immobilized through attachment to the treatment couch as used at McGill University is shown in Fig. 1.1. The frame in the picture is the OBT frame which is used clinically at our center. Target localization plates are shown attached to the frame's cubical structure. These plates are removed before the actual treatment begins. The frame, and thus the patient's head and the target volume, are held into position by means of a bracket afixed to the edge of the linac couch. This positioning forces the patient's head to lie beyond the edge of the couch and minimizes interference of the treatment apparatus with the radiation beam.

1.3 Photon treatment techniques

Photon beam radiosurgery is performed either with the Gamma unit or with isocentric linear accelerators. The Gamma unit is commercially available and has been described in detail by several of its users (19, 20). It presently incorporates 201 cobalt-60 sources each with a nominal activity of 1 TBq (~30 Ci). The sources are distributed evenly over a 160°x60° sector of the hemispherical source core. The points of beam entry into the patient's skull during the radiosurgical treatment are shown in Fig. 1.2 (a). The 201 beams are all collimated with a primary collimator and directed towards a common focus with a relatively short source-axis distance (SAD) of ~39.5 cm. The final collimation is achieved with a special helmet containing 201 tungsten collimators and positioned in such a way that the collimators align with the primary collimators when the proper treatment position is reached. The size of these secondary collimators determines the target volume that is treated. The patient is positioned stereotactically with respect to the helmet so that the center of the target volume coincides with the focal spot of the unit when the shutter is opened and the patient is brought into the treatment position. The main advantage of the Gamma unit is its potential for a high spatial precision of dose delivery. This is a result of the

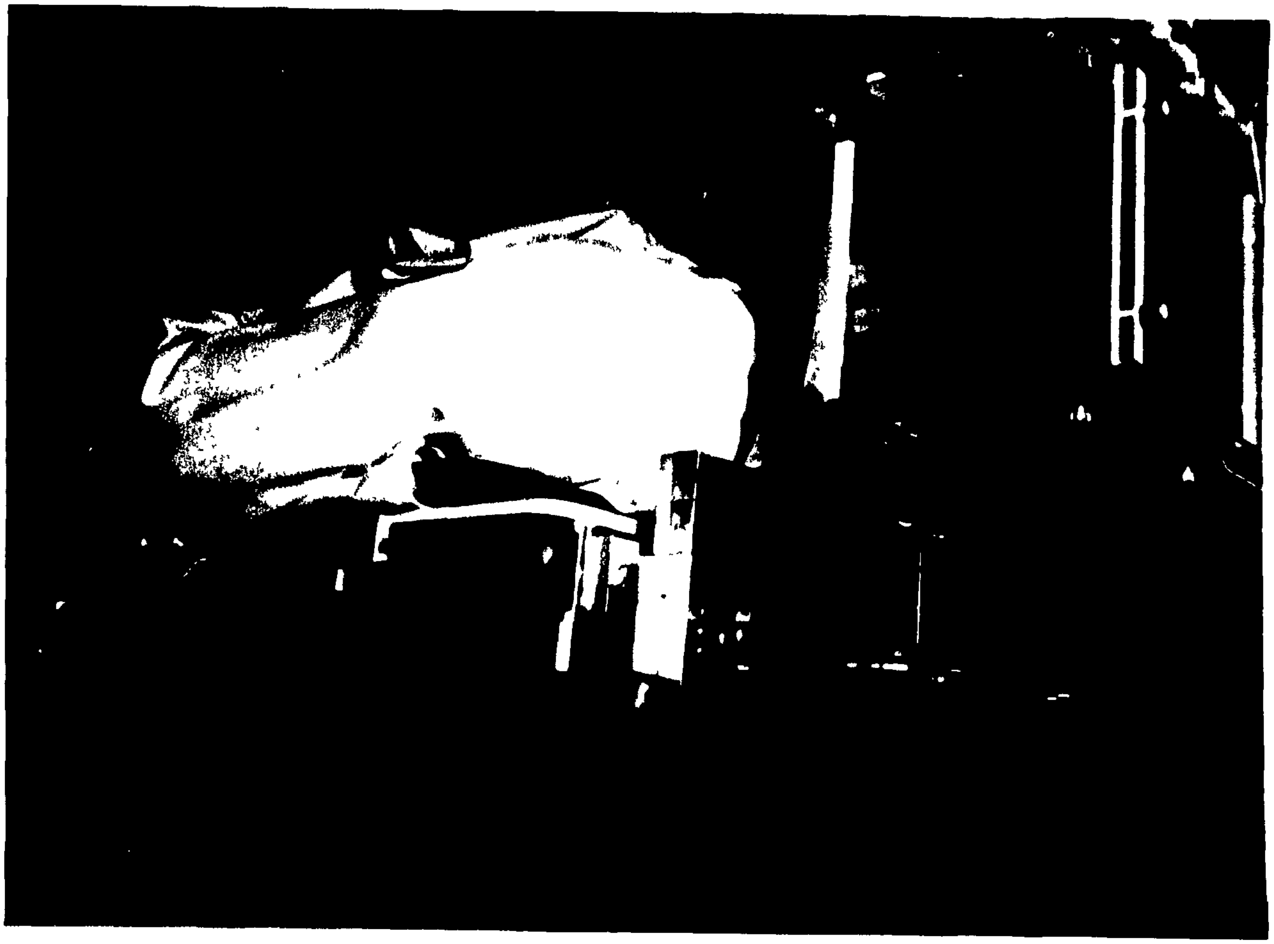

FIGURE 1.1. The OBT stereotactic frame attached to the patient's head and patient positioned onto a linac treatment couch in preparation for radiosurgery. The frame, the head and therefore the target volume are immobilized by means of a bracket fixed to the couch which holds the frame in place. Clearly seen is the frame's cubic structure and the orthogonal coordinate system associated with it. Target localization plates, enabling transfer of diagnostic information to the patient, are shown in place.

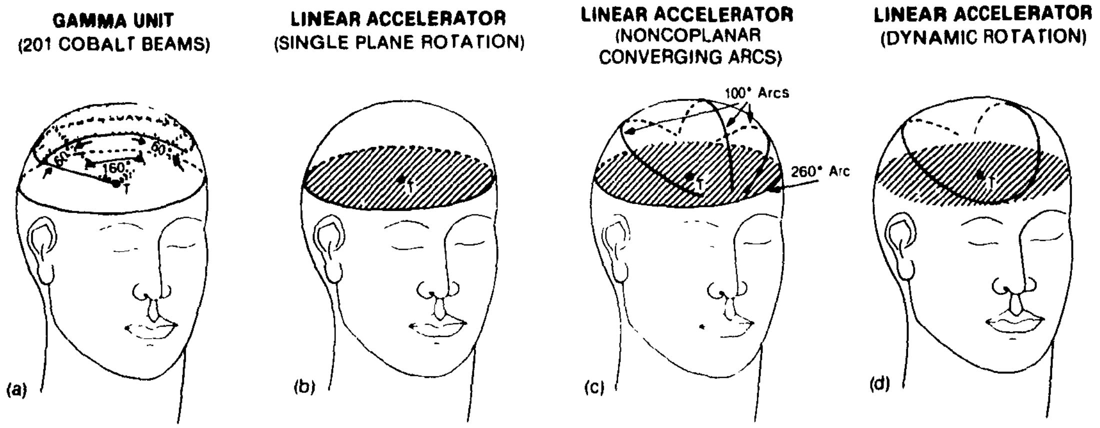

FIGURE 1.2. Points of beam entry into the patient's skull for various radiosurgical techniques: (a) Gamma unit, (b) single plane rotation with a linear accelerator, (c) multiple non-coplanar arcs with a linear acelerator and (d) dynamic rotation with a linear accelerator.

treatment achieved with stationary sources, i.e., there are no moving parts during the treatment. The disadvantages of the Gamma unit are its high capital cost, the high cost of replacing the Co-60 sources periodically and its dedicated application to radiosurgery alone, which preclude a widespread use and general availability.

It has been shown in the past decade that linacs used for standard radiotherapy and may be modified relatively inexpensively for use in radiosurgery. Photon beam radiation fields are usually circular with diameters ranging from 0.5 cm to 3 cm. Additional collimators are generally added to standard collimators in order to achieve the small, well defined circular fields needed for treatment and to minimize the beam penumbra. With the isocentric dose normalized to 100%, a fixed, high percentage isodose surface (typically 90%), which is spherical, is chosen to coincide with the edge of the target volume. The dose fall-off outside the target volume is measured in terms of the distances in which the dose falls from the target edge to lower isodose surfaces, such as 50%, 20% and 10%. The shorter is this distance, the steeper is the dose fall-off outside the target and the more suitable is the technique for radiosurgical procedures. When evaluating a technique for clinical use, the sharpness of dose fall-off as well as the isotropy of the dose distribution must be taken into account, the aim being to have dose fall-offs sharp and ideally of equal sharpness in all directions.

This isotropic dose distribution, of course, could only be achieved with a beam entry distribution over the upper hemisphere approaching the 2π geometry. In practical radiosurgery, only the high level isodose surfaces (e.g., 50% and above) are isotropic, the lower level isodose surfaces become progressively more anisotropic, reflecting particularities of a given treatment technique, resulting because of technical constraints in beam angulation. The isodose distributions may then be characterized by two dose fall-offs: the best (sharpest) and worst (shallowest), with all other fall-offs between the two extremes. The larger the difference between the two dose fall-offs, the worse is the anisotropy of the isodose distribution, and the less applicable is the technique for clinical radiosurgery.

Dose-volume histograms can also be used to characterize the dose fall-offs for a given treatment technique (21). Here, the volume of tissue encompassed by a specified isodose surface is calculated, with a small volume corresponding to a good dose distribution. However, these histograms should be used in conjunction with isodose curves to judge the isotropy of a particular distribution, since directional information is lost.

The linac-based radiosurgical techniques are divided into three main groups: single plane rotation (22), multiple non-coplanar converging arcs (17,23,24), and dynamic rotation (25). When discussing these techniques, we define the angles and planes of gantry and couch rotation, as depicted in Fig. 1.3, with θ representing the gantry angle of rotation in a vertical plane and ϕ representing the couch angle of rotation in a horizontal plane.

Radiosurgery with a *single plane rotation* on a linac is identical to rotational techniques used in conventional radiotherapy. The technique is quite simple, with the couch fixed in a stationary position at $\phi=0°$, and the gantry rotating in a single plane from 0° to 360°. The dose fall-off outside the target in the direction perpendicular to the plane of rotation is very steep, essentially identical to that of a stationary beam. In the plane of rotation (transverse plane), however, the dose fall-off is relatively shallow as a result of the dose superimposition outside the target volume for an infinitely large number of parallel-opposed beams. As shown in Fig. 1.2 (b), the beam entry trace for a full single plane rotation is in a transverse plane and coincides with the beam exit trace.

To improve the dose fall-off obtained with the single plane rotation, Betti and Derechinsky (17), Colombo et al. (23,26), and Hartmann et al. (24,27) have developed the *multiple non-coplanar converging arcs* technique on isocentric linear accelerators. The center of the target is placed stereotactically into the isocenter of the linac, and a series of arcs, each with a different stationary treatment chair (17) or treatment couch (23,24) position, is used to spread the dose outside the target area over as large a volume as possible. To avoid parallel-opposed beams, the arcs are usually kept smaller than 180° and all beam entry points lie in the upper hemisphere,

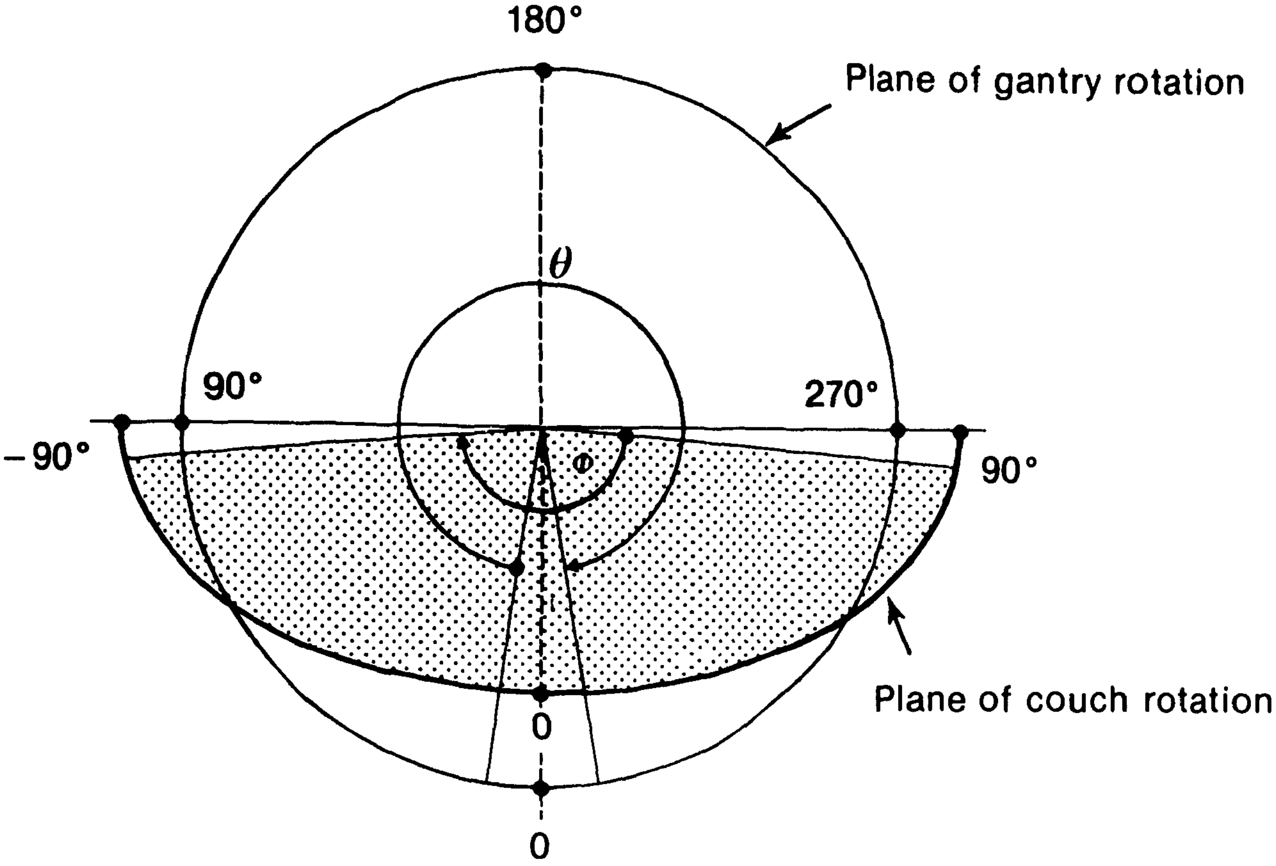

FIGURE 1.3. Angle definitions and rotation directions for the gantry and couch rotation during linac-based radiosurgical procedures. In the single plane rotation, the couch is stationary at 0° and the gantry rotates from 0° to 360°, in the multiple converging arcs techniques a series of arcs is given each with a different stationary couch position, and in the dynamic rotation the gantry and couch rotate simultaneously and continuously, the gantry from 30° to 330° and the couch from 75° to -75°.

while all beam exit points lie in the lower hemisphere.

Hartmann et al. (24,27) perform radiosurgery on a 15 MV linac. Additional circular collimators define fields at the isocenter ranging from 9 mm to 29 mm. Beam diameters are defined at the 50% isodose line, and consequently collimators for treatments are selected based on the ability of this isodose surface to cover the target volume. Dose gradients are then defined in terms of a fall-off from the 50% line. Irradiations in different non-coplanar planes with respect to a target point are achieved by rotating the patient in a horizontal plane on the treatment couch. Eleven 140° arcs of radiation are given while moving the couch by discrete angles. The gantry rotates from 20° to 160° or from 200° to 340° while the couch is positioned at eleven intervals from 90° to -90°.

Recently, Lutz et al. (28,29) have shown that reasonable dose fall-offs can be obtained with as few as four arcs. One 260° arc is given in the transverse plane with the couch fixed at 0°. Three 100° arcs, two from 40° to 140° with the couch first at 90° and then 45°, and one from 220° to 320° with the couch at -45°, are spread over the rest of the head. The additional collimators form fields from 12.5 mm to 30.0 mm diameter defined at the 90% isodose line. This treatment method, chosen as a typical example of the converging arcs technique, is depicted in Fig. 1.2(c).

Dynamic radiosurgery, which was developed by Podgorsak et al. (25,30) at McGill University in Montreal incorporates simultaneous couch and gantry rotations to achieve a steep dose fall-off outside the target volume. The gantry rotates through 300°, from $\theta=30°$ to 330°, while simultaneously the couch rotates through 150°, from $\phi=75°$ to -75° at half the gantry's speed. Thus, for each two degrees of gantry rotation, the couch rotates by one degree. The beam entry trace always lies in the upper hemisphere of the head, implying that all beam exit points lie in the lower hemishere. Thus, although all beams intersect in the target volume and the gantry travels through almost a full circle, the coincidence between an entrance beam and an exit beam, which would degrade the sharpness of the dose fall-off outside the target volume, is avoided for all beams. The resulting beam trace on the patient is shown in

Fig. 1.2 (d). Though the technique appears technically complex, once the continuous couch rotation has been installed, it is relatively simple and efficient to use. In the dynamic rotation used at our center the 90% isodose curve is chosen to coincide with the target volume. Possible beam diameters range from 5 mm to 3.5 mm in steps of 2.5 mm.

An example of a radiosurgical treatment in progress at our center is shown in Fig. 1.4. The patient is lying on the couch with the stereotactic frame attached to her head. The frame, and thus the target with respect to the isocenter, are immobilized by means of the couch bracket. The fiducial marker plates used in target imaging and the target localtization plates used in treatment set-up have been removed to minimize the interference of the stereotactic frame with the radiation beam. The additional collimator needed to produce the small diameter radiosurgical fields is seen fastened in the gantry tray holder. The gantry and couch have been positioned at the initial positions of the dynamic rotation radiosurgery technique, the gantry at 30° and the couch at 75°.

1.4 Thesis outline

We now present a brief outline of the specific aspects of radiosurgery which are discussed in this thesis. Chapter 2, deals with the experimental apparatus and techniques which we used to generate and measure the physical parameters of the radiosurgical photon beams. We first give a brief description of the 10 MV linac, which we use for radiosurgery in our center and then present the characteristics of radiation detectors which we used in the measuring of basic physics data for our radiosurgical beams. Finally, the phantoms used in conjunction with each of the detectors are described.

In Chapter 3 we first discuss the modifications to the linac for use in radiosurgery. The specific clinical set-up, used for radiosurgical treatments and all

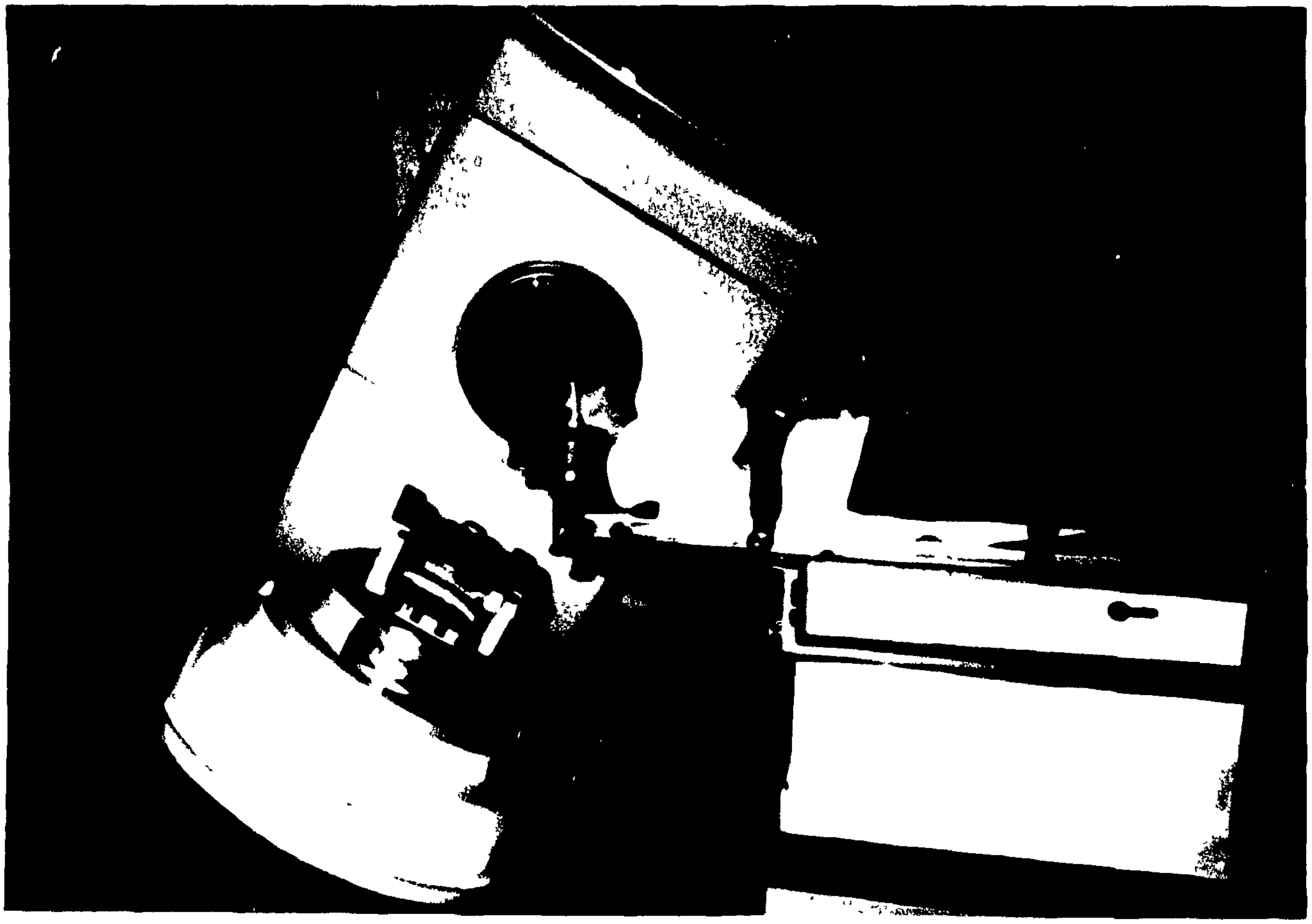

FIGURE 1.4. Example of a radiosurgical treatment in progress. The patient lies in a supine position on the linac couch, with the head hanging over the edge of the couch. The frame, in this case the OBT frame, is immobilized by means of the couch bracket. This ensures immobilization of the target with respect to the linac's isocenter. Both fiducial marker plates and target localization plates have been removed to avoid interference with the radiation beam. The additional radiosurgical collimator is seen in the tray holder of the gantry. Couch and gantry are in the initial positions for the dynamic rotation technique, the gantry at 30°, the couch at 75°.

radiosurgical experiments, is described. The adequacy of this set-up, in terms of spatial accuracy of dose delivery, is addressed. Simple tests show that properly executed linac-based radiosurgery can provide a high degree of spatial accuracy of dose delivery. We then examine the beam measurements required for treatment planning: dose profiles, percentage depth doses and the various factors, such as relative dose factor, scatter factor and collimator factor. These measurements are discussed as influenced by the detector used. A particular effect observed during the measurement of depth doses in the build-up region, a shift in depth of dose maximum with field diameter, is examined in detail, and the cause of the effect is explained.

In Chapter 4 we concern ourselves with actual radiosurgical treatments and dose distributions. The treatment planning system developed and used at McGill is briefly described. The system is capable of determining dose distributions for all photon beam radiosurgical techniques currently in clinical use. Dose distributions are calculated for several linac-based radiosurgical techniques. Comparisons of various techniques are made in terms of isodose contours in three orthogonal planes, and minimum and maximum distances for the dose to decrease from 90% of its maximum value (target edge) to lesser values, such as 50%, 20% and 10% outside the target volume. Results of measurements of actual dose distributions for various radiosurgical techniques are also obtained and the resulting dose distributions compared to distributions calculated for the same treatment parameters.

Recent interest in radiosurgery has focussed on shaping isodose contours, as it has been observed that many volumes to be treated are not spherical but ellipsoidal or even more complex in shape. In Chapter 5, we propose a means for obtaining cylindrical dose distributions in a single treatment. The method is based on rectangular collimators and an additional rotation of the treatment collimator to follow a projected field in the coordinate frame of the treatment couch. By rotating the collimator and by adjusting its longitudinal opening to the projected length of the target volume a cylindrical dose distribution results. We derive this method and present preliminary studies on its viability.

1.5 Summary

In this chapter, we have defined the term radiosurgery and given a brief history of this radiation treatment modality. Originally performed using orthovoltage x rays, the radiation sources for radiosurgery have since evolved to higher energy photon beams as generated by linear accelerators or cobalt-60 sources and heavy charged particle beams. All radiosurgical techniques require stereotactic frames for target localization, patient set-up and immobilization during the treatment. The stereotactic frames, including their target localization principles and immobilization methods were described. We then discussed in some detail various photon beam radiosurgical techniques, specifically the Gamma unit, single plane rotation, multiple non-coplanar converging arcs and the dynamic rotation radiosurgery pioneered at McGill University. Finally, we outlined the specific aspects of radiosurgery that are addressed in this thesis.

1.6 References

1. L. Leksell, **The stereotaxis method and radiosurgery of the brain**, Acta Chir. Scan. **102**: 316-319, 1951.
2. L. Leksell, **Gezielte Hirnoperationen**, in Handbuch der Neurochirurgie, (vol. VI) H. Olivecrona and W. Tonnis, editors. Springer Verlag, New York, 1957, pp.178-218.
3. L. Leksell, **Cerebral radiosurgery I Gamma thalamotomy in two cases of intractable pain**, Acta Chir. Scan. **134**:385-395, 1968.
4. Leksell Gamma unit, Elekta Instrument AB, Stockholm, Sweden.
5. B. Larsson, L. Leksell, B. Rexed, P. Sourander, W. Mair and B. Anderson, **The high energy proton beam as a neurosurgical tool**, Nature **182**: 1222-1223, 1958.
6. J.H. Lawrence, C.A. Tobias, J.L. Born, C. Wang and J.A. Linfoot, **Heavy-particle irradiation in neoplastic and neurologic disease**, J. Neurosurg. **19**: 717-722, 1962.
7. R.N. Kjellberg, A. Sintani, A.G. Frantz and B. Kliman, **Proton beam therapy in acromegaly**, N. Engl. J. Med. **278**: 689-695, 1968.
8. J.I. Fabricant, J.T. Lyman and Y. Hosobuchi, **Stereotactic heavy-ion Bragg peak radiosurgery for intra-cranial vascular disorders: method for treatment of deep arteriovenous malformations**, Brit. J. Radiol. **57**:479-490, 1984.
9. B. Larsson, K. Liden and B. Sarby, **Irradiation of small structures through intact skull**, Acta Radiol. TPB **13**:513-534, 1974.
10. T.M. Peters, J.A. Clark, A. Olivier, A.P. Marchand, G. Mawko, M. Dieumegarde, L. V. Muresan, R. Ethier, **Integrated stereotaxic imaging with CT, MR imaging and Digital Subtraction Angiography**, Radiology **161**:821-826, 1986.
11. Leksell stereotactic frame, Elekta Instrument AB, Stockholm, Sweden.

12. Brown-Robert-Wells stereotactic frame, Radionics Inc., Burlington, MA.
13. R.L. Siddon and N.H. Barth, **Stereotaxis localization of intracranial targets**, Int. J. Radiat. Oncol. Biol. Phys. **13**:1241-1246, 1987.
14. Riechert/Mundinger stereotactic frame, Fischer, Freiburg, W. Germany.
15. O. Pastyr, G.H. Hartmann, W. Schlegel, S. Schabbert, H. Treuer, W.J. Lorenz and V. Sturm, **Stereotactically guided convergent beam irradiation with a linear accelerator: localization-technique**, Acta Neurochir. (Wien) **99**:61-64, 1989.
16. OBT stereotactic frame, Tipal Instruments, Montréal, Québec.
17. O.O. Betti, and V.E. Derchinsky, **Hyperselective encephalic irradiation with linear accelerator**, Acta Neurochir. **33**:385-390, 1984.
18. P.H. McGinley, E.K. Butker, I.R. Crodker and J.C. Landry, **A patient rotator for stereotactic radiosurgery**, Phys. Med. Biol. **35**:649-657, 1990.
19. H. Dahlin, and B. Sarby, **Destruction of small intracranial tumours with ^{60}Co gamma irradiation**, Acta Radiol. TPB **14**: 209-227, 1975.
20. L. Walton, C.K. Bomford and D. Ramsden, **The Sheffield stereotactic radiosurgery unit: physical characteristics and principles of operation**, Brit. J. Radiol. **60**: 897-906, 1987.
21. M.H. Phillips, K.A. Frankel, J.T. Lyman, J.I. Fabrikant and R.P Levy, **Comparison of different radiation types and irradiation geometries in stereotactic radiosurgery**, Int. J. Radiat. Oncol. Biol. Phys. **18**: 211-220, 1990.
22. P.V. Houdek, J.V. Fayos, J.M. Van Buren and M.S. Ginsberg, **Stereotaxic radiotherapy technique for small intracranial lesions**, Med. Phys. **12**:469-472, 1985.
23. F. Colombo, A. Benedetti, F. Pozza, R.C. Avanzo, C. Marchetti, C. Chierego and A. Zanardo, **External stereotactic irradiation by linear accelerator**, Neurosurg. **16**:154-160, 1985.

24. G.H. Hartmann, W. Schegel, V. Sturm, B. Kober, O. Pastyr and W.J. Lorenz, **Cerebral radiation surgery using moving field irradiation at a linear accelerator facility**, Int. J. Radiat. Oncol. Biol. Phys. **11**: 1185-1192, 1985.

25. E.B. Podgorsak, A. Olivier, M. Pla, P.Y. Lefebvre and J. Hazel, **Dynamic stereotactic radiosurgery**, Int. J. Radiat. Oncol. Biol. Phys. **14**: 115-125, 1988.

26. G. Cheirego, C. Marchetti, R.C. Avanzo, F. Pozza and F. Colombo, **Dosimetric considerations on multiple arc stereotaxic radiotherapy**, Radiotherapy and Oncology **12**: 141-152, 1988.

27. G.H. Hartmann, W. Schlegel V. Sturm and W. J. Lorenz, **A fast algorithm to calculate three dimensional dose distributions for radiosurgery**, in "Proceedings of the eighth international conference on the use of computers in radiation therapy", IEEE Computer Society Press, Silver Spring, MD, 1984.

28. W. Lutz, K.R. Winston, and N. Maleki, **A system for stereotactic radiosurgery with a linear accelerator**, Int. J. Radiat. Oncol. Biol. Phys. **14**: 373-381, 1988.

29. K.R. Winston and W. Lutz, **Linear accelerator as a neurosurgical tool for stereotactic radiosurgery**, Neurosurg. **22**: 454-464, 1988.

30. E.B. Podgorsak, A. Olivier, M. Pla, J. Hazel, A. de Lotbinière and B. Pike, **Physical aspects of dynamic stereotactic radiosurgery**, Appl. Neurophysiol. **50**: 63-68, 1987.

CHAPTER 2

EXPERIMENTAL APPARATUS AND TECHNIQUES

2.1 Introduction

The experimental apparatus and techniques used to generate and measure the physical parameters of photon beams suitable for radiosurgery are discussed in this chapter. The source of the photon beams was a 10 MV linear accelerator (1). Beam characteristics were studied with a variety of detectors in tissue-equivalent phantoms. A 3-dimensional isodose plotter (2) with diodes (3) or ionization chambers (4) was used to take beam measurements in water, while a Farmer parallel-plate ionization chamber (5) was used in conjunction with a polystyrene phantom. Radiotherapy radiographic film (6) proved to be a useful detector and irradiations of these films in polystyrene or acrylic phantoms were subsequently analysed with two densitometry systems, one a 2-dimensional radiographic film densitometer and the other a digital imaging system developed for densitometry.

The basic features of the linear accelerator used for radiosurgery at McGill University are described first, and then the characteristics of the detectors are discussed. The techniques used for radiographic film dosimetry are explained. Finally, the phantoms used in conjunction with each of the detectors are described.

2.2 Linear accelerator

A 10 MV linear accelerator was used as radiation source in our experiments. It is installed in the Radiation Oncology department of the Montreal General Hospital and has been in clinical use for conventional radiotherapy for the past twelve years. Recently, minor adaptations have extended its use to radiosurgery, and since 1986 it has also been used in this capacity. The linac is isocentrically mounted with a source axis-of-rotation distance (SAD) of 100 cm and the isocenter 130 cm above the floor. It can be used in either electron or photon mode, producing electron beam energies of discrete values between 6 and 18 MeV, or a 10 MV photon (x ray) beam with a spectrum of photon energies ranging from 0 to a maximum of 10 MeV.

Figure 2.1 shows a schematic diagram of the linac (7). The machine operates in the S-band at 2856 MHz and uses an rf driver as the source of radiofrequency (rf) and a 5.5 MW klystron as the rf amplifier. A rectangular waveguide conducts the microwave power pulses to the accelerating structure. The electron gun, operating in the range from 5 to 25 kV depending on the final electron kinetic energy desired, acts as the source of electrons to be accelerated. The accelerating structure itself is a disk loaded, 1.4 m long standing wave accelerator, containing 21 accelerating cavities. Operating at a vacuum pressure of 10^{-6} torr, the accelerating waveguide is sealed from the outside environment with a 0.25 cm thick beryllium window.

A detailed diagram of the linac head is given in Fig. 2.2 (8). After leaving the accelerating waveguide, the electrons enter the beam transport section where they are bent through 270° by a magnetic field, in which a ±10% beam energy spread is brought to a single focal point. When operating in the photon mode, the electron beam hits a target consisting of 1 cm of copper, which transforms the kinetic energy of electrons into a 10 MV bremsstrahlung x-ray spectrum. The target is inside the evacuated beam transport system and the photons exit through the beryllium window.

A primary collimator in the proximity of the vacuum window defines the maximum attainable circular photon field size. Upon leaving the target, the photon beam is sharply peaked in the forward direction and is therefore passed through a tungsten flattening filter in order to produce a uniform radiation field over the maximum field size defined by the primary collimator. The flattening filter is mounted on a rotating carousel for easy interchange between photon and electron radiation modes.

The flattened photon beam then passes through a dual transmission ionization chamber. The charges collected on the measuring electrodes of the two chambers are amplified and measured in arbitrary units, usually referred to as monitor units (MU). These monitor units are calibrated to correspond to dose (cGy) in water at the depth of dose maximum when irradiated with a 10×10 cm^2 field at a distance of 100 cm

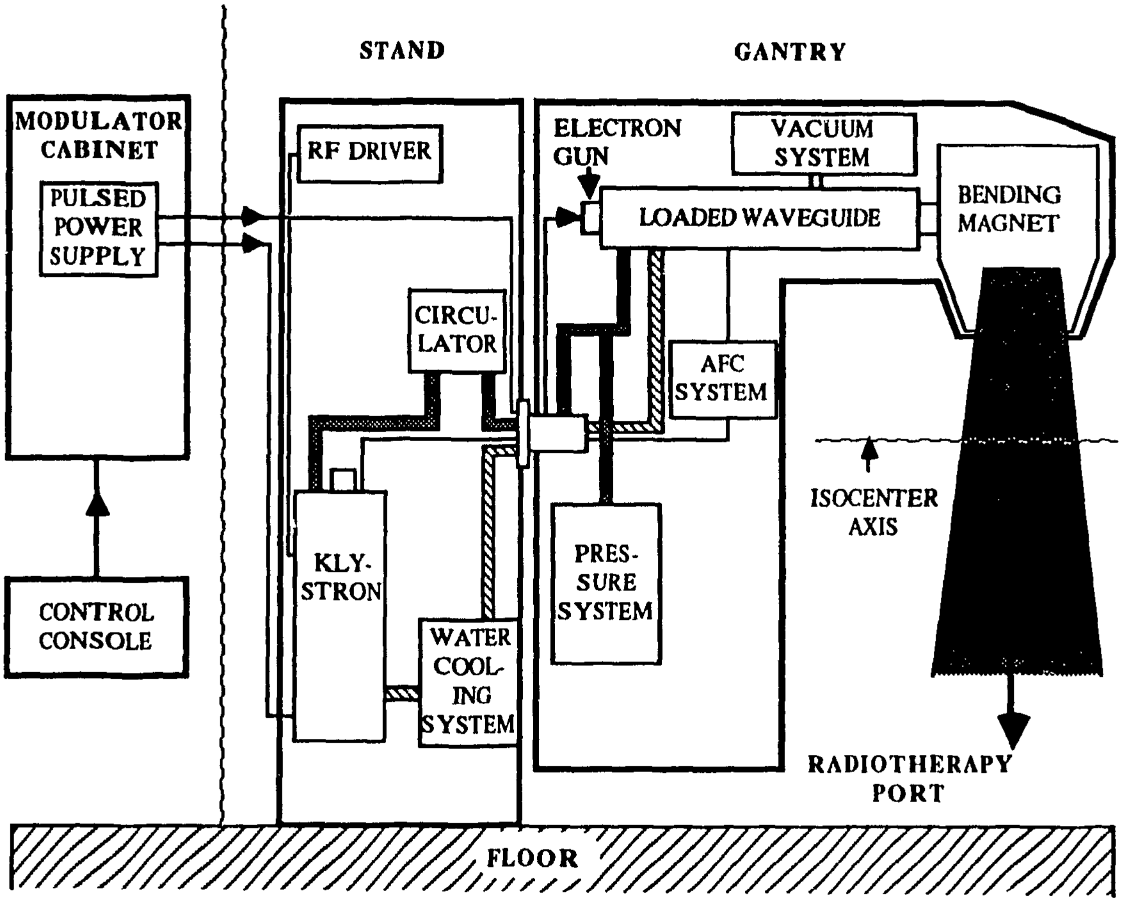

FIGURE 2.1. Schematic diagram of a typical isocentric linear accelerator showing the basic components.

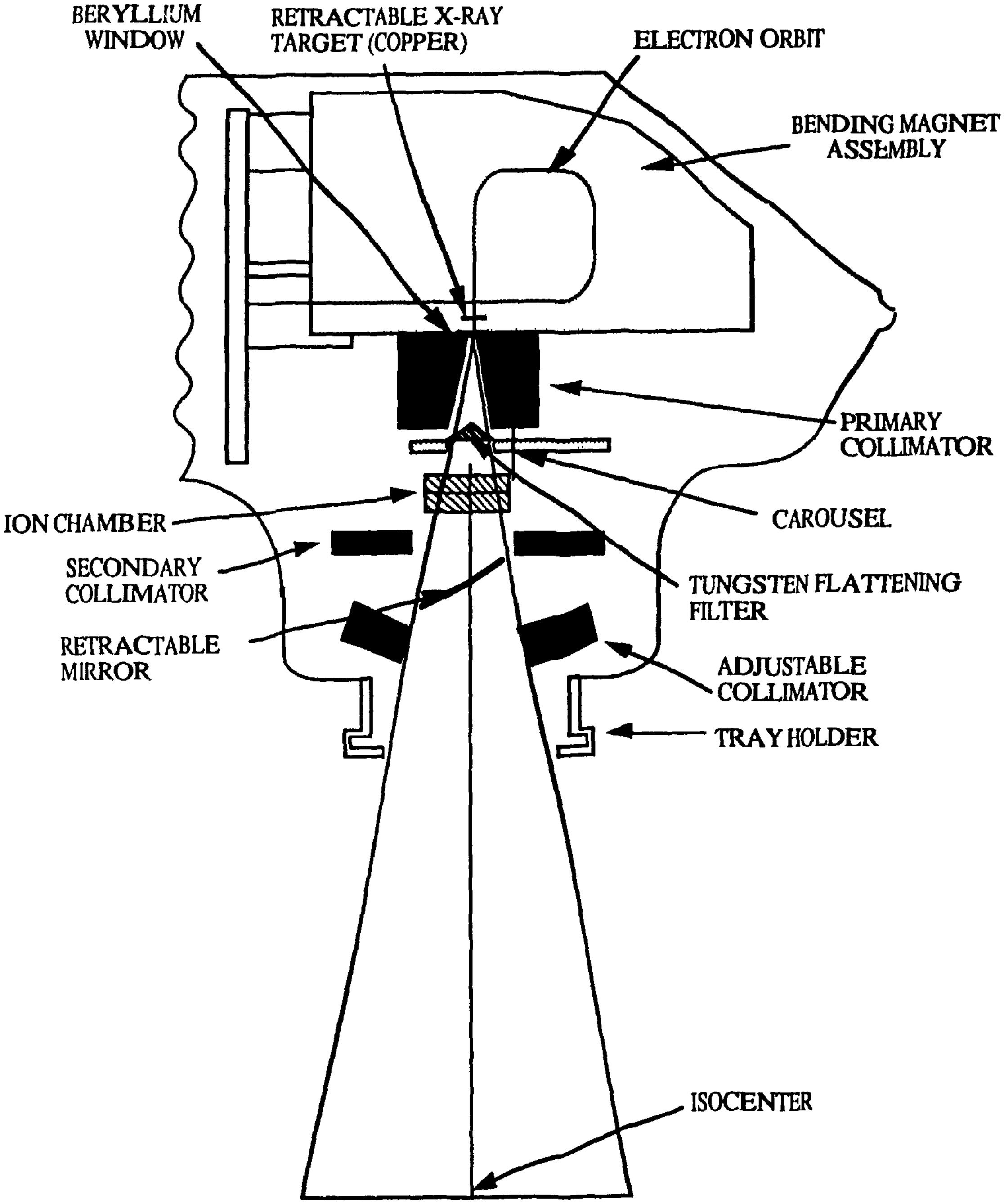

FIGURE 2.2. Detailed schematic diagram of the linac head when operating in the photon mode.

from the x-ray target. The radiation beam is switched off when a preset number of monitor units is attained. The two ionization chambers are independent to provide a redundancy check for improved safety.

As a safety precaution, a fixed secondary tungsten collimator limits the maximum square field size to 35x35 cm^2. The desired square or rectangular photon treatment field size is then defined by adjustable collimators, consisting of four tungsten blocks. To provide sharp edges of treatment fields, the movements of the tungsten blocks are confined to arcs, so that their faces present a flat edge to the beam diverging from the target. These adjustable collimators are fixed to a collimator head which can rotate about the vertical beam axis, allowing angulation of fields. A light beam, which coincides with the radiation field, is reflected into the beam path through a mirror. This mirror is removed when the radiation beam is on. Accessories to modify x-ray fields slide into slots of a tray holder which is attached to the treatment head, 65 cm below the target.

The linac has a variable dose rate with a maximum at ~500 MU per minute. The gantry can also deliver dose while rotating through a predefined arc, in either a clockwise or counter-clockwise direction. Precisely controlled dose rates from 0.25 to 5.0 MU per degree of gantry arc are then possible. The gantry has three speeds of rotation in the range from 0.1 to 0.4 rpm. The number of monitor units per degree and the degrees of gantry rotation can be set. Speed of rotation and pulse repetition frequency are then automatically fixed to achieve the desired dose rate.

The treatment couch has motor driven vertical, lateral and longitudinal motion, allowing for motorized placement of the target to the isocenter. The couch can also rotate about a vertical axis which is perpendicular to and intercepts the gantry axis of rotation and passes through the isocenter.

Three laser localization devices are used to precisely indicate the location of the isocenter, one is mounted on the ceiling and the other two are on the side walls of the treatment room. The ceiling laser designates the couch vertical axis with a dot of a diameter of 1 mm, while the two lateral lasers designate the height of the isocenter with a cross of line widths of ~1 mm.

The physical considerations of the gantry and treatment couch show that there are three degrees of freedom for treatment set-up, all of which can be related to the isocenter as a common reference point. These degrees of freedom are shown schematically in Fig. 2.3. If one considers a coordinate system fixed in space, with its origin at the isocenter, all other frames of reference are rotations and translations of this system. The gantry and couch rotations, θ and ϕ, respectively, have already been discussed in Chapter 1 where in Fig. 1.3 we defined the angular convention used in our center. The collimator itself, lying in the plane perpendicular to the beam axis, can also rotate clockwise or counter-clockwise about its axis, through an angle defined as ψ.

2.3 Radiation field analyser (RFA)

Beam parameters were measured with a varitey of detectors and measuring techniques which are described in this chapter. Ionization chambers, diodes and radiographic film were used as radiation detectors, all in conjuction with a radiation field analyser, or independently with an electrometer.

A radiation field analyser was used as a 3-dimensional isodose plotter or as a 2-dimensional radiographic film densitometer in the measurement of beam data. The analyser is controlled through a computer system based on an 80186 16-bit processor with a 20 megabyte hard disk. A software program MSDISK allows the transfer of beam data from a hard disk to a 5 1/4 inch floppy disk. Data was analysed on an IBM compatible microcomputer based on a MS DOS operating system .

When used as a three dimensional isodose plotter, the RFA plotter consists of an acrylic water tank with dimensions of 63x60x61 cm^3. A remotely controlled drive unit positions the radiation detector within a scanning volume of 50x50x50 cm^3. Diodes or ionization chambers are available as detectors, and an electrometer

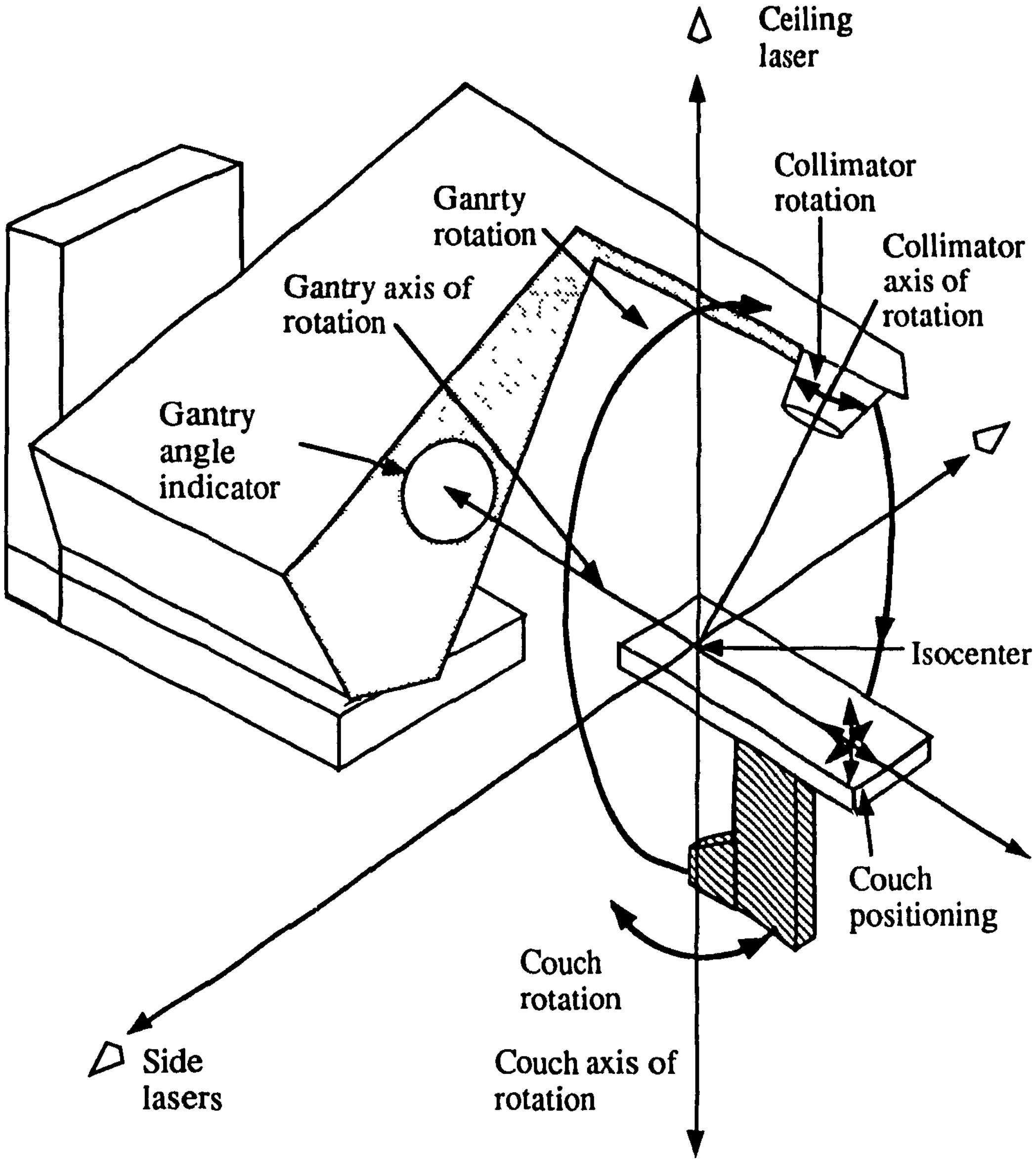

FIGURE 2.3. Degrees of freedom for treatment set-up on a linear accelerator. The gantry rotates about a horizontal axis of rotation, the couch about a vertical axis and the collimator rotates about the beam axis. All axes of rotation intersect at the isocenter which is indicated by means of two side lasers and one ceiling laser.

measures the signal received from them. For both measuring modalities two detectors are needed, one stationary in the radiation beam and the other moveable to measure ionization as a function of the chamber position in the beam. The first chamber acts as a reference and the other as the detector. The signals from the two chambers are passed through a differential amplifier and the result is digitized and stored. Using the ratio of signals minimizes the effects of fluctuations in the radiation beam intensity during the measurement. The positioning accuracy of the moveable detector is 0.5 mm, with a reproducibiliy of ±0.1 mm.

2.4 Film dosimetry

Film commonly used in diagnostic radiology imaging is also suitable as a relative dosimetry technique. Film blackening occurs during exposure to radiation and the subsequent development and fixation of a radiographic film, a process described in detail in the literature (9).

In conventional radiation dosimetry based on radiographic film, a pencil light beam of intensity B_0 is passed through the exposed and developed film at a point of interest and the amount of the transmitted light B is measured. The optical density of the film at this point is then given as the logarithm of the ratio of incident to transmitted light. This optical density vs. $\log_{10}$(dose) is the H&D curve, named after Hunter and Driffield who first described it in 1890 (10). It is sometimes also referred to as the characteristic curve for a particular film and is commonly used to asses film response to light or radiation.

When used as a dosimeter, the charateristic curve gives the relationship between optical film density and dose. This optical density is proportional to the mass of silver present in the film, which in turn is proportional to the dose. A plot of optical density vs. dose can then relate any measured optical density to a corresponding dose. Of course film blackening depends on many parameters, such as film type, processing technique, developer temperature, fixation proceedure, etc. Care must be taken to keep these parameters constant, so that any change in optical density is due only to a change in dose. Some degree of film blackening will occur even with no irradiation. This is referred to as the film fog, and must be subtracted from all measured optical densities to establish a true zero point on the characteristic curve.

The radiographic film (6) used in our experiments was of the type used for portal imaging of radiotherapeutic procedures (Kodak XV II). Beam data aquired with the radiographic film was analysed with two types of densitometers. One was the commercially available RFA used as a 2-dimensional film scanner and the other a digital imaging system developed for film densitometry.

In the RFA densitometer a transparent acrylic plate to hold the film is placed above the water tank. The optical system is driven by two independent motors, moving both the detector and light source simultaneously within a 50x50 cm^3 scanning area. The light source is a tungsten filament incandescent lamp with a radiated spectrum equal to that of a black body radiator at a temperature of 2850 K. The detector consists of a silicon photodiode with an active area of 1.6 mm^2, sensitive to light with wavelength ranging from 400 to 1150 nm and a spectral response peak at 925 nm when the acrylic window is in place. Optical lenses are used to focus the light spot. The spatial resolving capability of the densitometer is about 0.8 mm.

Typical calibration curves obtained with our radiographic film (6) on this system are shown in Fig. 2.4. The films were irradiated with 10 MV x rays to various doses up to 200 cGy in a polystyrene phantom. The measured optical density first rises linearly as a function of dose at low doses between 0 and 50 cGy. At larger doses, however, the density saturates at a dose of about 300 cGy. The measured optical density ranges from about 0.06, the fog, to about 3 at saturation. Shown in the graph are calibration curves obtained with photon beams under various irradiation conditions. The film was calibrated for different film batches, on different dates, and at a variety of depths in the polystyrene phantom. At low doses, the curves do not

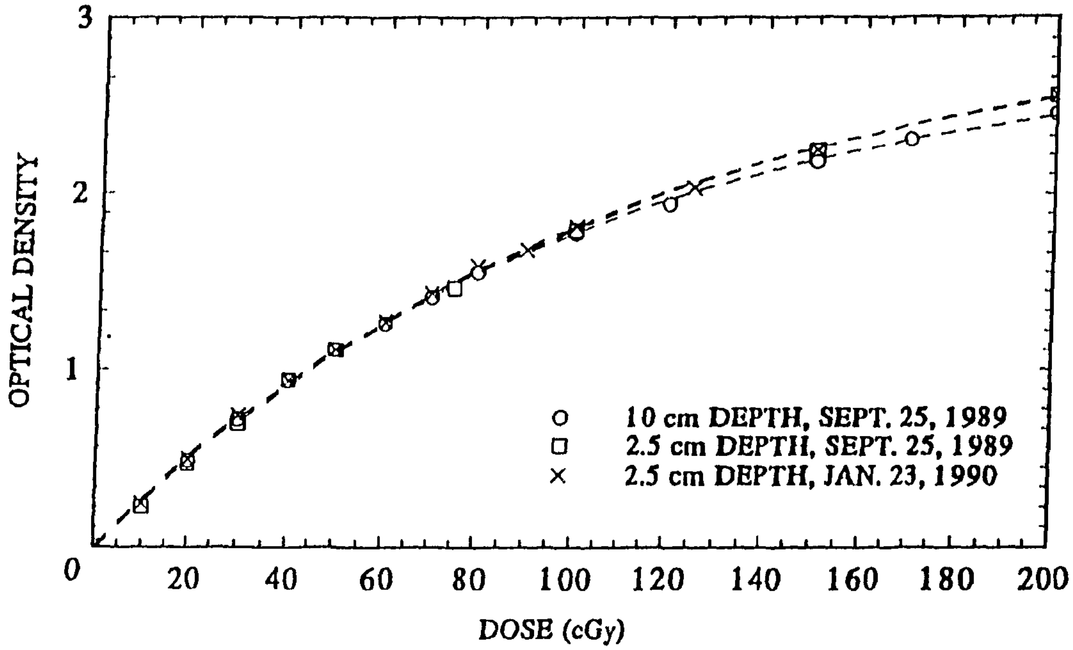

FIGURE 2.4. Characteristic curves for radiographic film (Kodak XV II) used in our experiments. Optical density of irradiated films as measured with the RFA densitometer for different film batches is plotted against dose. The films were irradiated to different doses at a variety of depths in a polystyrene phantom.

change with these parameters. Thus the same calibration curve can be used to analyse each irradiated film, provided that the dose is kept well below the saturation dose.

In the digital densitometry system, on the other hand, the film was placed on a high power uniformly illuminated light box and imaged with a solid state charge2 coupled video camera (11) through a 50 mm flat lens (12). The lens and camera were mounted on an adjustable arm, attached above the light box to enable versatile magnification. Images of 256 by 256 pixels (or 512 by 512 pixels if desired) were acquired with a frame grabber (13) and subsequently analysed with a Sun 386i/250 computer. The spatial resolution of this system depends on the magnification used, but is typically 0.2 mm per pixel. The intensity of light reaching the camera is measured and related to a grey scale ranging from 1 to 256. This intensity changes with degree of film blackening, and can thus be related to the dose in a manner similar to the RFA densitometry system described above. The film is calibrated by relating a known dose to a pixel intensity.

Figure 2.5 shows typical calibration curves obtained with the digital system. The curves are non-linear with dose and very specific to a particular camera setting, such as the camera magnification and the lens aperture opening. This means that the calibration curves are strongly dependent on the amount of light reaching the camera. Thus, a calibration curve should be measured for each camera setting used in the analysis of films and the resulting curve can then be used only under identical circumstances. However, given a particular setting, the calibration curve can be reproduced relatively easily, fulfilling the requirements for accurate dosimetry. At high doses, the film becomes too black to allow the camera to distinguish changes in intensity. All four curves of Fig. 2.5 converge at high doses to a minimum intensity whose magnitude varies depends on the camera and lens combination. When using this system as a dosimeter, care must be taken to ensure that all doses result in an intensity greater than that to which the calibration curves converge. This is easily done by keeping doses below 50 cGy, an acceptable solution in our measurements as we were interested only in relative dosimetry.

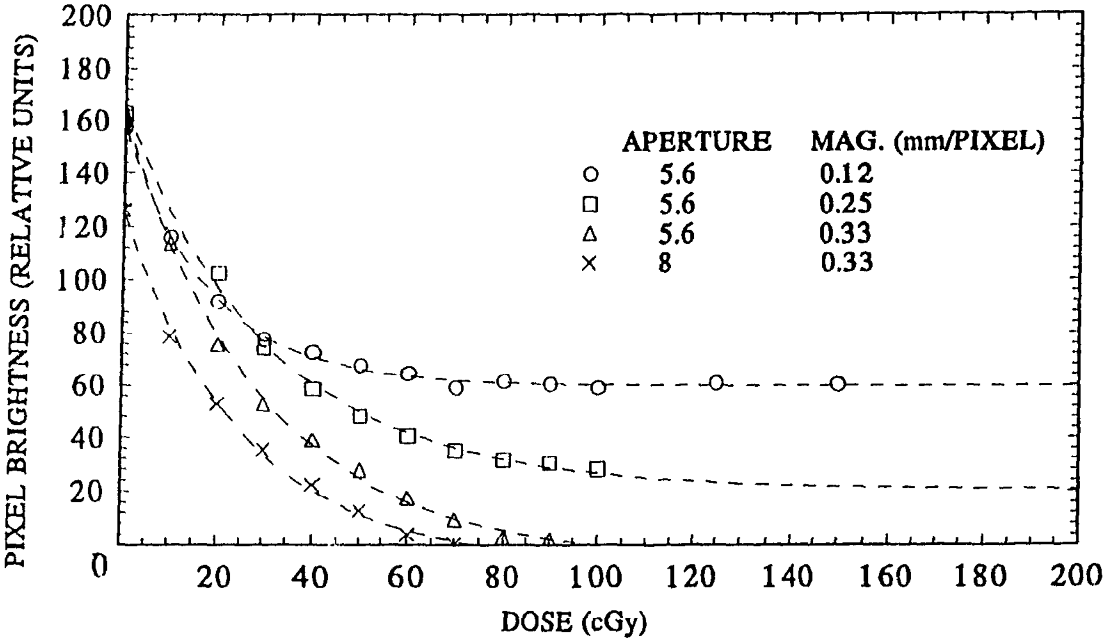

FIGURE 2.5. Characteristic curves for radiographic film used in our experiments and measured with the digital video imaging system. Light intensity passing through the irradiated film and reaching the camera is related to a grey scale ranging from 0 to 250. The same film densities will result in different intensity readings for different lens aperture openings and camera magnifications. The films were irradiated to known doses in a polystyrene phantom at a depth of 2.5 cm.

2.5 Ionization chambers and diodes

Detector size and their corresponding spatial resolution are very important factors, given the small field dimensions of the beams used in radiosurgery. The detector's cross-section of the sensitive volume must be considerably smaller than the beam diameter. Any charge or current measured due to the creation of ions upon irradiation must be related to a known mass in order to determine the dose. This criterion puts a substantial restriction on suitability of detectors, as the fields to be measured range from 0.5 cm to 3.5 cm in diameter. Therefore, only small volume ionization chambers and diodes were used in our measurements of radiosurgical beam data.

The diode detectors were p-type silicon semiconductors, requiring about 3 eV to produce an electron-hole pair, with the resulting current proportional to the dose received. They operate in the photovoltaic mode, so that no potential difference across the device is required. The outer dimensions of the cylindrical detector are 8.0 mm for the diameter and 25 mm for the height. The outer material is an epoxy resin, coated with a thin layer of water resistant paint. The silicon crystal itself has a sensitive volume of 0.25 mm^3, a diameter of 2.5 mm and a thickness of 60 μm. The measuring volume lies 0.55 mm below the detector's surface.

The diode proved to be the most suitable detector for beam measurements in air because of its small volume of interest. The high energy of the linac beam requires that a build-up cap covers the detector when beam parameters are measured in air in order to ensure electronic equilibrium (14). If made of a tissue equivalent material, the cap would require a thickness of 25 mm for the 10 MV beam making the detector plus cap diameter larger than the diameter of most radiosurgical beams. To overcome this, a brass build up cap was constructed for the semiconductor detector. Because of the higher attenuation coefficient of brass, a thickness of only 3 mm of brass was needed to achieve electronic equilibrium. Given the detector diameter of 8 mm, the diameter of detector with build-up cap was 14 mm. Thus, this set-up could be used for all but the smallest beams. Since only doses relative to a standard 10x10 cm^2 field were measured in air, the lack of tissue equivalence of brass was not taken into account.

In an ionization chamber, the measured signal is related to the ions produced and collected during irradiation. Both thimble and parallel-plate ionization chambers were used in our experiments. Practical thimble ionization chambers contain a single, charged electrode in the chamber's central air cavity. The wall of the chamber is made of an air-equivalent material, with an inner coating of conducting material. Exposure can be measured and related to the dose through calibration and correction factors. A parallel plate chamber, on the other hand, contains two charged plates separated by some distance thus creating an electric field. Guard rings ensure a uniform field in the volume-of-interest. The principles of operation are of course the same for both the thimble and parallel plate chambers. A known mass of air is irradiated, the ions produced by radiation are collected, and the charge measured is related first to exposure through a calibration factor, and then to the dose in the irradiated medium.

The ionization chambers used with the RFA isodose plotter are thimble ionization chambers with outer dimensions of 7.0 mm for the diameter and 25 mm for the height (3). The air cavity itself has a volume of 120 mm^3, a diameter of 4.0 mm and a length of 10 mm and contains a central electrode 9 mm in length. The thimble is made of acrylic with an inner graphite wall. A typical polarizing potential voltage of 250 V is applied to the chamber.

A Farmer type parallel plate ionization chamber (5) was used for percentage depth dose measurements to take advantage of its high depth resolution and its capability for measurement of surface doses. The chamber has a volume of 0.03 cm^3, an electrode separation of 1.0 mm, a sensitive diameter of 3 mm and a diameter including the guard ring of 5.2 mm. Its polyethylene wall has a thickness of 0.03 mm. It is used with a polarizing voltage of 300 V, has a sensitivity of 7×10^{-12} C/R and a leakage current of $\pm1\times10^{-14}$ A. The current was read with an electrometer (15).

2.6 Phantoms

Phantoms simulating soft tissue were used in conjuction with the dosimeters described above. The RFA unit, with its semiconductors and thimble ionization chambers, allows scan measurements in water. Sheets of polystyrene, ranging in thickness from 0.6 mm to 3.2 mm, were used with both the parallel plate chamber and film.

When measuring the dose distribution resulting from radiosurgical treatment simulations, or some other combination of radiation beams, a spherical phantom was used in conjunction with radiographic film as a detector. The phantom consisted of 26 sheets of Lucite, each 0.635 cm thick with variable radius, so that when the circular sheets were stacked together, they resulted in a sphere with a radius of 8.25 cm approximating the dimensions of a human head. Sheets of film could be placed between any two layers of the phantom, and the phantom could have arbitrary orientation, allowing the measurement of dose in any plane at any orientation for a given radiosurgical technique.

2.7 Summary

In this chapter we discussed the basic experimental apparatus and techniques used to generate and measure dose distributions obtained for photon beams used in radiosurgery. The detectors are discussed with respect to their ability to adequately measure properties of the narrow radiosurgical radiation beams. Given that even small detectors have diameters of the same order of magnitude as the photon beams to be measured, the question of spatial resolution must be addressed. Radiographic film proved to be a very versatile detector, so the particular film densitometry techniques used are explained in some detail in this chapter. The characteristic curves describing the density vs. dose relationship of the film as obtained with one of two densitometry systems can be used to convert an optical density measurement or pixel brightness to dose. The digital film densitometry system exhibits excellent spatial resolution, making the detector very suitable for small scale measurements, although it has a reduced latitude for high exposures.

2.8 References

1. Linear accelerator, Clinac 18, Varian Associates, Palo Alto, California.
2. Radiation field analyzer, RFA-7, Therados, Uppsala, Sweden.
3. Air ionization chamber, type RK, RFA-7, Therados, Uppsala, Sweden.
4. p-type semiconductor detector, RFA-7, Therados, Uppsala, Sweden.
5. Farmer type ionization chamber, model 2505/3, Nuclear Enterprises Ltd., Beenham, Reading, England.
6. XV-II ready pack film, Eastman Kodak, Rochester, New York.
7. C.J. Karzmark and R.J. Morton, **A primer on theory and operation of linear accelerators in radiation therapy**, U.S. Department of Health and Human Services, Food and Drug Administration, Bureau of Radiological Health, Rockville, Maryland, 1981.
8. Customer course documentation on Clinac-18 maintenance, Varian Associates, Palo Alto, California.
9. T. S. Curry, J. E. Dowdey and R. C. Murry, **Christensen's introduction to the physics of diagnostic radiology**, 3rd edition, Chap. 10, Lea & Febiger, Philadelphia, 1984.
10. F.H. Attix, **Introduction to radiological physics and radiation dosimetry**, John Wiley & Sons, Toronto, 1986, p.414.
11. Video Camera, VDC 3874, Sanyo Electric Inc., Compton, California.
12. 50 mm flat lens, Componar-C, Schneider, Kreuznach, Germany.
13. Frame grabber, MVT-ATi, Matrox, Montréal.
14. H. Johns and J. R. Cunningham, **The physics of radiology**, 4th edition, Charles C. Thomas, Springfield, Illinois, 1983, p. 239.
15. Electrometer, model 616, Keithley Instruments Inc., Cleveland, Ohio.

CHAPTER 3

PHYSICAL PARAMETERS OF RADIOSURGERY BEAMS

3.1 Introduction

In this chapter physical parameters which pertain directly to radiosurgery are discussed. We first describe the typical modifications and additions to standard isocentric linacs to make them useful for clinical radiosurgery. Then we discuss the typical set-up which is used in our center for delivering radiosurgery and which was also used in our radiosurgical experiments. The adequacy of the set-up, in terms of spatial accuracy of dose delivery, is also addressed in this chapter. Simple tests show that linac-based radiosurgery can provide a high degree of spatial accuracy. The results of the measurements of radiosurgical beam parameters are then analysed. A particular effect observed during the measurement of depth doses in the build-up region, a shift in depth of dose maximum with field diameter, is examined in some detail, and the cause of the effect is explained.

3.2 Modifications to the linear accelerator for use in radiosurgery

Radiosurgery sets requirements on linear accelerators that are quite different from those encountered in conventional radiotherapy. The small radiation field sizes used, the stringent requirement for patient immobilization and the mobility of gantry and couch movement involved must be considered, and several adaptations to standard linacs must be made, before the machine can be used for radiosurgery. In our case all necessary alterations and additions to the linac were constructed and implemented by the Department of Medical Physics at the Montreal General Hospital.

Additional collimation is necessary for use in radiosurgery to achieve the small, well defined circular fields. A typical collimator used in our center is shown schematically in Fig. 3.1. It consists of two lead cylinders, each 5 cm long and 5 cm in diameter, lying on top of each other and straddling a 0.65 cm thick acrylic plate. This enables placement of the collimator assembly into the tray holder of the linac, in

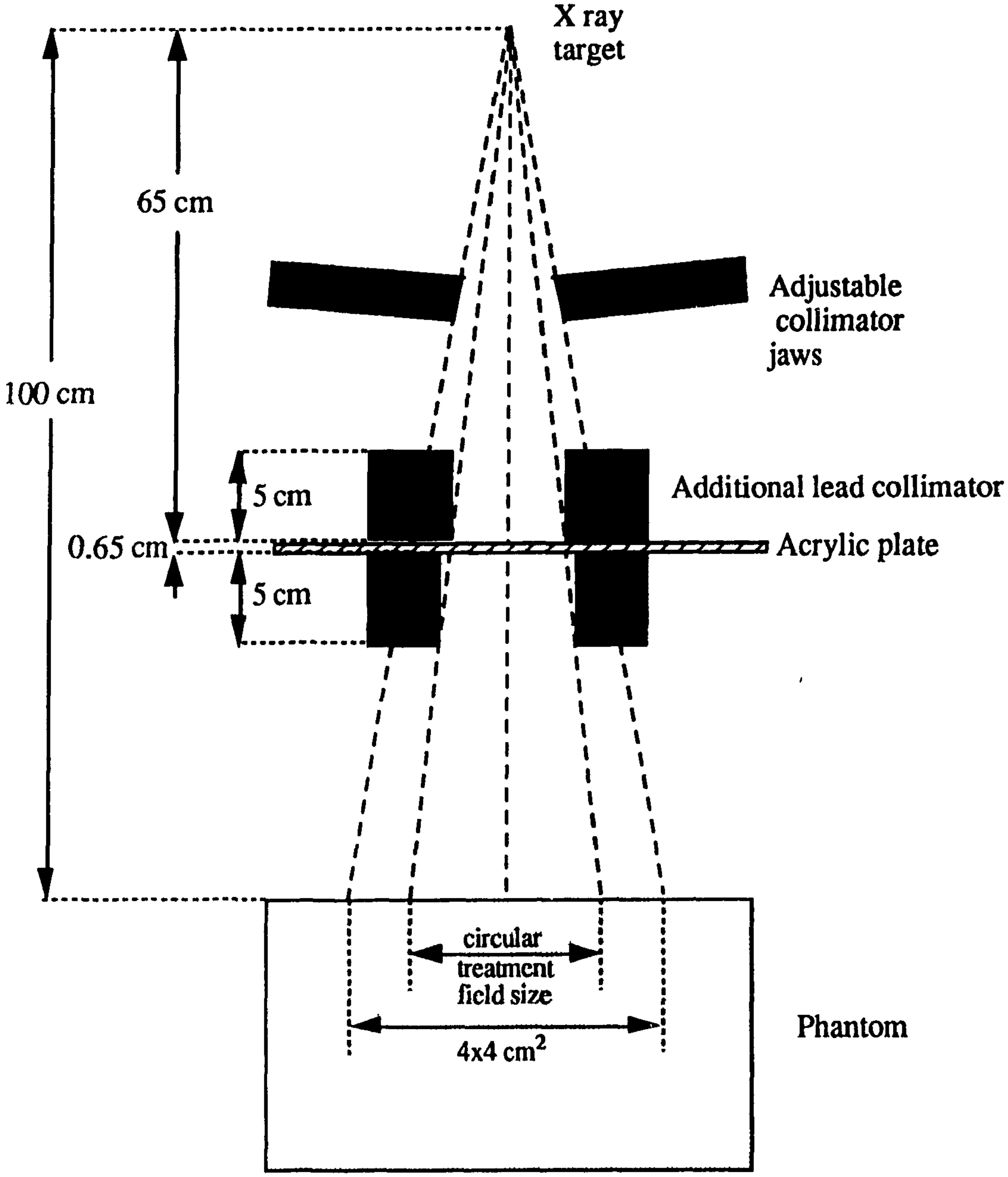

FIGURE 3.1. Geometry of experimental set-up used in measurement of radiosurgical beam parameters. Shown is an example of an additional radiosurgical field collimator and its positioning with respect to the machine collimator. Also shown is a tissue equivalent phantom at 100 cm from the target.

the path of the photon field. The linac adjustable collimator jaws are fixed to give a field size of 4x4 cm^2 at the isocenter. Small cylindrical apertures were drilled into each half of the lead collimator, such that the geometrical beam divergence determines the diameter of the the hole in the top and bottom halves of the collimator, as shown in Fig. 3.1. The nominal field diameters at the isocenter of the collimators in our set used for radiosurgery range from 0.5 cm to 3.5 cm in steps of 2.5 mm.

Additional remotely controlled couch motorization has been installed by the Department of Medical Physics to enable simultaneous couch and gantry rotation during the radiosurgical treatment. The couch rotation is monitored by means of an angular position readout on the machine console. The couch rotation is run by the gantry rotation control circuitry and its speed is fixed to be one half the gantry's speed. This addition is specific to the radiosurgery technique which was developed at McGill University and is referred to as the *dynamic rotation.*

A bracket is attached to the head of the treatment couch to fasten the stereotactic frame to the couch and to thereby immobilize the patient during treatment. During the treatment, i.e., while the couch is rotating, a brake which immobilizes lateral and longitudinal couch motions is enabled to ensure that shifting of the target volume from the isocenter cannot occur. The height of the stretcher top as well as the couch angle are continuously monitored during the radiosurgical procedure. A change of couch height by more than 0.5 mm or an excessive discrepancy between the couch angle ϕ and the gantry angle θ (i.e., if $2\phi - \theta <> 3°$) shuts the radiation off automatically.

3.3 Spatial accuracy

As mentioned before, radiosurgery is usually given in one high dose irradiation (~2000 cGy) with a very small field size (diameter ~1 cm). This makes the requirements on accuracy of dose delivery, both spatial and numerical, far more stringent in radiosurgery than in conventional radiotherapy where a series of lower dose treatments is delivered (typically 25 fractions of 200 cGy each). The spatial accuracy falls into two categories, the accuracy of the determination of the target volume and subsequently, the accuracy of the dose delivery to this target volume.

Given the recent advances in modern imaging modalities, such as CT, MRI, and DSA, the ability to localize a treatment target has been greatly facilitated. All of these modalities can be used in conjunction with stereotactic frames, first to determine the coordinates of a volume-of-interest and then to bring this volume-of-interest to the isocenter so that the radiation dose is delivered to this target. Presently, with modern radiosurgical techniques, the accuracy of target localization lies within ±1 mm (1) and radiation dose can be delivered to the target with roughly the same precision.

The spatial accuracy of dose delivery in radiosurgery depends not only upon the chosen treatment technique, it also depends on the equipment itself and the care with which it is used. The general properties of radiosurgical techniques were described in some detail in Chapter 1. The Gamma unit has no moving parts during the treatment, resulting in the highest potential for spatial accuracy. In 1975, publications indicate that all 201 beams of the unit focus to a sphere of radius of 0.3 mm (2), and more recently, the maximum misalignment of each beam at the focal point was given as ±0.1 mm (3). Thus the achievable alignment of beams from the Gamma unit falls within fractions of a millimeter, giving these machines an extremely high degree of spatial accuracy, exceeding in principle even the accuracy of target localization.

Because the Gamma unit provided the first commercial means of performing radiosurgery, and because of its excellent potential for spatial accuracy, it has become in many ways a standard to which other treatment modalities are compared. All linac-based radiosurgical techniques require moving parts to achieve a sharp dose fall-off outside the target volume. The dose is delivered by relying on rotation of the gantry and the couch even though the rotations are not necessarily simultaneous. The rotational movements have raised questions concerning the stability of linac-based techniques. However, if the linac is in a good mechanical condition, it can be shown through simple tests, that linac-based radiosurgical techniques can provide the required spatial accuracy of dose delivery (4).

For the dynamic rotation technique, developed and used clinically at McGill University, both the couch and gantry rotate simultaneously about a well defined point referred to as the isocenter. Results of a series of tests to determine the spatial accuracy of dose delivery with this technique are shown in Fig. 3.2. The purpose of this test was to verify the collimator alignment with respect to the gantry rotation and the couch rotation axes. The variable machine collimators were set at the usual field size of 4x4 cm^2, and the additional radiosurgery field defining collimators (nominal diameters of 5 mm to 30 mm in steps of 5 mm) were placed in the tray holder and centered about the isocenter with the help of the three alignment lasers. A radiographic film (Kodak XV II) was centered between sheets of a 3 cm thick polystyrene phantom at the isocenter. For each of the collimators the film was irradiated in four different ways with the film always positioned at the isocenter perpendicularly to the beam central axis.

The single field data of Fig. 3.2 column (a) shows the size and shape of the beam at the isocenter for the various collimators, providing a comparison with subsequent configurations. The data were obtained with a single irradiation of the film with a vertical beam. Next films were irradiated with two parallel-opposed beams, the first two beams were aligned along the vertical gantry position, and the next two were aligned along the horizontal position, with the results shown in Figures 3.2 (b) and (c), respectively. In either case, and with all field sizes, the two parallel beams appear almost perfectly superimposed, indicating an excellent mechanical alignment of the gantry rotation. A fourth set of films, Fig. 3.2 (d), indicates the variation of a stationary vertical field with couch rotation. The film was placed on the couch, which was rotated through 180° during the vertical irradiation. The films of Fig. 3.2 (d) show that the couch does not shift with respect to the isocenter during

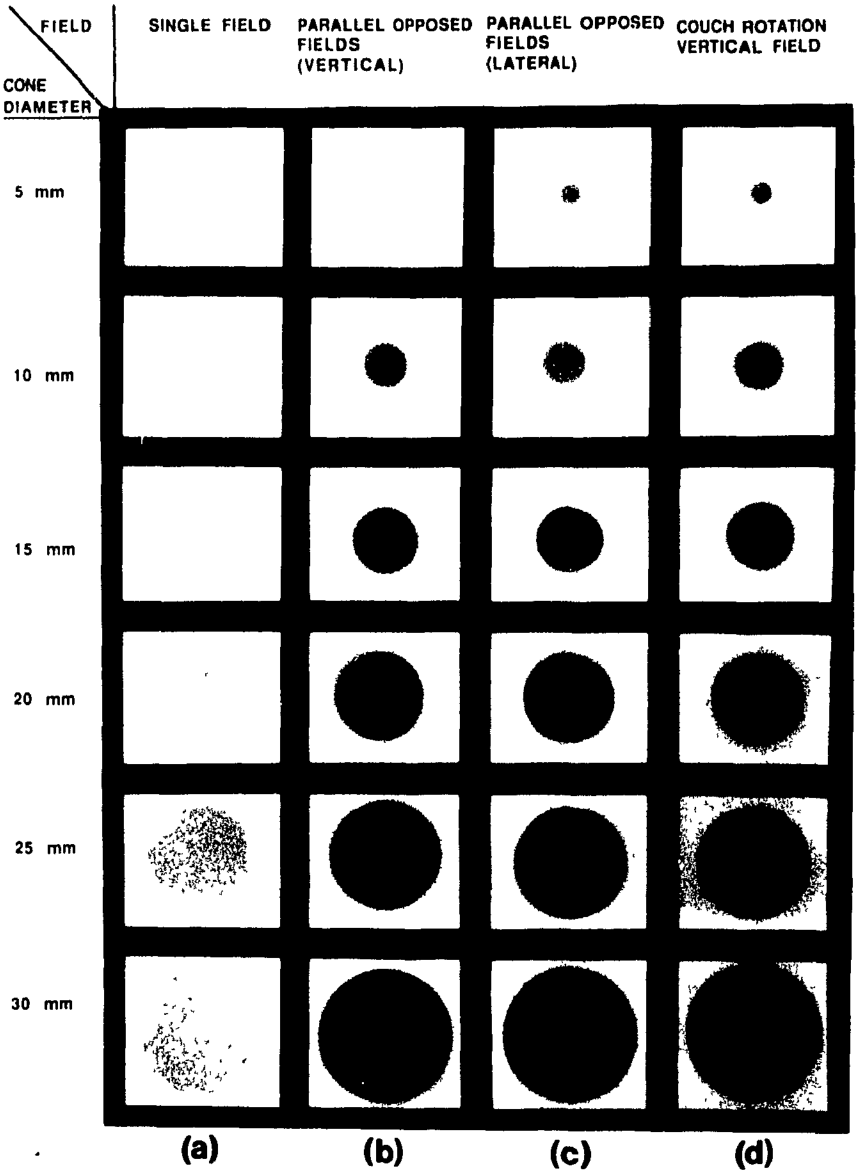

FIGURE 3.2. Tests to determine spatial accuracy of dose delivery in dynamic rotation radiosurgery. Part (a) is for single field data of vertical beams at isocenter. Superposition at isocenter of parallel-opposed fields for part (b) two vertical beams and part (c) two lateral beams. Part (d) is for the rotation of couch through 180° during irradiation at isocenter by a vertical beam. The tests are performed using film as a detector for a selection of treatment collimators used clinically at our center.

the full rotation of 180°, since the collimator image of the rotating film is essentially identical to that of the stationary beam of Fig. 3.2 (a).

Figure 3.2 provides evidence that our linac is in an excellent mechanical condition for accurate clinical radiosurgery. Results of further experiments with radiographic film and a 1 cm diameter collimator to verify the mechanical accuracy of our linac are shown in Fig. 3.3. The first film, in Fig. 3.3 (a), shows the alignment of radiation and light fields. The film was placed at the isocenter in the polystyrene phantom perpendicularly to the vertical beam. The radiosurgical collimator was centered to the ceiling laser by centering the light field to the isocenter position as indicated by the ceiling laser. The dark spot in the center indicates a pin-prick at the isocenter as determined by the ceiling laser. The film was then irradiated with two vertical parallel-opposed beams. The film shows the dark spot centered well with respect to the two superimposed radiation fields. The parallel-opposed fields are slightly shifted, indicating a less than optimal collimator placement. Yet the shift is within ±0.5 mm. We conclude that the light and radiation fields coincide well and that centering of the radiosurgical collimators with the help of the light field is acceptable.

The other three films in Fig. 3.3 depict the superposition of four fields, two parallel-opposed vertically and two parallel-opposed laterally. The films were either perpendicular, parallel, or oblique at a 45° angle to the vertical direction and the results are shown in Fig 3.3 columns (b), (c), and (d), respectively. The orientation of the film and the incident beams are shown schematically in the top portion of the figure. The four fields superimpose well, certainly within ±0.5 mm. The beams passing in a parallel orientation through the films show a slightly poorer superposition. This can be attributed to the divergence of the beams with depth. The shape of the irradiated spot in Fig. 3.3 (d) is an ellipse as expected, because of the 45° film orientation with respect to the vertical.

It is obvious from Figures 3.2 and 3.3 that the spatial accuracy of linac-based techniques can be made to fall well within the present accuracy of target localization, i.e., well within ±1 mm. This accuracy depends not only on the mechanical

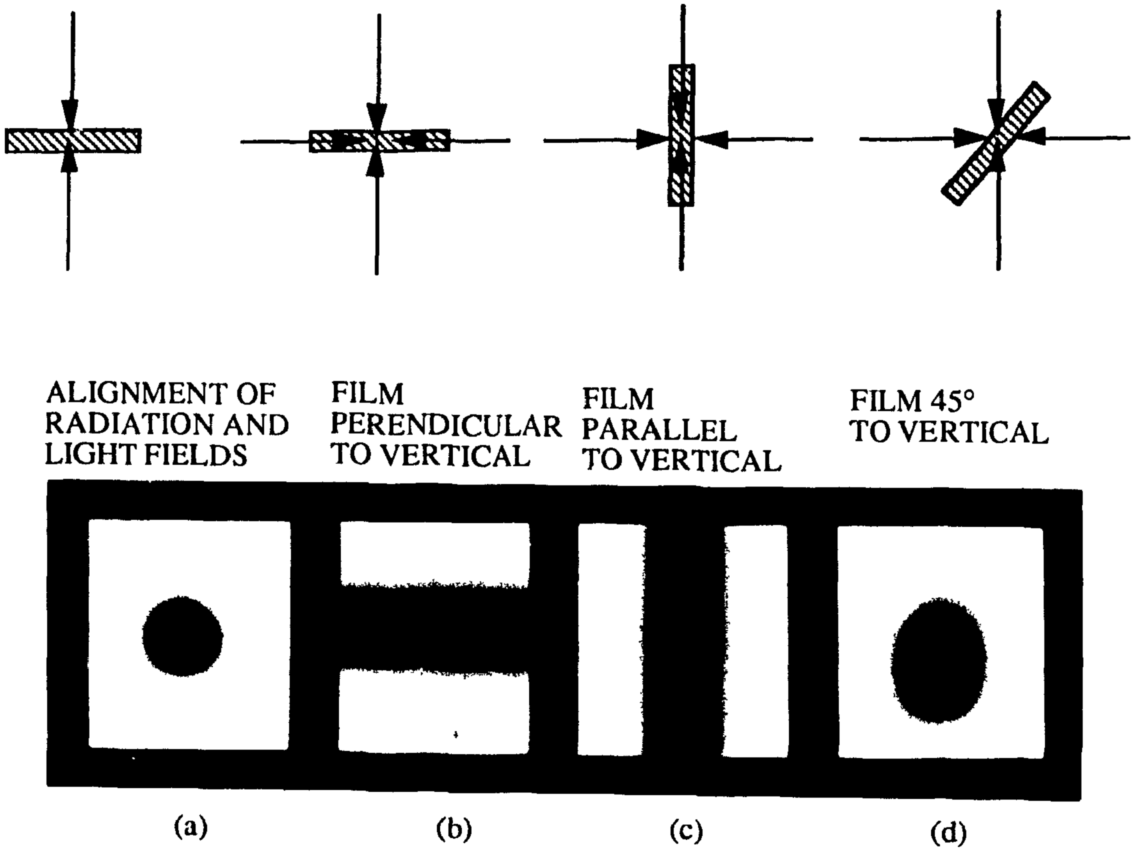

FIGURE 3.3. Alignment of several radiation fields defined by the 1 cm treatment collimator at isocenter. Part (a) alignment of two parallel-opposed vertical radiation fieids and light field as indicated by a pin prick through the laser point marking the center of the light field. Parts (b), (c), and (d) show the alignment of four radiation fields. The film is placed at isocenter perpendicular to the vertical beam, parallel to the vertical beam and at a 45° angle to the vertical beam for films in parts (a), (b) and (c), respectively. The orientation of the film and the incident beams are shown schematically in the top portion of the figure.

iscentricity of the linear accelerator, but also on the proper placement of the treatment collimator in the tray holder. Great care must be taken that the collimator is correctly centered about the isocenter, and a quick film check of vertical parallel-opposed beams to verify that this is the case should be made before commencing each treatment.

The potential problems with spatial accuracy resulting from an improper placement of radiosurgical collimators are demonstrated in Fig. 3.4. Again, film was placed at the isocenter in a 3 cm thick polystyrene phantom perpendicularly to a vertical radiation beam obtained with a 1 cm diameter collimator. The collimator was first centered with the procedure discussed above and then shifted intentionally in either the longitudinal (along the gantry axis) or the lateral (perpendicularly to the gantry axis) direction. Three collimator shifts were studied: 0.5 mm, 1 mm and 2 mm, and the results are shown in Fig. 3.4. As seen in Fig. 3.4 (a), a longitudinal shift of the collimator does not affect the superposition of the two vertical beams. This is expected since the longitudinal axis remains coincident with the axis of gantry rotation, which is referred to as the isocenter axis. In the lateral direction, on the other hand, even a slight misalignment of the collimator about the isocenter results in a very poor superposition of the parallel-opposed fields, far exceeding the limits on the accuracy imposed by the target localization, as seen in Fig. 3.4 (b). However, the images in Fig. 3.4 clearly indicate that a misplaced radiosurgical collimator can be readily detected by means of a simple film verification prior to treatment.

Thus, a conclusion can be made that if care is taken during the treatment set-up, a linac can be adapted to meet the stringent requirements on spatial accuracy in radiosurgery, falling well within ±1 mm, the present limit on target localization with imaging techniques. In the future, imaging modalities and stereotactic frames may improve even further, indicating a need to re-evaluate the current linac performace, but for the present, the higher degree of accuracy of the Gamma unit seems unnecessary, and should not be an important factor when comparing radiosurgical techniques.

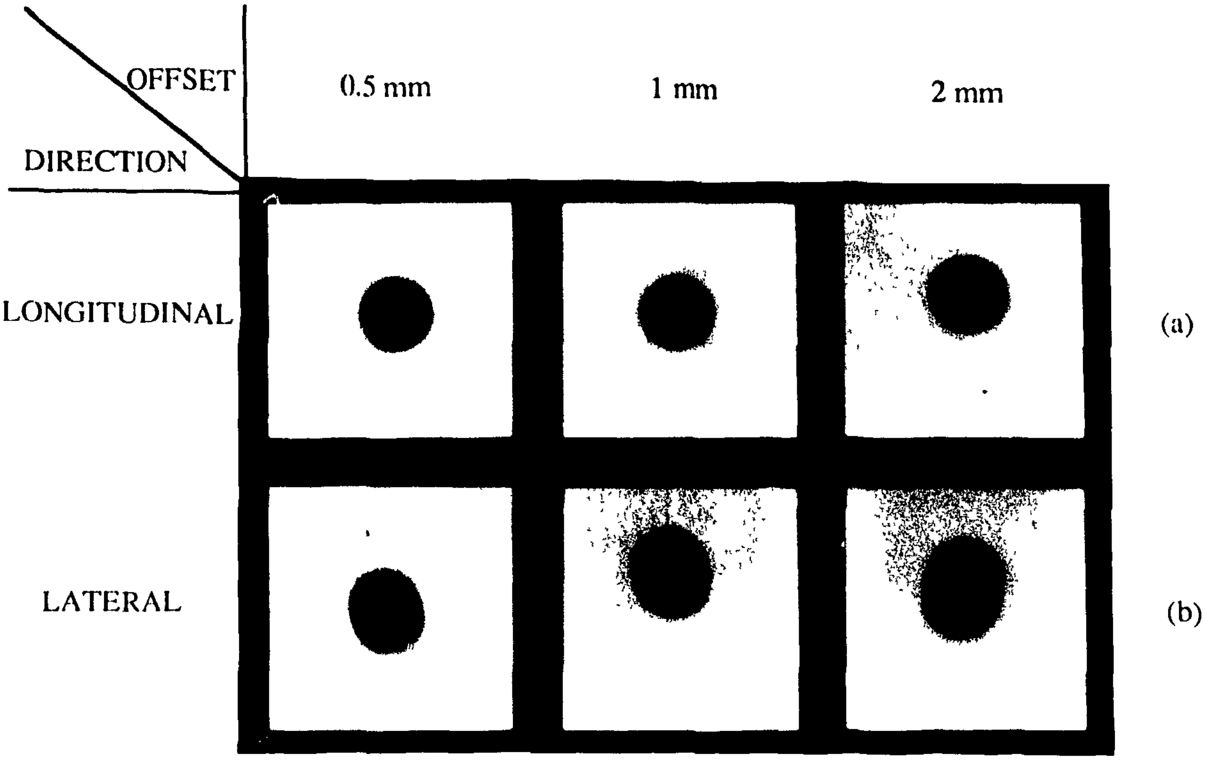

FIGURE 3.4. Alignment of parallel-opposed vertical fields obtained with the 1 cm diameter treatment collimator shifted with respect to the laser indicated isocenter. Part (a): collimator is offset from central position by 0.5, 1 and 2 mm in the longitudinal direction, and part (b): collimator is offset by same amounts in the lateral direction.

3.4 Profile measurements for stationary beams

A beam profile gives the distribution of dose along the cross-section of a radiation beam at a particular depth in a phantom. The doses are normalized to the dose on the central beam axis and are usually given as a percentage of this dose. These percentages are referred to as off-axis ratios (OAR) and are plotted as a function of distance from the central axis. Measurements were made to determine the beam width as a function of depth and the size of the beam penumbra. The data are used in the calculation of dose distributions for radiosurgery.

Since the radiosurgical beams are of very small cross-sections, the techniques used in the measurement of beam profiles for standard radiotherapy beams are not necessarily adequate for the profile measurements of radiosurgical beams. To determine the suitability and dependence of the measurement on detector size and orientation we measured profiles of our radiosurgical beams with several different detectors. The ability of these detectors to accurately resolve the profile of a narrow beam was investigated. The profile of each beam was measured in a tissue equivalent phantom with the various detectors at a depth of 2.5 cm, which is the nominal depth required for the dose of a 10 MV photon beam to reach its maximum, equilibrium value. In order to study the beam divergence, profiles were also measured at various other depths in phantom. All measurements were done with a vertical stationary beam and a source-surface distance (SSD) of 100 cm. The dose measurement techniques were discussed in some detail in Chapter 2. The exposed film was analyzed with the RFA densitometer as well as the digital video analysis system. Profile measurements were also made with the semiconductor and the thimble ionization chamber on the RFA 3-dimensional isodose plotter. The semiconductor was placed in an upright position, parallel to the beam central axis. Its small sensitive volume and small diameter made this the most suitable orientation. The ion chamber was positioned in three different orientations to investigate the effects of its asymmetrical sensitive volume. When on its side, the long axis of 10 mm was placed perpendicularly to the beam. Scans could then be performed along the longitudinal direction of the detector or along the direction of the 4 mm diameter of the cylinder. In the upright orientation, the sensitive volume has an upper surface diameter of 4 mm.

Examples of results of these measurements at the depth of 2.5 cm are shown in Fig. 3.5 for two collimator sizes: 1 cm diameter in Fig. 3.5 (a) and 3 cm diameter in Fig. 3.5 (b). The graphs indicate that the ability of the detector to resolve the sharp edge of the profile is a direct reflection on the size and orientation of the detector's sensitive volume. The sharpest profile was measured with the digital video analysis of the films. At the magnification chosen to image the films, the spatial resolution of the system was less than 0.15 mm per pixel. The slight tail at the end of the profile, a few millimeters in width, indicates the beam penumbra.

The measurement of films with the RFA densitometer and the measurements taken with the semiconductor exhibit a similar behaviour. The fall-off of the profiles is quite steep from doses of 90%to 20%, with a shallower fall-off at doses below 20%. This tail, which is larger than would be expected from the beam penumbra, can be explained by the finite size of the detectors. As the detectors scan across the beam (or the aperture across the image of the beam in the case of the exposed film), the detectors are still partially irradiated, thereby detecting dose, even though the reference point of the chamber has passed out of the beam diameter. As the detector becomes larger or the field diameter smaller, this effect becomes more important.

When the ionization chamber scans the beam along the 4 mm diameter of its sensitive volume, whether placed sideways or upright in the beam, the measurements obtained are essentially equal. However, given the larger dimensions, the measured fall-off is less steep than that obtained with the other detectors. As expected, by far the worst profile is measured when scanning along the length of the longitudinally placed ionization chamber. Only for the central axis measurements is the detector fully irradiated by the beam. Off-axis measurements result in partial detector irradiation, making the dose too low when the reference point of the chamber lies

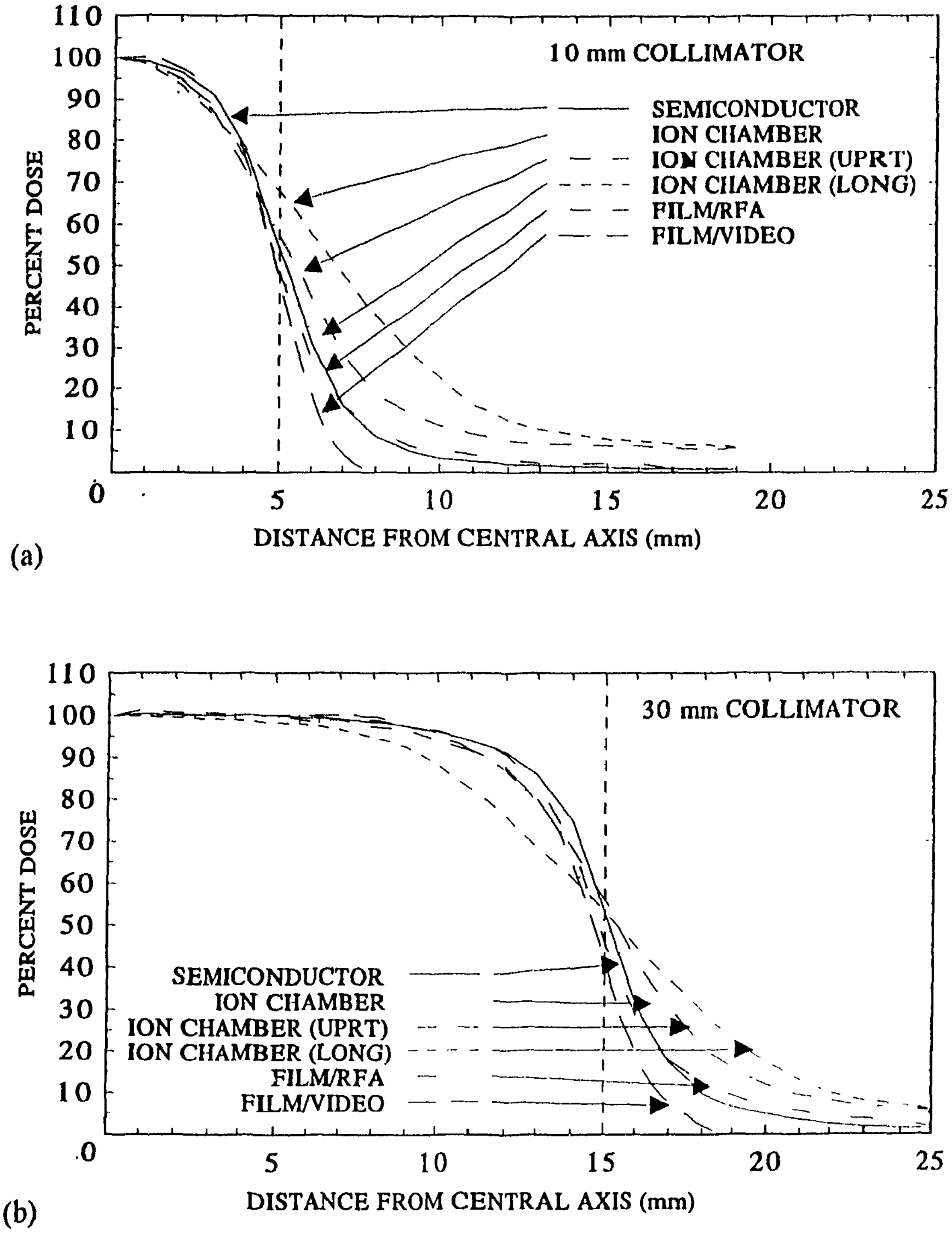

FIGURE 3.5. Dose profiles as measured with a variety of detectors at a depth of 2.5 cm in a tissue equivalent phantom with a 10 mm diameter collimator in part (a) and a 30 mm diameter collimator in part (b).

within the beam, and too high when when it lies outside of it.

The importance of choosing a suitable detector becomes clear from these measurements. The smaller the detector's sensitive volume, the greater is its ability to measure sharp edges and the smaller is the observed tail effect. As field size decreases, measurement dependency upon detector size and resolution plays an increasingly important role. Based on the profiles of Fig. 3.5 we conclude that the film/video dosimetric system gives the best measurement resolution. The film densitometer system and diode are a close second and still could be used with some confidence. The ionization chambers, however, should be used in radiosurgical profile measurements with great caution because of their relatively large sensitive volumes which degrade their spatial resolving power.

Dose profiles measured at different depths in phantom are shown in Fig. 3.6 (a) and (b) for the 1 cm and 3 cm diameter collimators, respectively. The off-axis ratios (OAR) were measured with the film/video dosimetric system, which, as shown in Fig. 3.5, was the most suitable detector for small radiosurgical fields. The depths of measurement were chosen at 2.5 cm, 10.5 cm, 18.5 cm and 26.5 cm. These profiles measured with 8 cm depth intervals beyond the depth of dose maximum correspond to the profile data requirements of the dose calculation algorithm we commonly use in radiotherapy (5). The graphs show the divergence of the beams, which can be considered as originating from a point source. At a depth in phantom of 265 mm, the diameter of the beam profile is 80 mm wider than the diameter of the profile measured at the depth of dose maximum.

3.5 Percent depth dose measurements

In radiotherapy, the dose deposited by a radiation beam as it penetrates through a medium is described by a percent depth dose curve (PDD). This curve is measured on the beam central axis and gives the relative dose deposited by the beam as

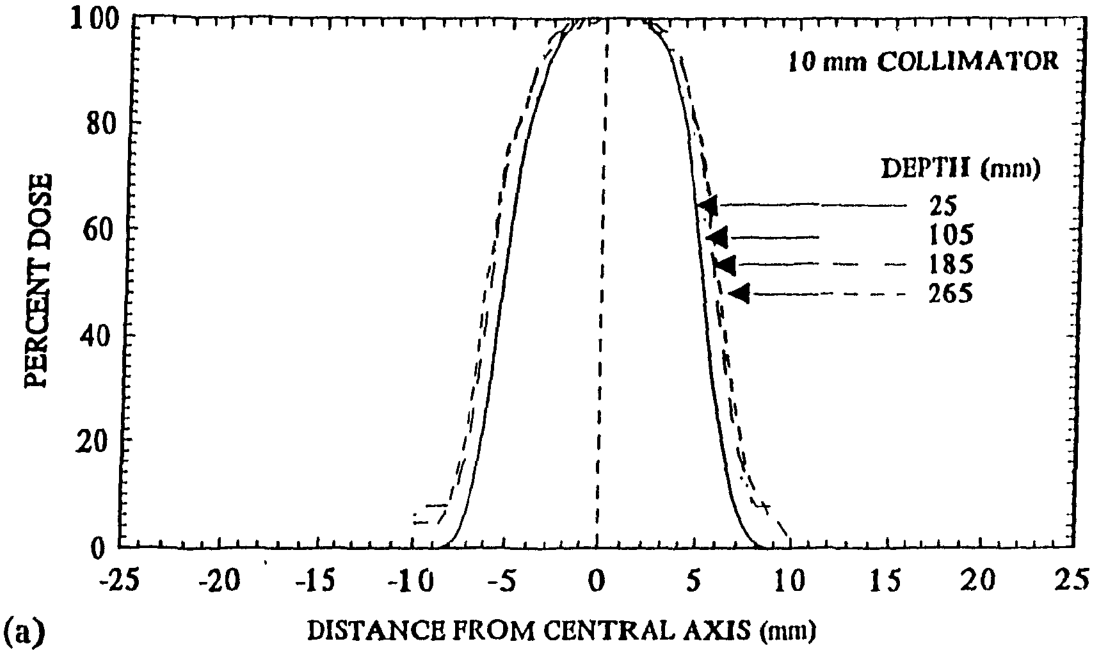

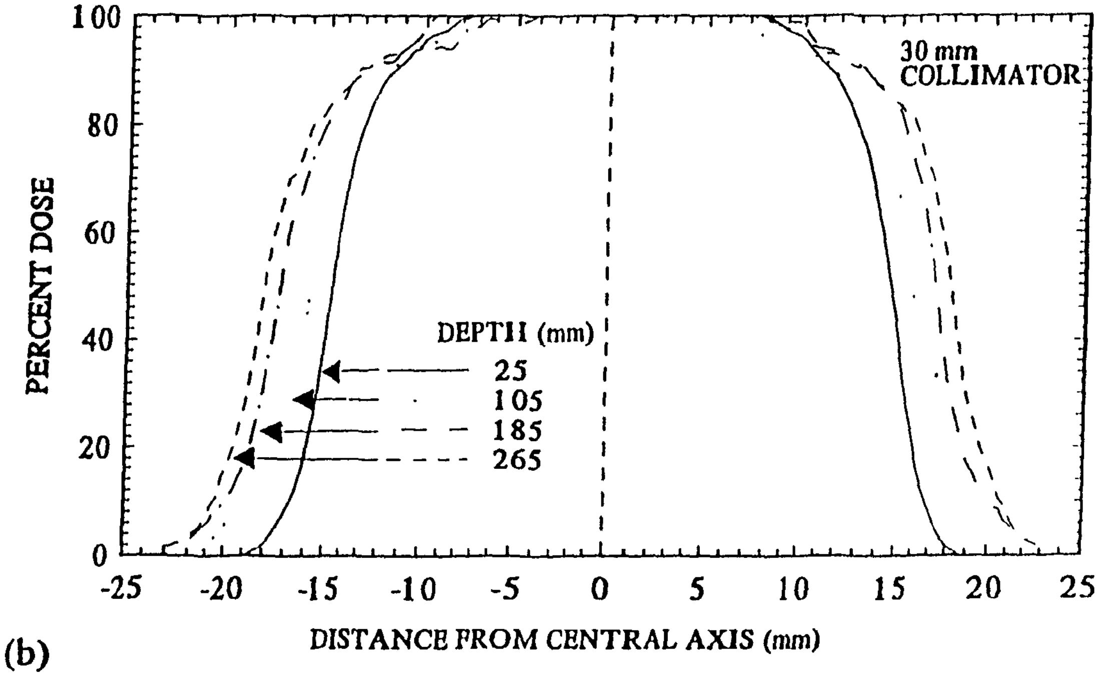

FIGURE 3.6. Off-axis ratios measured with the digital imaging densitometry system at four depths in polystyrene phantom: 25 mm, 105 mm, 185 mm and 265 mm. Part (a) 10 mm diameter collimator and part (b) 30 mm diameter collimator.

a function of depth in the medium. The dose is normalized to the maximum value occuring at the depth of dose maximum (d_{max}) and quoted as a percentage. Measurement of percent depth doses for the radiosurgical beams were made with the detectors described in Chapter 2. Film was used as a detector and subsequently analysed with the RFA densitometer. The parallel plate ionization chamber was also used, as were both the semiconductor and the thimble ion chamber of the RFA isodose plotter. All measurements were made in tissue equivalent phantoms at an SSD of 100 cm, to a depth of ~20 cm. This depth was deemed sufficient, since radiosurgery is performed on the brain with a maximum separation of less than 20 cm.

Sheets of radiographic film were placed between layers of the polystyrene phantom and oriented parallel to the beam. This allowed the measurement of a two dimensional dose distribution with depth along the length of the film. To verify that the thin layer of silver on the film did not affect the attenuation of the beam, a few films were placed into the phantom perpendicularly to the beam and irradiated. Percent doses were then compared at specific depths for the parallel and perpendicular orientation of the films and were found to be identical. Films were analysed with the RFA densitometer. For practical reasons the video analysis system was not used in percentage depth dose measurements. The system was specifically designed to image small areas with the camera's field of view having a diameter of only a few cm. The films used in the PDD measurement of the radiosurgical beams were 20 cm in length and thus too large for the camera to aquire their images for analysis. Furthermore, since the PDD curves do not contain sharp edges, the spatial resolution of the RFA densitometer proved to be sufficient.

In the build-up region the depth doses were measured with a Farmer parallel plate ionization chamber. The build-up region of a photon beam is defined as the region extending from the surface of the medium to a depth d_{max} where the dose attains its maximum value and electronic equilibrium has been reached (6). The dose gradients in this region are generally very steep, as the depth of dose maximum is reached at a depth of a few mm to a few cm, depending on the beam energy. Thus a thin wall chamber with a thin sensitive volume has the depth resolution needed to measure the doses in this region.

Establishing d_{max} accurately is very important for subsequent depth dose measurements with other detectors, such as diodes and ionization chambers. The geometry and wall thickness of these detectors do not allow dose measurements in the build-up region. At depths beyond d_{max}, however, they give excellent and accurate results provided that they are properly used. This requires that their cross-section perpendicular to the beam central axis is relatively small compared to the beam cross-section at a given depth in phantom and, moreover, that the position of the reference point in the detector is well known. These two conditions are met for both the diode and the cylindrical ionization chamber by orienting the chamber axis along the beam central axis. The position of the chamber reference point is on the chamber axis for both the diode and the ionization chamber. The exact position is easily determined for the diode as the sensitive volume is only 60 μm thick, for the ionization chamber, on the other hand, which has a length of ~10 mm, we determined the reference point position experimentally. For small diameter radiosurgical fields, the ionization chamber must be used in the parallel orientation. To determine the depth position of the reference point in this orientation, we match the depth dose curve obtained with the parallel plate ionization chamber to that measured with the RFA ionization chamber for a 10x10 cm^2 field. Once the depth position of the reference point of the RFA chamber in the parallel orientation is known, the depth doses for our set of radiosurgical collimators were relatively easily measured.

Figure 3.7 shows the percent depth dose curves measured with a variety of detectors. The curves for the 1 cm diameter collimator in part (a) and for the 3 cm diameter collimator in part (b) exhibit typical PDD behaviour, a rapid rise to d_{max} and a slow fall off which is essentially exponential. Measurement with all detectors for a particular collimator result in PDD curves within a few percentage points of each other. The 1 cm collimator PDD curve measured with the ionization chamber shows a slight deviation from data obtained with other detectors, indicating an error

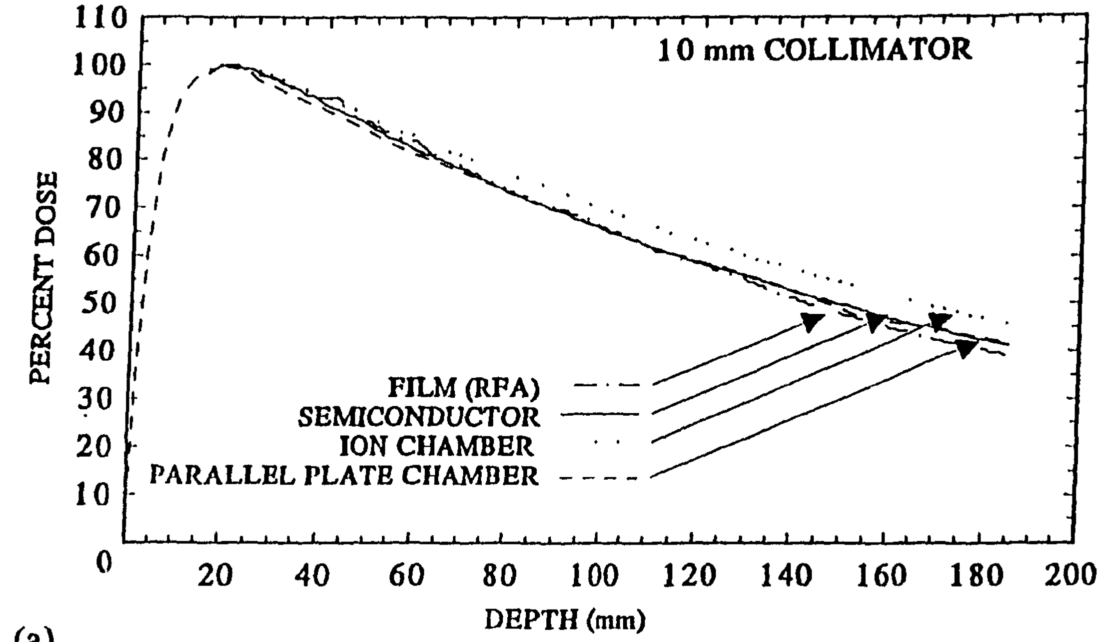

(a)

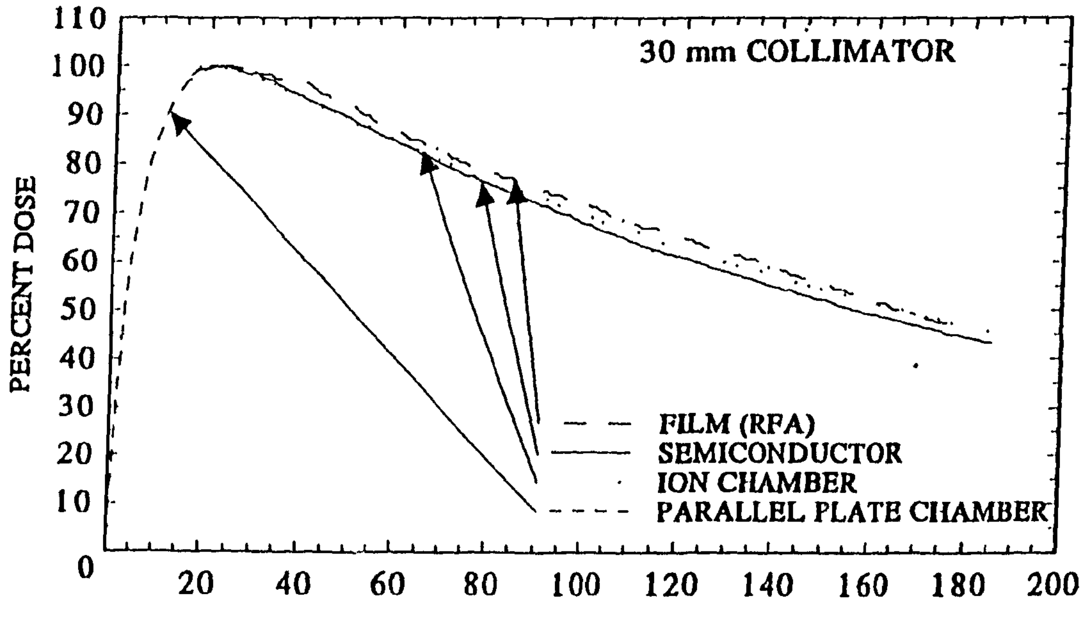

(b)

FIGURE 3.7. Percentage depth doses measured with a variety of detectors in a tissue equivalent phantom for (a) 10 mm diameter collimator and (b) 30 mm diameter collimator.

from the average measurements of ~5 %. However, in general all the detectors used are suitable for these measurements. An average of these curves is used as basic data for the computerized treatment planning in radiosurgery.

In Fig. 3.8 we plot the average PDD data for several field sizes. Shown are two radiosurgical fields, with a 10 mm and a 30 mm diameter, and a standard 10x10 cm^2 radiotherapy field. Because of its smaller field size, the 1 cm PDD curve falls off at a slightly steeper rate than the 3 cm PDD curve, and both curves are steeper than the large 10x10 cm^2 field. PDD data for radiosurgical fields of diameters between those shown, fall between the 10 mm and 30 mm collimator curves. The surface doses for all collimators were 8%, the depths of dose maximum, however, depend on field size. This dependence will be discussed in section 3.7 below.

3.6 Relative dose factor, scatter factor and collimator factor

In general, the dose measured at any depth in phantom along the central axis of a radiation beam consists of both primary and secondary dose. The primary dose is determined by the photon fluence of the primary beam, which can be considered as originating from a point source, and is field size independent. The scattered dose, on the other hand, is proportional to the collimator field size and to the volume of the irradiated phantom. Any change in beam parameters is a result of a change in the scatter dose. This scatter can be separated into two components, the scatter originating from the collimator and the scatter originating in the phantom itself (7).

The total change in dose rate as a result of a change in field diameter is given by the relative dose factor (RDF). The change is relative, comparing the dose rate measured at the depth of dose maximum d_{max} in phantom for an arbitrary field size r to that for a standard 10x10 cm^2 field and is as given by the equation

$$RDF(r) = \frac{D_{max}(r)}{D_{max}(10\times10)} , \qquad (3.1)$$

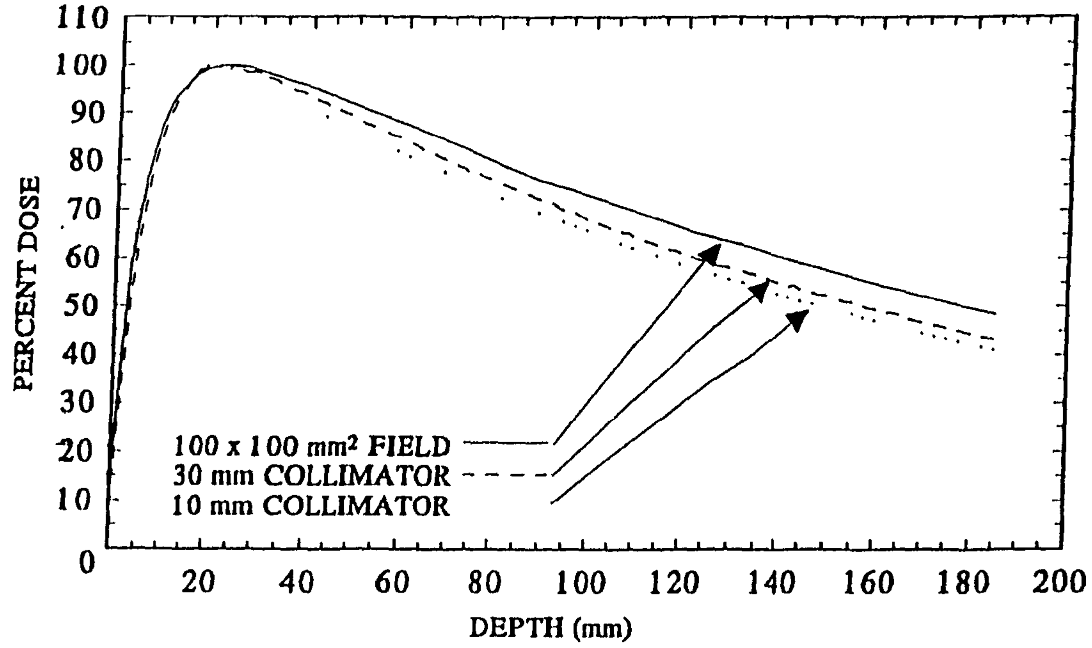

FIGURE 3.8. Average percentage depth doses measured in a tissue equivalent phantom with a variety of detectors for several field sizes: 10 mm diameter collimator, 30 mm diameter collimator and a 10x10 cm^2 field.

where the subscript denotes that the point of measurement is at d_{max} in phantom. RDF is measured with an SSD of 100 cm. Deviations in this factor from 1.0 are a result of a change in scatter from both the phantom and the collimator. The relative dose factor can also be expressed in terms of its contributors, i.e., in terms of factors reflecting changes in collimator scatter and factors reflecting changes in phantom scatter, given by the collimator factor (CF) and scatter factor (SF), respectively. The RDF (r) can then be expressed as follows:

$$\mathrm{RDF}(r) = \mathrm{SF}(r)\,\mathrm{CF}(r)\ . \tag{3.2}$$

The collimator factor, which gives the relative change in dose due to a change in collimator size only, is given by equation

$$\mathrm{CF}(r) = \frac{D'_{max}(r)}{D'_{max}(10\times10)}\ , \tag{3.3}$$

where the prime in Eq. (3.3) denotes doses to a small mass of medium measured in air. The CF for collimator size r is, similarly to the RDF(r) of Eq. (3.1), normalized to CF(10X10 cm^2) =1. The doses to a small mass of medium can be measured with a suitable detector and a build-up cap at a distance of (SSD + d_{max}) from the source. Collimator factors reflect a change in collimator scatter due to a change in collimator surface area exposed to the primary beam.

In our experiments, the collimator factors were measured in air for the collimators ranging in diameter from 1.5 cm to 3.0 cm in steps of 0.5 cm, with the semiconductor detector and the brass build-up cap discussed in Sec. 2.5. Collimator factors for fields smaller than 1.5 cm diameter were found by extrapolation. The measurements of relative dose factors were made with several detectors and the results averaged. Scatter factors were then calculated using Eq. (3.2).

The results of these measurements and calculations are given in Table 3.1. Both the relative dose factor and the scatter factor have a very strong dependence on

Collimator diameter (mm)	RDF (r)	CF (r)	SF (r)
10	0.73	0.94	0.77
15	0.81	0.94	0.86
20	0.86	0.94	0.91
25	0.90	0.94	0.96
30	0.91	0.94	0.97
100x 100	1.00	1.00	1.00

TABLE 3.1. The relative contributions to scatter into various components, relative dose factor, collimator factor and satter factor for different radiosurgical field sizes. Data for a standard 10X10 cm^2 radiotherapy field is included for comparison.

the field size. The collimator factor, on the other hand, remains constant for fields between 1.5 cm and 3 cm in diameter and increases only for fields larger than 3 cm. The relative dose factors are used, in conjunction with percentage depth dose data and the off-axis ratios, in the computerized calculation of dose distributions in radiosurgery and in the subsequent calculation of the monitor units required on the linac to achieve the prescribed target dose.

3.7 Depth of dose maximum

A closer look at the depth dose curves in Fig. 3.8 shows that the smaller field size (1 cm diameter) has a shallower depth of dose maximum compared to the larger field size (3 cm diameter). In conventional radiotherapy, a change of d_{max} with field size is a well known phenomenon. As the collimator jaws widen the field size increases and more surface area of the collimator is exposed to the primary beam. The dense, high atomic number collimator material produces secondary scatter, both electron and photon, primarily through the Compton interaction of the photons with the collimator surface. Some of this scattered radiation reaches the phantom or the patient but has a lower energy than the primary photons, thereby softening the beam spectrum. The softer the photon beam, the less penetrating it is and the shallower is its depth of maximum dose (8,9). For large field sizes it has been shown by applying a magnetic field over the region of the x-ray beam, that electrons account for an additional contribution to the dose in the build-up region, causing a shift in d_{max} (9).

However, the change in d_{max} observed with the small diameter radiosurgical beams is opposite to what was found for large fields, since in small fields the depth of d_{max} decreases with decreasing field size. The effect is shown clearly in Fig. 3.9 where the percent depth doses for a 1 cm collimator and a standard 10x10 cm^2 radiotherapy field are plotted in the build-up region for the two fields. It is obvious that the two fields do not have the same depth of dose maximum.

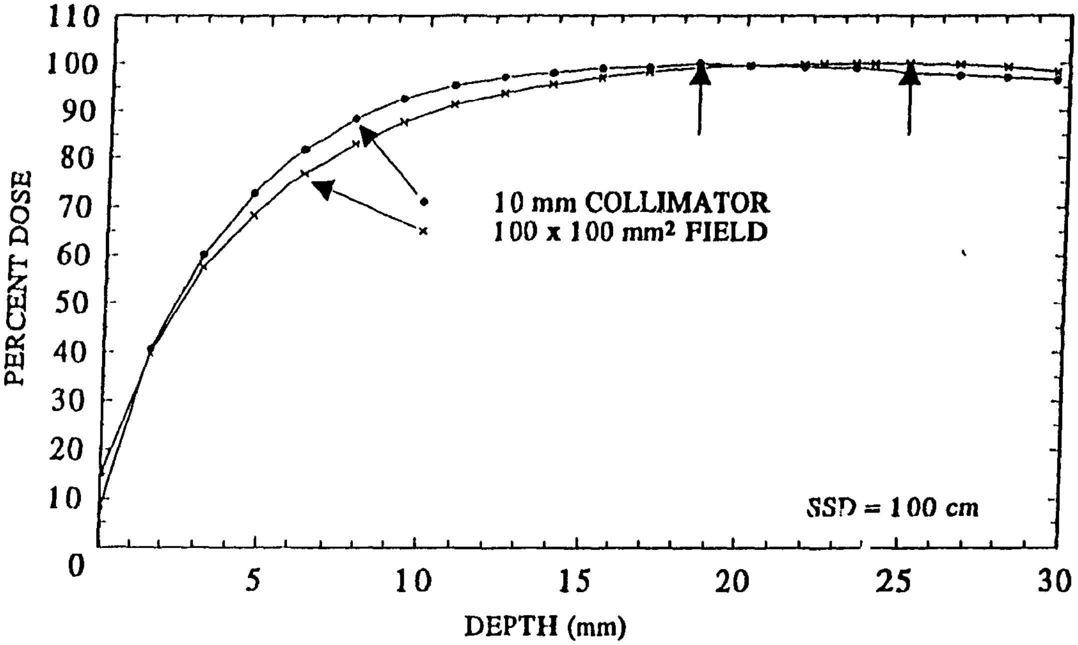

FIGURE 3.9. Percentage depth doses for a 1 cm diameter collimator and a 10x10 cm^2 square field measured with a parallel plate ionization chamber in a polystyrene phantom at an SSD=100 cm. Shown is the build-up region for both fields from the surface of the phantom to a depth of 30 mm.

The dependence of d_{max} on collimator size was observed for all radiosurgical collimators. Table 3.2 lists the measured depths of dose maximum for various radiosurgical field sizes and Fig. 3.10 shows a plot of this data with data for the $10x10\ cm^2$ field included for comparison. Data for collimators with diameters smaller than 10 mm are not included in the table, as the parallel plate ionization chamber which was used to determine d_{max} had a larger diameter than these field sizes. The measured d_{max} range from 18.5 mm for the 10 mm collimator to 23.4 mm for the 30 mm collimator. The d_{max} for the 30 mm collimator is very close to the d_{max} of 25 mm measured for the $10x10\ cm^2$ field, indicating that the effect of d_{max} shift is only pronounced for very small field sizes. Given the scale set by beam diameters, the change in d_{max} is sizable and largely unexpected.

The data giving the relative contribution of scatter to the dose measured, as listed in Table 3.1, can be used to understand the shift in d_{max}. We have seen that scatter originating in the collimator remains constant for the small radiosurgical fields, while the scatter factor and with it the relative dose factor change rapidly with field size. Furthermore, the percentage surface dose for all small radiosurgical fields is essentially constant with a value of 8%. These measurements suggest that the observed shift in d_{max} cannot be attributed to scatter events originating on the collimator's inner surface area, i.e., the effect is not a result of collimator scatter. Instead, judging from the rapid change in scatter factor, the shift must be a result of scattering events occuring within the phantom.

To confirm the lack of dependence of d_{max} on exposed collimator surface area, the build-up region for two fields giving an equivalent beam area but having different collimator surface areas was measured. The results are shown in Fig. 3.11 where we plot the percentage depth doses in the build-up region for a $17.7X17.7\ mm^2$ square field, defined by the standard linac collimator, and for a 20 mm diameter circular field, defined by the 20 mm diameter radiosurgical collimator The square field has a perimeter of 7.1 cm and an area of $3.14\ cm^2$, while the circular collimator has the same field area but a perimeter of only 6.3 cm. However, it is clear from the

Collimator diameter (mm)	d_{max} (mm)
10	18.5
15	20.1
20	20.9
25	22.7
30	23.4
100 x 100	25

TABLE 3.2. Depth of dose maximum measured in a tissue equivalent phantom with a parallel plate ionization chamber for several radiosurgical field sizes. The depth of dose maximum for the 10X10 cm^2 field is included for comparison.

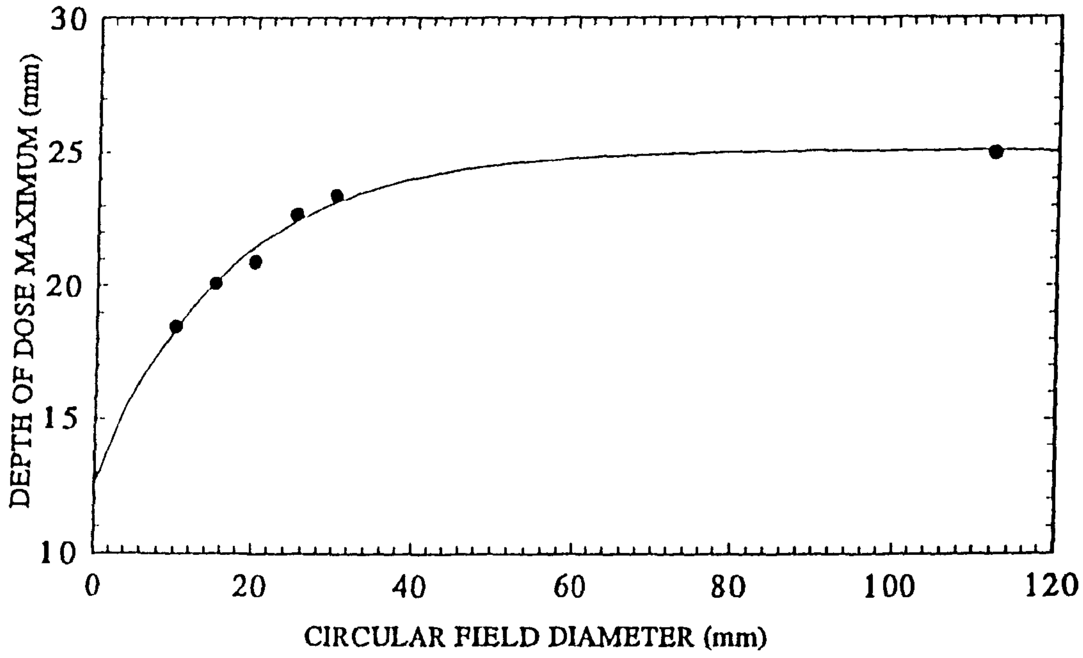

FIGURE 3.10. Depth of dose maximum plotted as a function of circular field diameter.

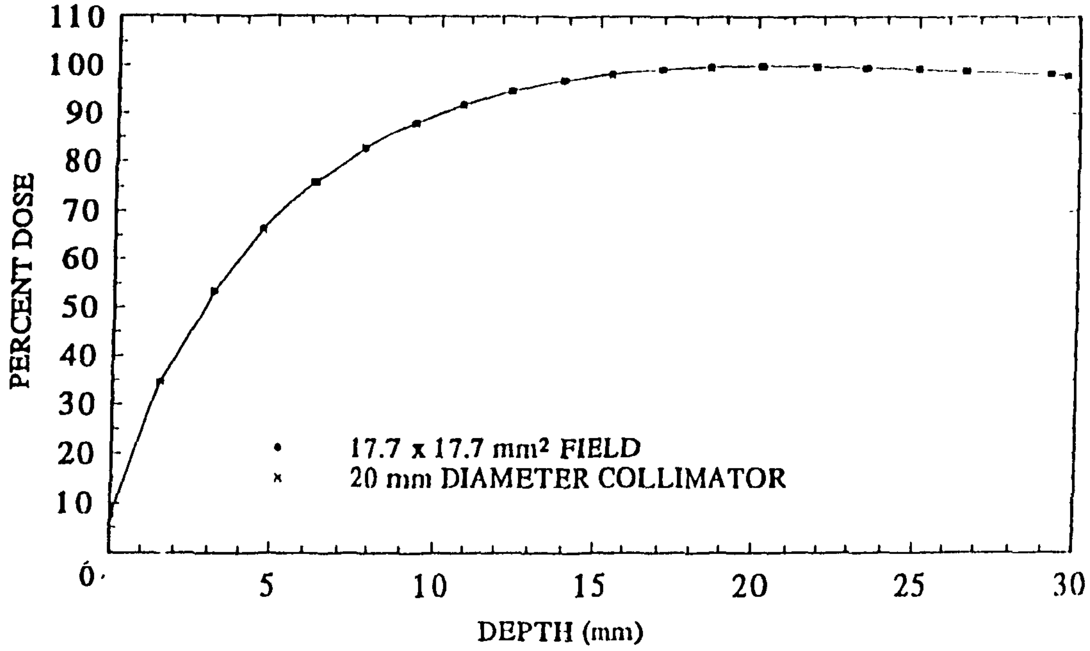

FIGURE 3.11. Percentage depth doses in the build-up region for an equivalent square field (17.7X17.7 mm^2) and a circular field (20 mm diameter) as measured with the parallel plate ionization chamber in a polystyrene phantom. Both fields have an area of 3.14 cm^2.

comparison of measured data that the build-up regions for the two fields are identical, from the same surface dose to the same depth of dose maximum. We conclude that scattering events occuring in the phantom are far more important for the shift in d_{max} than any effects resulting from the collimator.

To further verify that electron contamination from the additional collimators, which are relatively close to the isocenter, does not occur, a thin sheet of acrylic was placed just below the collimator and the depth dose measurements were repeated. Any electrons originating from the lead collimators would be filtered by the acrylic, while the photon beam would pass essentially unhindered. This was done for the 1 cm collimator and no change in the measurement of the position of d_{max} was observed.

From the measurements discussed above, it is clear that the observed shift in d_{max} must be caused by effects occuring in the phantom, as we have established that it cannot be attributed to collimator scatter, either photon or electron. The shift is a short range effect and is observed only for small field sizes. At a field diameter of 3 cm the depth of dose maximum is very close to that of a 10x10 cm^2 field. Furthermore, the shift that is observed is of the order of 0.5 cm which is a significant fraction of d_{max}, approximately 1/5 of the depth of maximum dose for a standard 10x10 cm^2 radiotherapy field. The short range aspect suggests that the effect is a result of the scatter and distribution of electrons rather than photons in the phantom.

Other groups, such as Rice et al. (10) and Arcovito et al. (11), observe a similar change in the depth of dose maximum, however, neither give a detailed explanation to account for the effect. Rice et al. suggest the effect is a result of a lack of lateral electronic equilibrium, while Arcovito et al. believe the shift to be caused by photons scattered in the phantom. To obtain a more in depth explanation, we examine the interactions occuring in the phantom for the given photon beam.

The spectrum of the 10 MV accelerator can be calculated through Monte Carlo calculations (12). It contains photons with energies from 0 to 10 MeV, most photons, however, have energies between 1 and 3 MeV. For these incient photon energies, Compton scattering is by far the most probable form of interaction with the medium, as over 98% of all interactions occur through this effect. Even for photon energies of 10 MeV, 80% of interactions are still through Compton scattering (13). Thus in the first approximation in our situation we take only Compton scattering into account. We consider the angular distribution of Compton scattered electrons and their corresponding energy to know in what direction and how far the Compton recoil electrons travel in the scattering medium.

In general, the equations describing the Compton interaction of a photon with an electron are given as a function of the photon scattering angle θ, defined from 0° to 180°. 0° corresponds to the direction of the incident photon (forward scattering) and 180° corresponds to a backscattered photon. As we are interested in the direction and energy of the recoil electron, the equations can easily be expressed in terms of ϕ, the electron scattering angle. The relationship between θ and ϕ is given by:

$$\cot\phi = (1+\varepsilon)\tan\frac{\theta}{2}\ , \tag{3.4}$$

where ϕ is defined from 0° to 90°, and ε is the initial photon energy $h\nu$ normalized to the electron rest mass m_oc^2:

$$\varepsilon = \frac{h\nu}{m_oc^2}\ . \tag{3.6}$$

The differential scattering cross-section $d\sigma/d\phi$, which gives the differential cross-section per electron per unit scattering angle ϕ, is given as follows:

$$\frac{d\sigma}{d\phi} = \frac{2\pi\sin\phi\, 4\, r_o^2\,(1+\varepsilon)^2\cos\phi}{(1+2\varepsilon+\varepsilon^2\sin^2\phi)^2} \tag{3.5}$$

$$\times\left[\ 1+\frac{2\varepsilon^2\cos^4\phi}{(1+2\varepsilon+\varepsilon^2\sin^2\phi)(1+\varepsilon(\varepsilon+2)\sin^2\phi} - \frac{2(1+\varepsilon)^2\sin^2\phi\cos^2\phi}{(1+\varepsilon(\varepsilon+2)\sin^2\phi)^2}\right],$$

where r_0 is the classical electron radius (~2.8 fm).

The relationship expressed in Eq. (3.5) is plotted as a function of the electron scattering angle ϕ for various incident photon energies in Fig. 3.12. At low incident photon energies the distribution of the differential cross section is quite symmetric. As the incident photon energy increases, however, the distribution becomes more and more peaked in the forward direction. At very high energies almost all electrons are scattered between 0 and 10 degrees. It is also seen from this graph, that the total cross section, i.e., the probability for the effect to occur, as given by the area under the curves, decreases rapidly with the increasing incident photon energy.

As discussed above, the photon beam from a linear accelerator consists of a spectrum of energies. Thus, to know the differential cross-section for the photon beam from the 10 MV accelerator, we must integrate the differential cross-section for individual photon energies over the energy spectrum. Using the calculated spectrum from Mohan, Chui and Lidofsky (12), we find the sum of all cross-sections, weighted by the probability of the incident photon having an energy between hν and hν+Δhν, as given by the following equation:

$$\frac{d\sigma}{d\phi} = \sum_i w_i \frac{d\sigma}{d\phi}(h\nu_i, \phi)\, \Delta h\nu \;, \tag{3.7}$$

where w_i is the probability per MeV of the photon having and incident energy between hν and hν+Δhν.

The results of this calculation for our 10 MV photon beam are shown in Fig. 3.13, which gives the differential cross section $d\sigma/d\phi$ as a function of electron scattering angle ϕ. Again we see a distribution which is strongly peaked in the forward direction, with a maximum probability for ϕ=~8° and a fairly rapid fall-off as ϕ increases toward 90°. Most recoil electrons are thus scattered essentially in the forward direction.

Next, we are interested in how far these electrons can travel in a tissue equivalent phantom. The kinetic energy KE of the recoil electron as a function of its

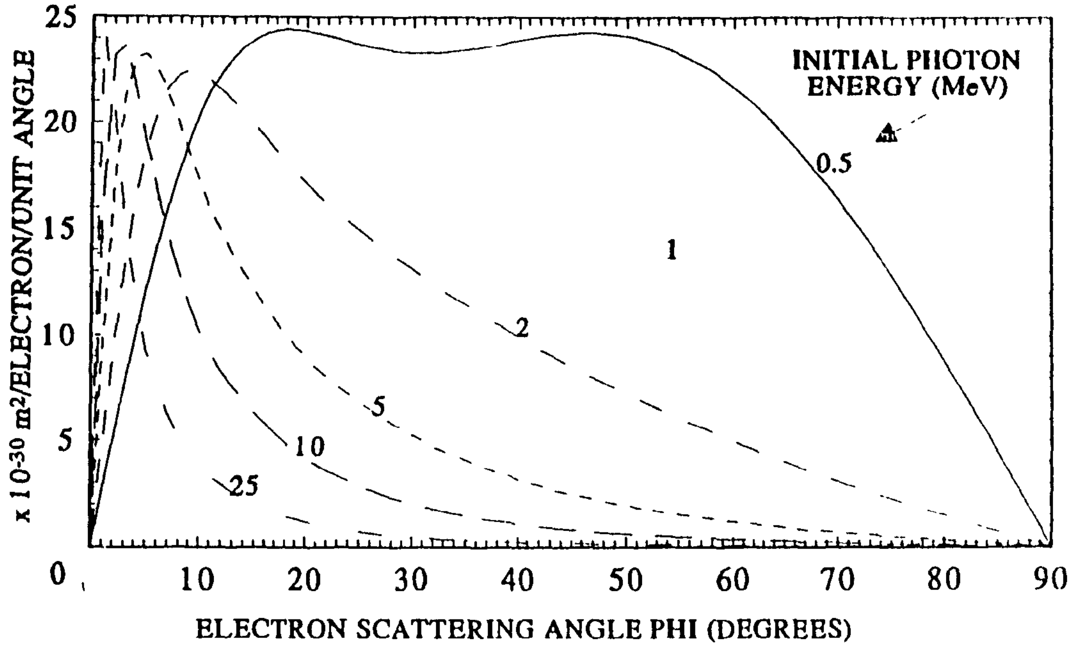

FIGURE 3.12. Compton differential scattering cross-section calculated for various incident photon energies as a function of electron scattering angle ϕ.

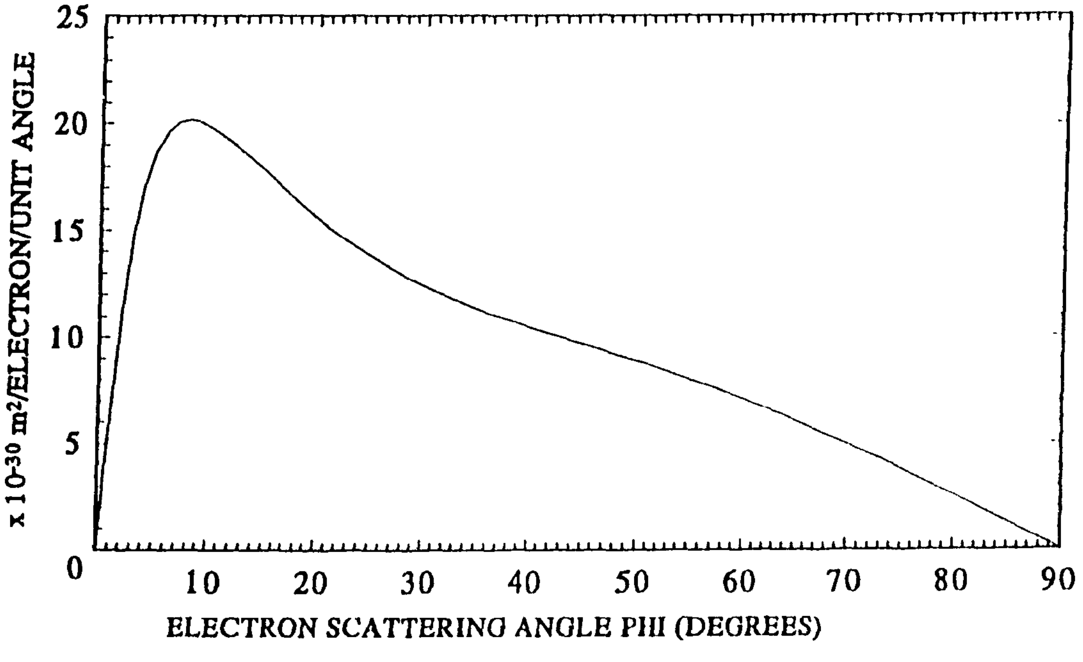

FIGURE 3.13. Compton differential scattering cross-section calculated for the x-ray energy spectrum of a 10 MV linear accelerator as a function of electron scattering angle ϕ.

scattering angle for a fixed incident photon energy hv is, according to the Compton relationship, given by:

$$KE = \frac{2\,h\nu\,\varepsilon\cos^2\phi}{(1+\varepsilon)^2-\varepsilon^2\cos^2\phi}\ . \tag{3.8}$$

Again we use the 10 MV linac spectrum to find the probability per MeV that an electron which is scattered at a given angle ϕ will have a particular range R in a medium. With the use of tabulated range data for electrons in water (14), the kinetic energy information can be expressed in terms of electron range R. Figure 3.14 shows the probability per MeV that an electron scattered at a fixed angle ϕ will have a particular range R. As the scattering angle increases, the probability of the electron having a large kinetic energy and correspondingly a large range, decreases. At small angles the electrons have a substantial chance of having ranges of a few centimeters, while the maximum range of electrons scattered at angles greater than 50° is less than 2 mm.

Figure 3.13 suggests that the most probable electron scattering angle for Compton electrons produced by 10 MV incident photons is ~8°. The average range of electrons scattered at this angle is 1.7 cm in tissue. The probability of scatter increases in the forward direction and the range of the electrons that are scattered in this direction increases. Those electrons that do get scattered in more lateral directions, on the other hand, have a very short range, as shown in Fig. 3.14.

To fully explain the observed field size dependence of the depth of dose maximum, a Monte Carlo calculation would be required at this point to follow the paths of each Compton recoil electron, thereby determining exactly where the dose is deposited with respect to the central axis. This lies beyond the scope of our present work, but using the above information on Compton scattering, it is possible to at least qualitatively explain the effect as shown below. We use the schematic diagram of Fig. 3.15 to help understand the argument. An assumption is made that all electrons are scattered at 8° and that they all have a straightline range of 1.7 cm in tissue. For small

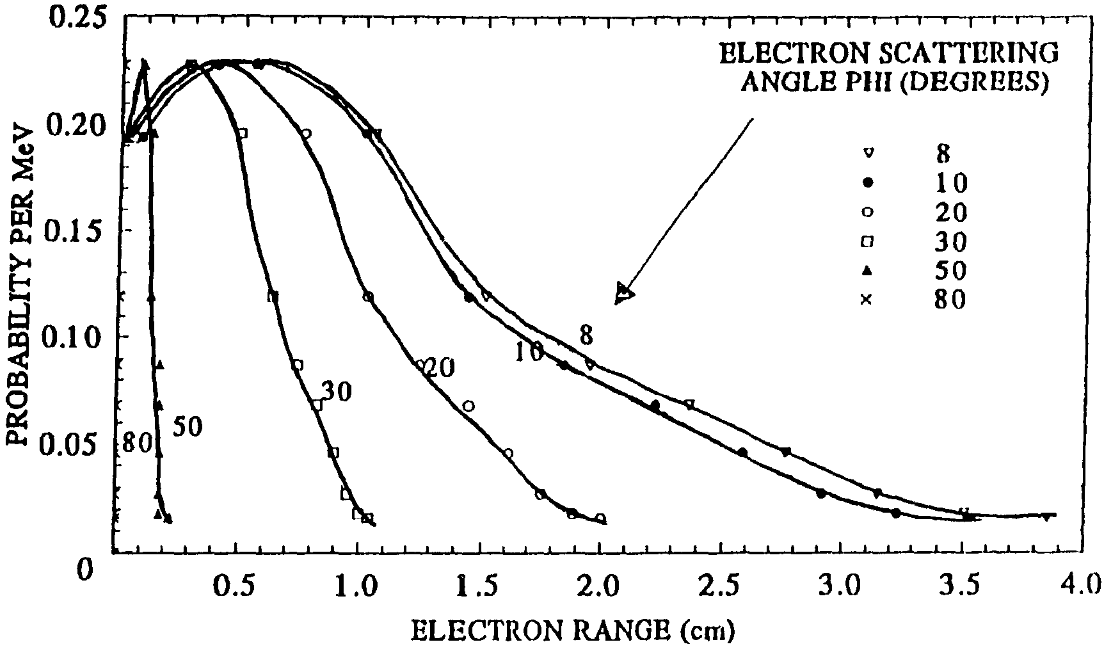

FIGURE 3.14. Probability per MeV that a Compton recoil electron scattered at a given angle ϕ will have a particular range R.

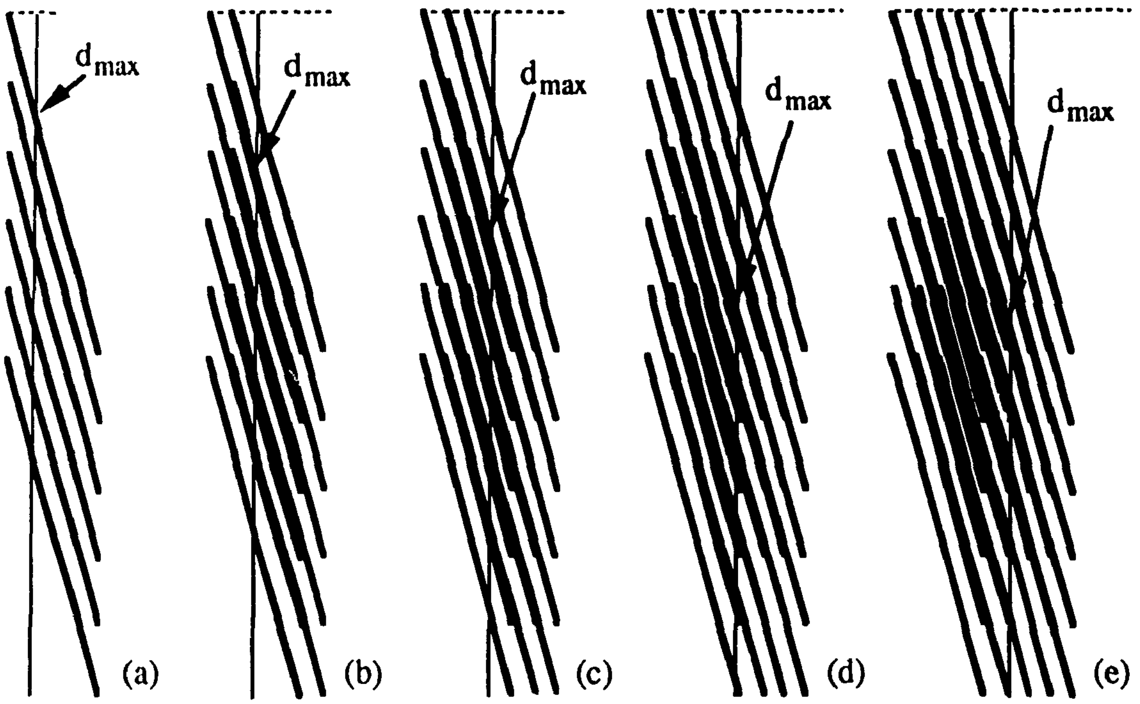

FIGURE 3.15. Schematic diagram explaining the observed shift in depth of dose maximum. Electrons are scattered at a most probable angle of ~8° with an average range of ~17 mm. In (a), (b), (c) and (d) as field size increases, the additional peripheral electrons contribute to the central axis dose, causing depth of dose maximum to increase. Yet if field size is further increased as in (e), the peripheral electrons will no longer have large enough range to reach the central axis, resulting in a saturation of the observed shift in d_{max}. The dashed horizontal line indicates the field size for each of the diagrams, and the solid vertical line represents the central axis.

field sizes, even recoil electrons produced at the edge of the field will cross the central axis, contributing to the dose at the central axis, as seen in Fig. 3.15 (a). As the field size increases as in Figures 3.15 (b), (c) and (d), the additional electrons originating in the increased volume of the irradiated phantom will also contribute to the central axis dose. However, for a scatter event at a given scattering angle (in our case ~8°), a greater lateral distance from the central axis implies a greater longitudinal distance from the origin of the scatter event to the point where the electron crosses the central axis. Thus the electrons originating farther from the central axis will contribute to the central axis dose at a greater depth. This is illustrated in Figures 3.15 (b), (c) and (d) where the depth of dose maximum becomes progressively deeper as field size increases. However, if the field size increases too much, this effect quickly saturates and the additional electrons originating in the peripherary of the larger field will no longer have enough energy to reach the central axis, as shown schematically in Fig. 3.15 (e). Thus the depth of dose maximum has a small value for small field sizes and increases as field size increases. At field sizes greater than the electron range the effect saturates and d_{max} reaches its highest value. This occurs at ~3 cm diameter fields. Of course this arguement presents a simplified picture of the actual event, yet it helps us to qualitatively understand the situation.

3.8 Summary

In this chapter physical parameters pertaining directly to radiosurgery were addressed. The equipment used for radiosurgical treatment was described. Modifications must be made to a standard linac to obtain the small field diameters required, to motorize the accelerator motions specifically the remotely controlled couch rotation, and to ensure the patient immobilization during treatment. Simple tests show that the spatial accuracy of dose delivery of linac-based radiosurgical techniques can be well within ±1 mm, the present limit of target localization techniques, provided that the equipment is in an excellent mechanical condition and provided that it is applied properly. Performing these tests prior to patient treatment is manditory and will ensure proper placement of treatment field collimators.

Measurements of radiosurgical photon beam parameters were discussed in this chapter. Both profile and percent depth dose measurements were examined as a function of the detector used. Detector choice proved to be of greatest importance when taking dose profile measurements, with the resolving power of the various detectors clearly reflected in the measured profile sharpness. Measurements with the digital film densitometer gave the steepest dose profiles. Percent depth dose measurements taken with all detectors showed good agreement with each other.

It was observed that the depth of dose maximum depends on the field size, becoming smaller with a decreasing field diameter. This is contrary to what is observed with conventional radiotherapy field sizes where the depth of dose maximum shifts towards the surface with an increase in field size. By measuring the various scatter components of the radiosurgical beams, it was shown that the shift cannot be attributed to collimator scatter, either photon or electron, but in fact is due to electron scatter originating in the phantom. The effect can be explained qualitatively using the probabilities of electron scatter as determined by Compton effect calculations in terms of the electron recoil angle and the corresponding electron kinetic energy or range.

3.9 References

1. T.M. Peters, J.A. Clark, A. Olivier, E.P. Marchand, G. Mawko, M. Dieumegarde, L.V. Muresan, and R. Ethier, **Integrated stereotaxic imaging with CT, MR Imaging and Digital Subtraction angiography**, Radiology **161**: 821-826, 1986.
2. H. Dahlin and B. Sarby, **Destruction of small intracranial tumours with Co 60 gamma radiation**, Acta Radiologica **14**: 209-227, 1975.
3. L. Walton, C.K. Bomford and R. Ramsden, **The Sheffield stereotactic radiosurgery unit: physical characteristics and principles of operation**, Brit. J. Radiol. **60**: 897-906, 1987.
4. E.B. Podgorsak, G.B. Pike, M. Pla, A. Olivier and L. Souhami, **Radiosurgery with photon beams: physical aspects and adequacy of linear accelerators**, Radiotherapy and Oncology **17**: 349-358, 1990.
5. J. Milan and R.E. Bentley, **The storage and manipulation of radiation dose data in a small digital computer**, Brit. J. Radiol. **47**:115-117, 1974.
6. H.E. Johns and J.R. Cunningham, **The physics of radiology**, 4th edition, Charles C. Thomas, Springfield, Illinois, 1983, pp. 220-223.
7. F.M. Khan, W. Sewchand, J. Lee and J.F. Williamson, **Revision of tissue-maximum ratio and scatter-maximum ratio concepts for cobalt 60 and higher energy x-ray beams**, Med. Phys. **7**: 230-237, 1980.
8. J.R. Marbach and P.R. Almond, **Scattered photons as the cause for the observed d_{max} shift with field size in high-energy photon beams**, Med. Phys. **4**: 310-314, 1977.
9. P.J. Biggs and C.C. Ling, **Electrons as the cause of the obseved d_{max} shift with field size in high energy photon beams**, Med. Phys **6**: 291-295, 1979.
10. R.K. Rice, J.L. Hansen, G.K. Svensson and R.L. Siddon, **Measurements of dose distributions in small beams of 6 MV x-rays**, Phys. Med. Biol.

32: 1087-1099, 1987.

11. G. Arcovito, A. Piermatti, G. D'Abramo and F.A. Bassi, **Dose measurements and calculations of small radiation fields for 9-MV x-rays**, Med. Phys. **12**: 779-784, 1985.
12. R. Mohan, C. Chui and L. Lidofsky, **Energy and angular distributions of photons from medical linear accelerators**, Med. Phys. **12**: 592-597, 1985.
13. H.E. Johns and J.R. Cunningham, **The physics of radiology**, 4th edition, Charles C. Thomas, Springfield, Illinois, 1983, p.163.
14. H.O. Wyckoff, Chairman, **Stopping powers for electrons and positrons**, ICRU report 37, 1984, p. 206.

CHAPTER 4

DOSE DISTRIBUTIONS OF RADIOSURGICAL TREATMENT TECHNIQUES

4.1 Introduction

In this chapter we briefly describe the 3-dimensional treatment planning system developed for radiosurgery at McGill by Pike et al. (1,2), and then discuss and compare the dose distributions resulting from several radiosurgical techniques currently in clinical use. Calculated isodose distributions are compared with measured ones for various radiosurgical treatment techniques. The McGill radiosurgical treatment planning system is capable of determining the dose distributions for all photon beam radiosurgical techniques including the Gamma unit. Measured dose distribution data were obtained by simulating treatments with the linear accelerator. In our convention, the 90% isodose surface is assumed to coincide with the target volume, while the 100% dose occurs at the isocenter. For the chosen treatment techniques, the minimum and maximum distance for the dose to decrease from 90% of the maximum dose to lesser values, such as 50%, 20% and 10%, was obtained. The ideal characteristic of the dose distributions is a rapid fall-off outside the target volume to low isodose values isotropically in all arbitrary directions.

First we discuss the principles of the McGill radiosurgical treatment planning system and then describe the process of obtaining measured isodose distributions. These measured distributions are used to verify the accuracy of the treatment planning program in calculating isodose distributions, and then to determine how closely the various techniques conform to the desired ideal distribution.

4.2 The McGill treatment planning system

In clinical radiosurgery the dose distribution must be known throughout the patient's brain, making the calculation of dose essentially a three dimensional problem. A method for calculating the dose distributions in three orthogonal planes (transverse, sagittal and coronal) through the target volume was developed and verified experimentally at McGill University by Pike et al. (1). This 3-dimensional treatment planning system can perform dose calculations for all modern photon radiosurgical techniques, including the Gamma unit, and all linac-based techniques, such as the single plane rotation, the multiple converging arcs with any arbitray number of arcs, and the dynamic rotation. The calculation is based on the well known 2-dimensional Milan and Bentley algorithm (3) for the calculation of tissue-maximum ratio (TMR) distributions, but accounts for the 3-dimensional geometry of the problem.

The algorithm follows the gantry and couch rotation in an incremental fashion and calculates the normalized TMR values over a matrix of points defined on a pre-selected plane (1). It uses a set of data measured in a tissue equivalent phantom for each individual beam to be used in radiosurgery, as discussed in Chapter 3. This data set consists of central axis depth doses and off-axis ratios (OAR) or dose profiles at several depths for each individual stationary circular beam. The depth and off-axis distance of each point-of-interest in the calculation is obtained from a patient surface database defined by a set of stereotactic computed tomography (CT) or magnetic resonance (MR) images. With this information, the dose at a point of interest Q can be calculated from the following equation:

$$D_Q(d,\Phi_Q) = P\left(d, \Phi_i \frac{f_i - d_i + d}{f_i + d}, f_i\right) \times \left(\frac{f_i + d}{f_i + d_{max}}\right)^2 \left(\frac{f_i}{f_i - d_i + d}\right)^2 \text{OAR}(d, r_Q) \;, \tag{4.1}$$

where d is the depth of point Q, d_{max} the depth of dose maximum, d_i the depth of the isocenter, f_i the source-axis distance (SAD=100 cm), Φ_Q the field diameter at point Q, Φ_i the field diameter at isocenter as defined by the circular collimator, P the interpolated percentage depth dose value at depth d for SSD equal to f_i and field size equal to $\Phi_i\,(f_i - d_i + d) / (f_i + d)$, and OAR (d,r_Q) the off-axis ratio for point Q at a depth d at a distance r_Q from the central axis. The normalization assumes that 100 cGy is given to a point at the isocenter with a field Φ and depth in phantom d_{max}. $D_Q(d,\Phi_Q)$ is thus the calculated tissue-maximum ratio (TMR) for the point-of-interest. An assumption is made that the TMR is independent of SSD (1). This is a reasonable assumption, considering the small changes in SSD, which occur when treating lessions within the brain. It is also assumed that tissue inhomogeneities (e.g. skull bone) will have little effect on the dose distribution.

Originally, the McGill planning system was developed on a large VAX computer equiped with array and display processors. To make the system more affordable and user-friendly a PC-based version of the system has been developed and integrated with a complete stereotactic image analysis system, capable of processing stereotactic MR, CT and DSA images (4,5). The basic hardware of the dose planning system consists of an IBM PC/AT compatible system running MS-DOS version 3.3. The system is equiped with a math co-processor, serial mouse, and an 80 MB hard disk. Images are displayed by means of an inexpensive 512x512x8 bit imaging board and a red-green-blue monitor. Image data are transferred to the system via an industry standard 9 track magnetic tape unit.

The program allows the choice of the treatment technique in terms of the number of individual arcs or rotations of the gantry, and the gantry and couch initial and final positions. Treatment field size and beam energy must be specified so that appropriate beam data are used in the calculation. Finally, the number of angular increments at which calculations are made must be specified for each arc of the chosen treatment technique. Typically, for the dynamic rotation and multiple converging arcs, calculations at increments corresponding to 10° steps in the gantry angle are sufficient to obtain a precise enough calculated dose distribution. For improved precision, a greater number of increments could be used, however, the calculation time then increases accordingly.

Isodose contours, as calculated for the orthogonal plane-of-interest which passes through the isocenter, are then directly superimposed on the corresponding image slice. This allows the user to see the calculated dose distribution resulting from a chosen treatment plan and technique. The TMR is calculated at the target center (which of course coincides with the linac isocenter) and the isodose lines are given as a percentage of this value, corresponding to 100% at the isocenter and 90% at the edge of the target. Distances between isodose lines can be measured directly from the displayed distribution, and dose fall-offs can then be calculated. The average TMR value for the isocenter is determined by calculating the TMR with Eq. (4.1) for each of the individual beams, summing the individual TMRs and dividing the sum by the number of beams. The average TMR is used in conjunction with the appropriate RDF for the given treatment collimator to calculate the monitor units or time needed for linacs or the Gamma unit, respectively, to deliver a prescribed dose to the isodose surface defining the target volume.

The treatment planning algorithm has been verified experimentally with thermoluminescent dosimetry (TLD) techniques in a humanoid phantom by Pike et al. (1). In our work we used a spherical phantom and film densitometry techniques for comparison of experimental radiosurgical isodose distributions with the ones calculated by the McGill radiosurgical software.

4.3 Dose distributions for various radiosurgical techniques

In this section we compare the calculated and measured isodose distributions for four clinically used radiosurgical treatment techniques: the single plane rotation, two converging non-coplanar arcs techniques (the eleven arcs used in Heidelberg and the four arcs used in Boston) and the dynamic rotation used at our center. The technical aspects of these techniques have been described in detail in Chapter 1. The calculations and measurements of dose distributions were performed for a spherical tissue equivalent phantom wih a radius of 8 cm. The spherical phantom was chosen to ensure generality by avoiding particular patient shapes, as well as to facilitate comparison with measured data.

We first calculate the dose distributions for the four radiosurgical techniques in three orthogonal planes: transverse, sagittal and cononal through the center of the sphere, for collimators with diameters of 1 cm, 2 cm and 3 cm. A typical set of isodose curves for the 1 cm diameter collimator is shown in Fig. 4.1 with the dose at the target center, which is also the isocenter of the linac, normalized to 100%. Isodose curves corresponding to 90%, 50%, 20%, 10% and 5% of the isocenter dose are shown. In some cases the lower percentage isodose curves extend beyond the areas shown on the figures. Ideally, the optimal dose fall-off would be obtained by irradiation in a 4π geometry, i.e., where the beam entry points are spread over the total surface area of the sphere (6).

The practical constraints of dose delivery in clinical set-ups, however, cause asymmetries in the resulting dose distributions. This anisotropy is most pronounced in Fig. 4.1 (a) which shows the distribution obtained with the single plane rotation. We see clearly the difference between the dose fall-off in the plane of ganty rotation, where we have a very poor dose fall-off and the dose fall-off in the plane perpendicular to the gantry plane of rotation where we see a very sharp dose fall-off. The shallow dose fall-off in the plane of rotation results from the large number of parallel-opposed beams in that plane. The 4 converging arcs technique of Fig. 4.1 (b) also shows a deviation from spherical symmetry, especially at low isodose curves. This asymmetry is also observed for the dynamic rotation technique shown in Fig. 4.1 (d). A closer observation, however, shows that the anisotropies in the two distributions occur only at isodose surfaces below 20%. The dose distribution for the 11 converging arcs technique is shown in Fig. 4.1 (c). This technique gives the most isotropic isodose distribution. Because of the large spherical segment covered by the 11 arcs during irradiation, the isodose surfaces, especially above 20%, appear almost spherically symmetric.

Although deviations from an isotropic dose distribution occur in all techniques, we see that the 4 converging arcs, 11 converging arcs and dynamic rotation result in a much better approximation to the ideal dose distribution than does

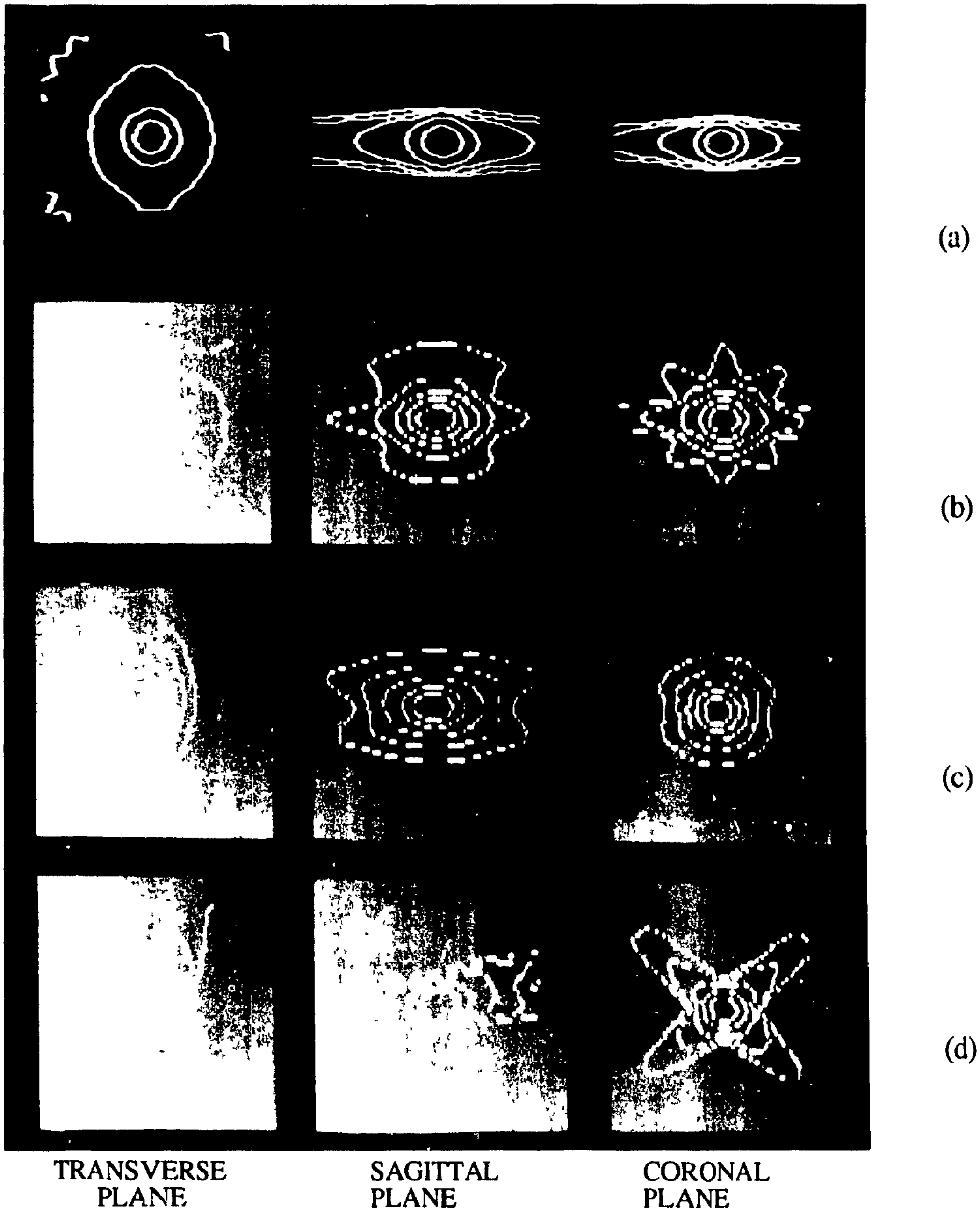

FIGURE 4.1. Isodose distributions in three orthogonal planes (transverse, sagittal and coronal) for several treatment techniques, (a) single plane rotation, (b) 4 converging arcs, (c) 11 converging arcs and (d) dynamic rotation, as calculated for an 8 cm radius spherical tissue equivalent phantom with the 1 cm diameter collimator. Shown in each distribution are the 90%, 50%, 20%,10% and 5% isodose curves. In some cases the 5% and even the 10% isodose curves continue beyond the limits shown in the figures.

the single plane rotation. Furthermore, for these techniques deviations from spherical symmetry are pronounced only at low level (< 20%) isodose surfaces.

To gain a more precise information on the dose fall-off and isotropy for the various radiosurgical techniques, we characterize the dose distributions by the steepest and shallowest dose fall-off curves outside the target volume. These dose fall-off curves, as calculated on the spherical phantom with the 1 cm diameter collimator, are plotted in Figures 4.2 and 4.3. We plot the two extreme dose fall-off, the steepest and shallowest curves for the single plane rotation in Fig. 4.2 (a), 4 converging arcs in Fig. 4.2 (b), 11 converging arcs in Fig. 4.2 (c) and dynamic rotation in Fig. 4.2 (d). The closer the two curves are to each other, the more isotropic is the dose distribution and the more suitable is the technique for radiosurgery. The shaded areas between the two curves represent the location of all intermediate fall-off curves.

To facilitate the comparison among techniques, the fall-off curves of Fig. 4.2 are plotted on a single graph in Fig. 4.3, with curve (a) corresponding to the single plane roation , (b) to 4 converging arcs, (c) to 11 converging arcs and (d) to dynamic rotation. Also plotted on this graph for comparison purposes are the two extreme dose fall-off curves for the Gamma unit, obtained from Walton et al. (7) and labelled as curves (e). As expected from the isodose distributions of Fig. 4.1, the steepest dose fall-off curve for single plane rotation is extremely sharp. The shallowest dose fall-off curve, however, shows a very gradual decrease in dose with distance from the target center. Comparing the single plane rotation fall-off curves to those of the Gamma unit in Fig.4.3, we see that the single plane rotation cannot be taken as a serious competitor to the Gamma unit. The shallowest dose fall-off curve is much worse than that of the commercially available Gamma unit.

Curves (b) and (c) of Fig. 4.3 represent the dose fall-offs for the 4 and 11 converging arcs techniques, respectively. In comparison to the single plane rotation, the multiple converging arcs techniques yield a steeper shallowest dose fall-off curve because the dose outside the target volume is spread over a larger volume and the

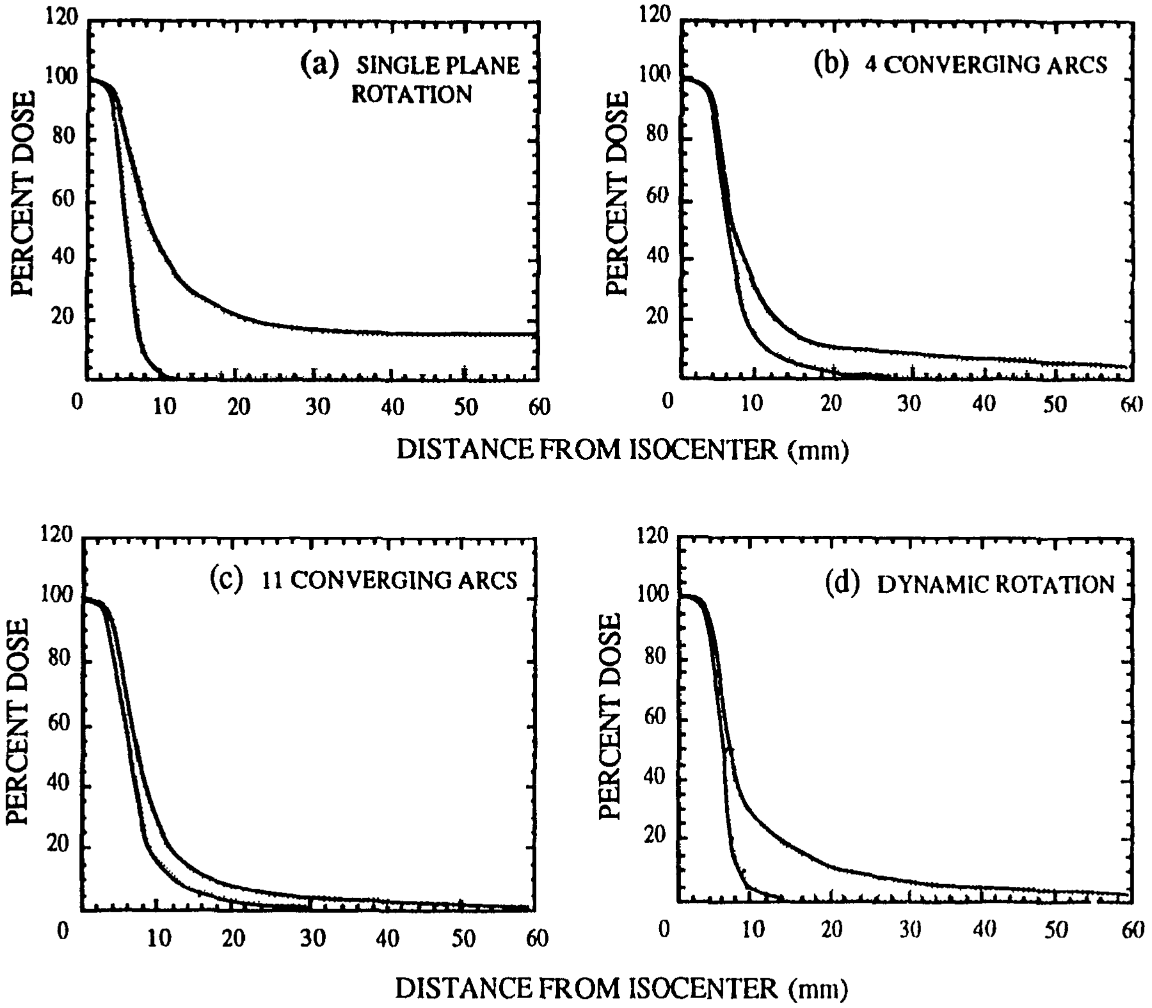

FIGURE 4.2. The steepest and shallowest dose fall-off curves for various linac-based radiosurgical techniques as calculated on a spherical phantom of radius 8 cm with the 1 cm diameter treatment collimator. Percentage doses are plotted as a function of distance, in mm, from the target center. All intermediate dose fall-offs lie in the shaded region between the two extreme curves. Shown are (a) single plane rotation, (b) 4 converging arcs, (c) 11 converging arcs and (d) dynamic rotation.

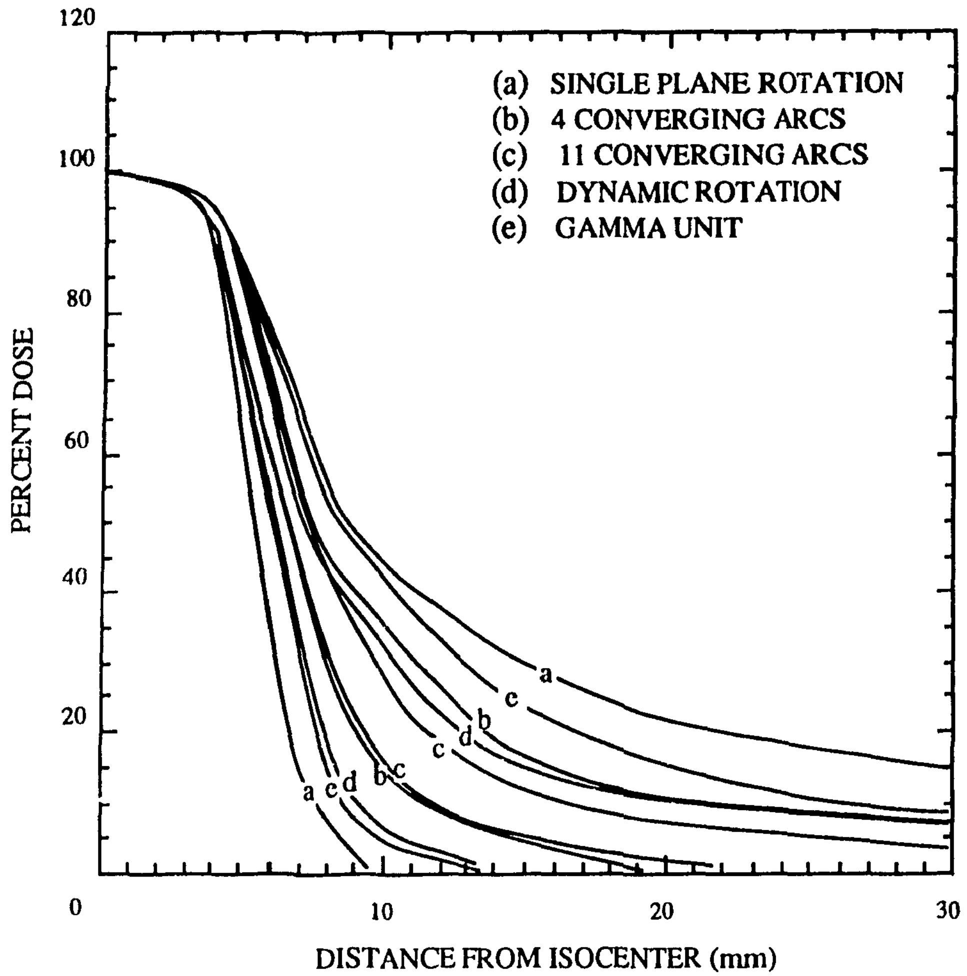

FIGURE 4.3. The steepest and shallowest dose fall-off curves for various linac-based radiosurgical techniques as calculated on a spherical phantom of 8 cm radius with the 1 cm diameter collimator. The percentage doses are normalized to 100% at the isocenter and plotted as a function of distance from the target center. Curves (a) represent the steepest and shallowest fall-off for single plane rotation, curves (b) for 4 converging arcs, curves (c) for 11 converging arcs, curves (d) dynamic rotation and curves (e) for the Gamma unit (7). The curves are plotted on the same axes to facilitate comparison between dose fall-offs obtained with the various techniques.

parallel-opposed beam situation is essentially avoided. Curves (b) and (c) of Fig. 4.3 actually compare quite favorably with curve (e) for the Gamma unit. The multiple converging arcs techniques with isocentric linear accelerators are therefore viable alternatives to radiosurgery with the Gamma unit. A comparison between curves (b) and (c) also shows that the larger the number of arcs the steeper appears to be the shallowest dose fall-off curve, which of course is to be expected. This effect, however, only becomes pronounced at isodose levels below 20%, while in the region between 90% and 20%, there is essentially no difference between the 4 arcs and the 11 arcs technique.

The dose fall-off curves for dynamic rotation are shown in Fig. 4.2 (d) and again as curve (d) of Fig. 4.3. The shallowest dose fall-off for the dynamic rotation is better than that for the Gamma unit and very similar to that for the 4 converging arcs technique. It is, however, shallower than the curve for the 11 converging arcs technique. These differences again appear only in the dose regions below 20%, in which a rapid dose fall-off is no longer that important (6). The steepest dose fall-off for the dynamic rotation is similar to that for the Gamma unit, and they both are considerably better than the steepest dose fall-offs obtained for the two multiple converging arcs techniques.

The conclusions drawn from Figures 4.2 and 4.3 for the linac-based radiosurgical treatment techniques with the 1 cm diameter collimator are shown to hold for larger diameter treatment collimators as seen in Figures 4.4 and 4.5 which give the steepest and shallowest dose fall-off curves calculated for the 2 cm and 3 cm diameter collimators, respectively. In both figures we show the single plane rotation in (a), the 4 converging arcs in (b), 11 converging arcs in (c) and the dynamic rotation in (d). Again, both figures show the large discrepancies between the steepest and shallowest fall-off curves for the single plane rotation technique, while the other three techniques exhibit a rapid dose fall-off and good isotropy for isodoses above 20%.

The data of Figures 4.2, 4.4 and 4.5 is quantified in Table 4.1, where the minimum and maximum distances for the dose to fall from the 90% to 50%, 90% to

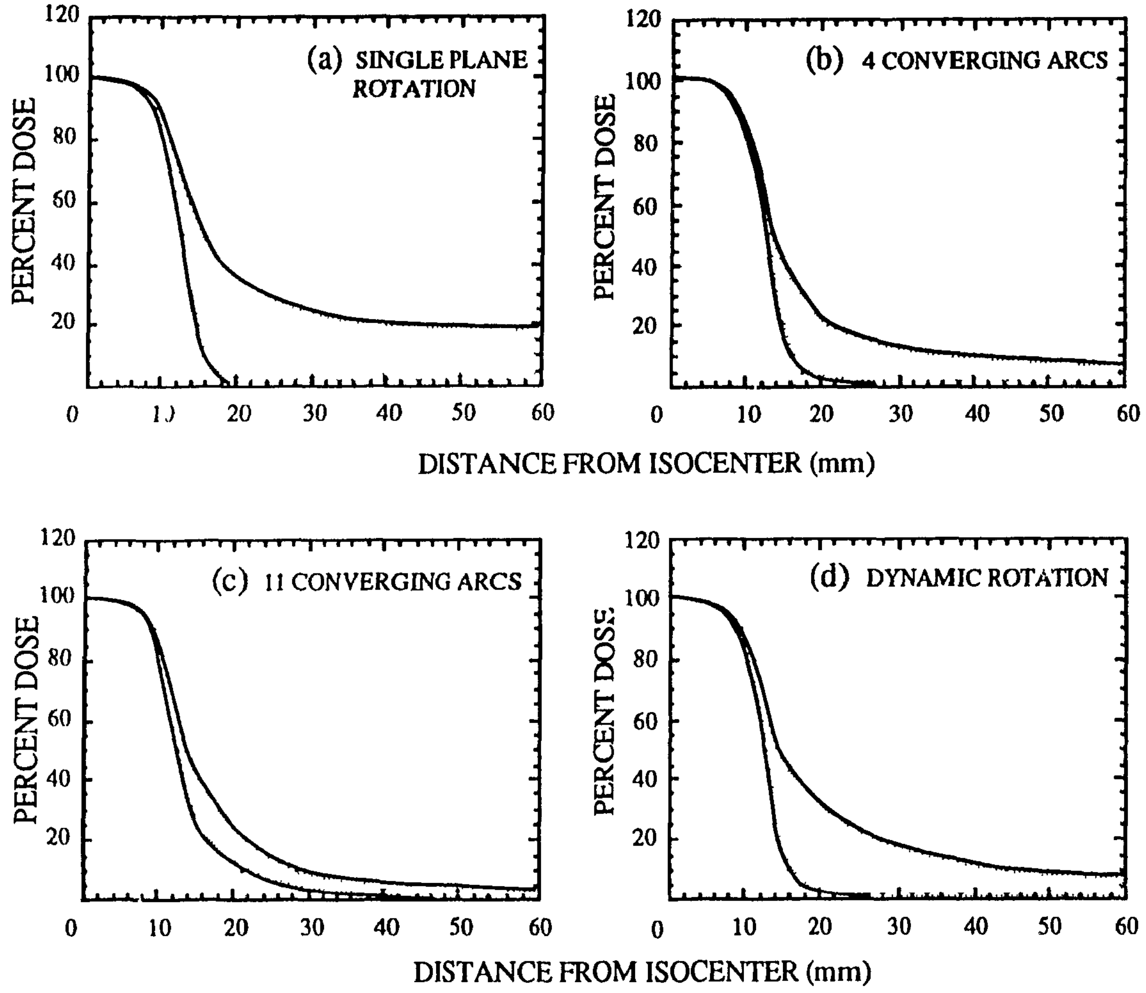

FIGURE 4.4. The steepest and shallowest dose fall-off curves for various linac-based radiosurgical techniques as calculated on a spherical phantom of radius 8 cm with the 2 cm diameter treatment collimator. The percentage doses are normalized to 100% at the isocenter and plotted as a function of distance from the target center. All intermediate dose fall-offs lie in the shaded region between the two extreme curves. Shown are (a) single plane rotation, (b) 4 converging arcs, (c) 11 converging arcs and (d) dynamic rotation.

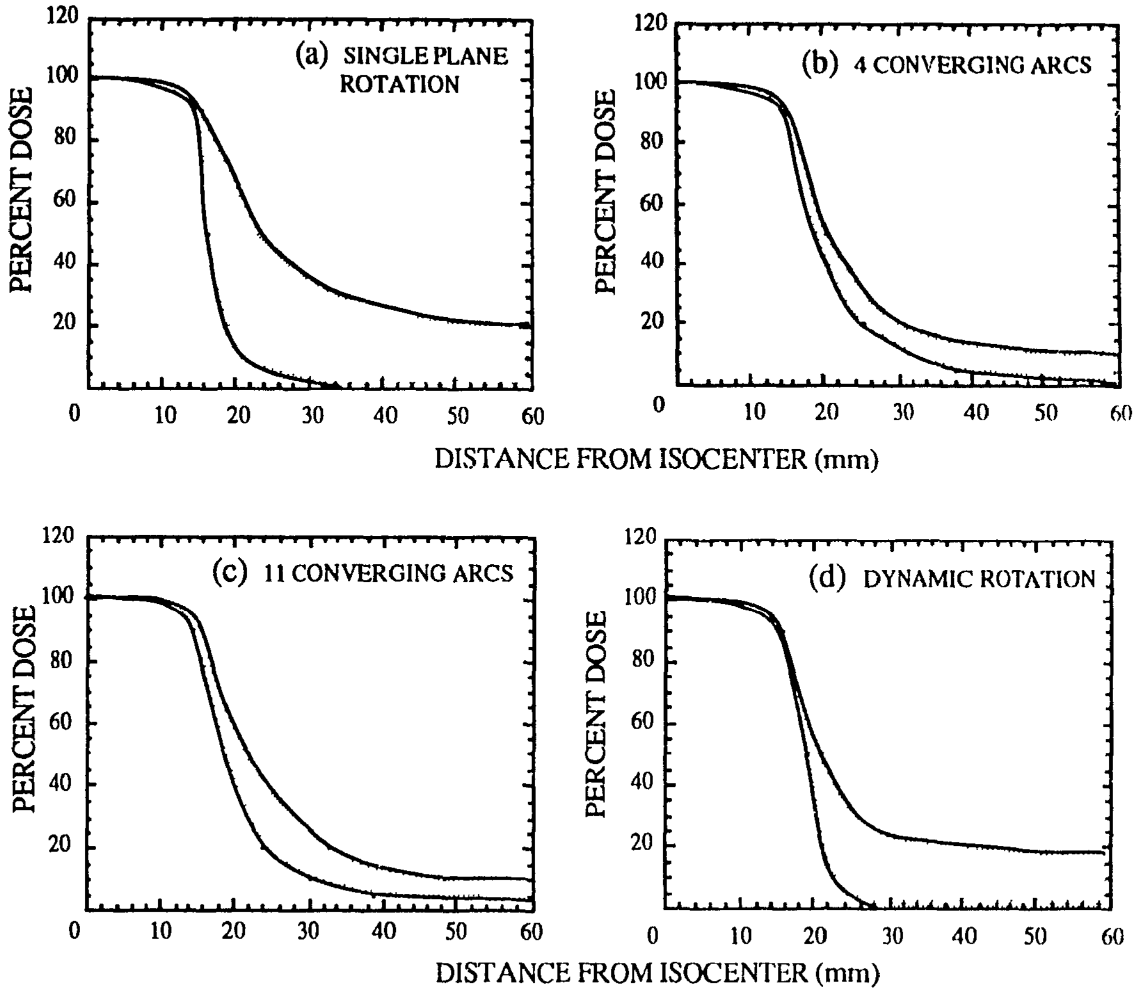

FIGURE 4.5. The steepest and shallowest dose fall-off curves for various linac-based radiosurgical techniques as calculated on a spherical phantom of radius 8 cm with the 3 cm diameter treatment collimator. The percentage doses are normalized to 100% at the isocenter and plotted as a function of distance from the target center. All intermediate dose fall-offs lie in the shaded region between the two extreme curves. Shown are (a) single plane rotation, (b) 4 converging arcs, (c) 11 converging arcs and (d) dynamic rotation.

	Single plane rotation		4 converging arcs		11 converging arcs		Dynamic rotation		
90%-50%	2	4	2	3.5	2	3.5	2	3	
90%-20%	3	17	4.5	8.5	5	7	3.5	9	
90%-10%	3.5	–	7	19.5	8	12.5	5	18	(a) 1 cm diameter collimator
90%-50%	2.5	6	3.5	4.5	3	4.5	3.5	5	
90%-20%	4	32	8	12	7.5	12.5	5.5	17.5	
90%-10%	5.5	–	13	30.5	12	19	8.5	34.5	(b) 2 cm diameter collimator
90%-50%	2	8	4	5.5	4	5.5	3	6	
90%-20%	3.5	43	10	15.5	9.5	17.5	6.5	25	
90%-10%	5.5	–	17.5	42.5	16	35.5	7.5	44	(c) 3 cm diameter collimator

TABLE 4.1. Minimum and maximum dose fall-off distances in mm from 90% isodose surface to 50%, 20% and 10% isodose surfaces as calculated with the treatment planning system for single plane rotation, 4 converging arcs, 11 converging arcs and dynamic rotation. The calculations were done on a spherical phantom of radius 8 cm with (a) the 1 cm diameter collimator, (b) 2 cm diameter collimator and (c) 3 cm diameter collimator. In some cases, for the single plane rotation, maximum dose fall-offs extend beyond the range of the calculated distribution and are therefore not available.

20% and 90% to 10% isodose surfaces are listed. Table 4.1 (a) gives the data for the 1 cm diameter collimator, (b) for the 2 cm diameter collmator and (c) for the 3 cm diameter colimator. Based on these data, as well as on Figures 4.2-4.5, one can conclude that the multiple converging arcs techniques and the dynamic rotation on isocentric linear accelerators give good dose distributions and are thus viable alternatives to the commercially available Gamma unit. At isodose values above 20% there is little difference between these three treatment techniques.

The dose distributions discussed above were all calculated with the McGill radiosurgical treatment planning system. Some of these distributions were also measured to verify again the software algorithm. The measurements of radiosurgical dose distributions were made on the spherical tissue equivalent phantom discussed in Chapter 2, in conjunction with film as a detector. The film was placed between the central slices of the phantom, and phantom and film were positioned at the isocenter of the linac with the film parallel to the desired plane of observation, corresponding to the transverse, sagittal or coronal planes. Using thin acrylic rods as supports, the sphere could be placed to hang over the edge of the treatment couch thereby avoiding interference of the radiation beam with the couch. The sphere was placed into a fixed position with respect to the machine isocenter. The machine collimator was set to the standard 4x4 cm^2 field, and the 1 cm treatment collimator was aligned with respect to the isocenter. A lead attenuator with a thickness of approximately 2 cm was placed just above the collimator in order to attenuate the radiation beam. This yielded optical densities of the radiographic films below saturation values (see Fig. 2.4). Films were then irradiated in three orthogonal planes for the four treatment techniques for which the calculations were discussed above. The films were analysed with our densitometry system discussed in Chapter 2, and minimum and maximum dose fall-offs, from the 90% isodose surface to subsequent lesser isodose surfaces, were measured for all films.

The data from these measurements are shown in Fig. 4.6. For the four treatment techniques, minimum and maximum dose fall-offs from the 90% isodose surface to the 50%, 20% and 10% isodose surfaces are depicted in Fig. 4.6 (a), (b) and (c), respectively. The corresponding calculated values, as given previously, are also plotted on these graphs to allow comparison between calculated and measured data. We will limit our discussion of this data to the comparison, as fall-off and isotropy characteristics were already discussed above.

The dose fall-offs from 90% to 50% and from 90% to 20% show excellent agreement between measured and calculated values. The inherent error is ±1 mm (1) in the calculation, and ~±0.5 mm in the measurement. Figure 4.6 (c) depicts the dose fall-offs from 90% to 10%. Here, there is a slightly greater difference between calculated and measured values, especially for the maximum dose fall-offs. We attribute this discrepancy to the dose profile data used by the treatment planning program to calculate dose distributions. It was seen in Chapter 3 that dose profile measurements for these small fields are a function of detector size, and that film analysed with a densitometry system of high spatial resolution gave the sharpest profile measurements, while larger sized ionization chambers gave a shallower profile. This difference was especially apparent at low percentage doses. The dose profile data used in the calculation of dose by the treatment planning program was in fact measured with an ionization chamber. This may explain the over-estimation of low percentage dose values by the treatment planning program and suggests that the dose profile data used in the treatment planning system should be modified to reflect the more accurate measurement technique available with the digital densitometer.

4.4 Summary

In this chapter we have compared the dose distributions resulting from several linac-based radiosurgical techniques. Both calculated and measured dose fall-offs from the 90% isodose surface to lesser isodose values were obtained. Comparisons were made for minimum and maximum fall-offs, as we wished to compare

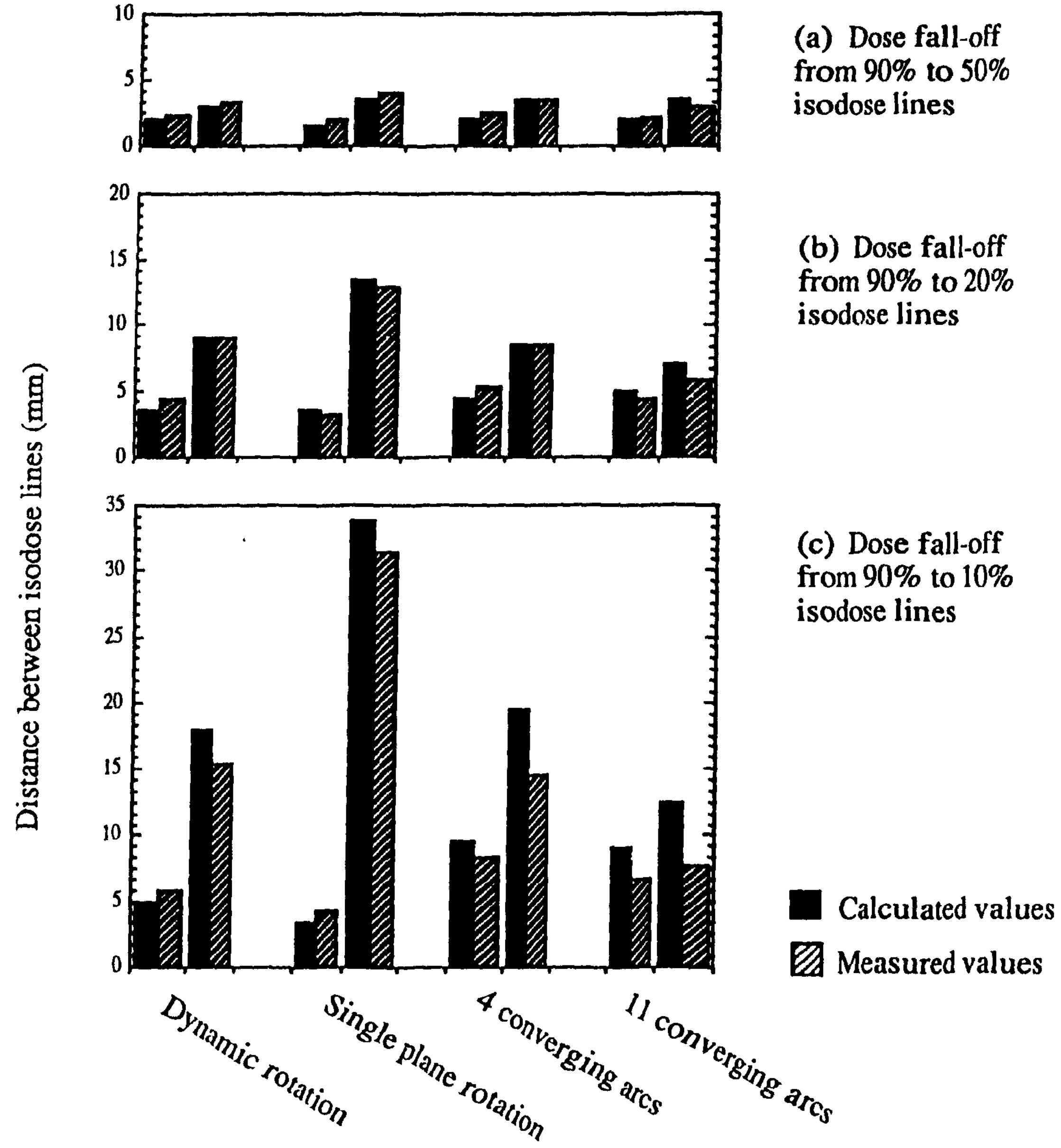

FIGURE 4.6. Minimum and maximum dose fall-off distances in mm for various linac-based radiosurgical treatment techniques. Shown are the distances for the dose to decrease from (a) 90% to 50%, (b) 90% to 50% and (c) 90% to 10%. Measurements were made with 1 cm diameter collimator, a spherical phantom of 8 cm radius and film as a detector. Calculations were performed on a sphere of 8 cm radius with the 1 cm collimator.

radiosurgical techniques. The comparison of radiosurgical techniques showed that methods which avoid parallel-opposed beams result in very similar dose distributions. Comparing dose fall-offs down to the 20% isodose surface, four converging arcs, eleven converging arcs and dynamic rotation are essentially the same. Only at very low isodose surfaces do isotropy differences in techniques begin to manifest themselves. As expected, techniques where the beam entry traces cover the greatest surface area of the skull, such as eleven converging arcs, exhibit the greatest isotropy and the steepest dose fall-offs. Single plane rotation, with its infinite number of parallel-opposed beams in the transverse plane, shows the most anisotropic dose distribution and the shallowest dose fall-off. The dynamic rotation and four converging arcs exhibit similar dose fall-off characteristics, with a progressive anisotropy at lower isodose surfaces.

Comparisons were also made between calculated and measured dose fall-off data. It was found that calculated values exhibit excellent agreement with measured data at isodose levels above 20%. For comparisons down to the 20% isodose surface the measured and calculated fall-off distances agree to within ~1 mm. At lower isodose surfaces, there is a slightly greater discrepancy between the measured and calculated maximum dose fall-off distances. This can be attributed to inaccurate dose profile data measured with too large an ion chamber. It is recommended that these data be updated with digitally analysed film data.

4.5 References

1. G.B. Pike, E.B. Podgorsak, T.M. Peters and C. Pla, **Dose distributions in dynamic stereotactic radiosurgery**, Med. Phys. **14**: 780-789, 1987.
2. G.B. Pike, E. B. Podgorsak, T.M. Peters, C. Pla, A. Olivier and L. Souhami, **Dose distributions in radiosurgey**, Med. Phys. **17**: 296-304, 1990.
3. J. Milan and R.E. Bentley, **The storage and manipulation of radiation dose data in a small digital computer**, Brit. J. Radiol. **47**:115-117, 1974.
4. A. Olivier, T.M. Peters and G. Bertrand, **Stereotaxic systems and apparatus for use with MRI, CT, and DSA**, Appl. Neurophysiol. **48**: 94-96, 1986.
5. T.M. Peters, J.A. Clark, A. Olivier, G. Mawko, E. Marchand, M. Dieumegarde, L.V. Muresan and R. Ethier, **Integrated stereotactic imaging with CT, MRI, DSA**, Radiol. **161**:821-825, 1986.
6. E.B. Podgorsak, G.B. Pike, A. Olivier, M. Pla and L. Souhami, **Radiosurgery with high energy photon beams: a comparison among techniques**, Int. J. Radiat. Oncol. Biol. Phys. **16**: 857-865, 1989.
7. L. Walton, C.K. Bomford, D. Ramsden, **The Sheffield stereotactic radiosurgery unit: phsical characteristics and principles of operation**, Brit. J. Radiol. **60**: 897-906, 1987.

CHAPTER 5

CYLINDRICAL DOSE DISTRIBUTIONS

5.1 Introduction

As discussed in previous chapters, ideally, radiosurgery would be performed with beams approaching the target from directions essentially spread over the 2π geometry of the upper hemisphere of the brain. The limiting plane would be the transverse plane through the center of the target. The 2π geometry would give the sharpest as well as an essentially isotropic dose fall-off outside the target volume. In practice, because of technical constraints, the 2π geometry can only be approximated to a certain degree, resulting in the various radiosurgical techniques presently in clinical use. Because in all techniques the beams approach the target in non-coplanar directions, their shape has to be circular, which results in spherical dose distributions, at least for isodose surfaces above 50%. It was shown in Chapter 4 that the isodose surfaces below 50% become progressively more anisotropic, reflecting the particular properties of a given radiosurgical technique.

The isodose surfaces used clinically are thus spherical, appropriate to spherical target volumes. Target volumes are not generally spherical, they may, however, because of their small dimensions within the brain, be approximated by spheres. This was the practice when radiosurgery was first developed. Since then, it has been observed that many volumes to be treated are ellipsoidal or even more irregular in shape. This includes the most common lesions amenable to radiosurgery, the arteriovenous malformations. Thus, the most recent interest in radiosurgery has been to devise a means of shaping isodose contours to conform to the shape of the actual target volume. Of course, the most important isodose surface that must be shaped is the one which circumscribes the target volume, usually the 90% dose surface.

A variety of methods has been suggested to accomplish this goal but only one has been implimented clinically, using multiple isocenters. In this technique, rather than approximating the irregular target with a relatively large sphere, the target is covered by several small spheres, each with its own isocenter within a certain region of the target. In principle one can expect a reasonable conformity of the irradiated volume with the irregular target volume as the dose distributions obtained from the treatment of each single isocenter with a circular beam are superimposed. For example, an ellipsoid with a length of 3 cm and a width of 1 cm could be irradiated with the 1 cm collimator treating three isocenters along the ellipse's major axis. The main disadvantage of this technique is the complicated dose overlap produced by the multiple isocenters. This results in extensive planning and treatment time, as each process must be repeated for the chosen isocenters. Moreover, imprecise placement of the multiple isocenters can result in severe dose inhomogeneities within the target.

In this chapter we propose a direct means of obtaining cylindrical dose distributions with a single isocenter. Cylindrical targets can be used to approximate ellipsoid targets in situations where approximations with spherical irradiations would result in excessive doses to vital yet uninvolved structures within the brain. The method with cylindrical targets could be implemented with any radiosurgerical technique which involves the rotation of both the gantry and couch. Variable rectangular fields are used and the basic principle is the additional rotation of the treatment collimator to follow a projected field in the plane of the treatment couch. In this chapter we describe the method in detail, including its derivation, as well as present preliminary studies of the method's viability. This methodology has been referred to as dynamic conformational therapy in conventional irradiations.

5.2 Definition of the coordinate systems

The coordinate system used in all calculations is defined in Fig. 5.1. The XYZ system defines the coordinate frame fixed in the treatment room, with the position of the gantry and couch centers of rotation (isocenter) defining the origin of this system. The gantry rotates in the YZ plane about the X axis. The angle of gantry rotation θ is defined to be 180° when the gantry is in a vertical, upright position with the beam pointing down. An increase in gantry angle is obtained through a clockwise rotation.

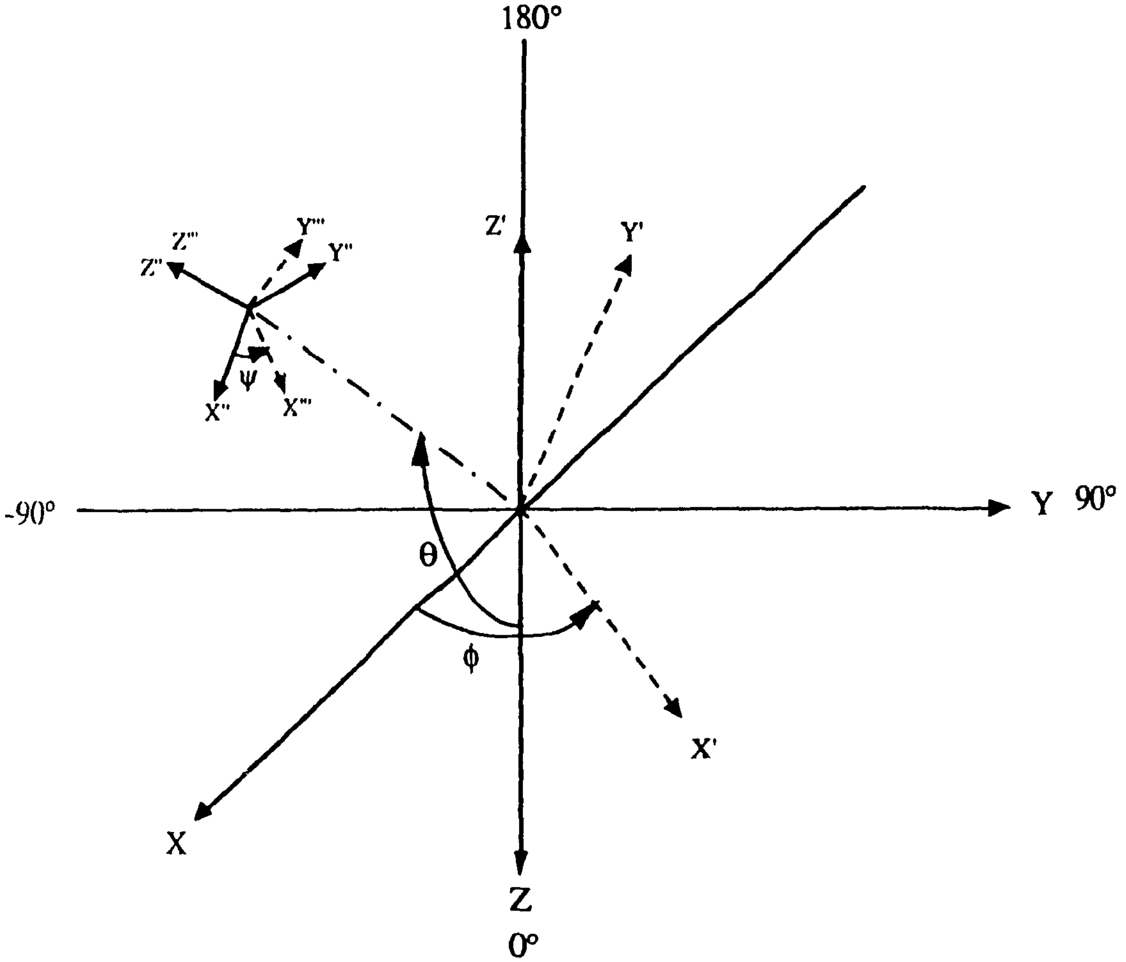

FIGURE 5.1. Degrees of rotational freedom and definition of coordinate systems. The XYZ coordinate frame is fixed in the treatment room with the origin at the isocenter. The X'Y'Z' is the coordinate frame fixed with respect to the couch and rotating with the couch through an angle ϕ in the XY plane about the Z axis. The X"Y"Z" frame is fixed in the ganrty head, rotated through angle θ in the YZ plane about the X axis. Angle ψ gives the collimator rotation in the X"Y" plane about the Z" axis, which is also the beam axis. The triple primed frame X'"Y'"Z'" is the fixed frame rotated about this axis.

If we consider the gantry head to have a fixed frame of reference, with a coordinate system X"Y"Z", this frame is simply a clockwise rotation of XYZ through angle θ about the X axis. A further degree of freedom in the gantry head is introduced by rotation of the collimator itself. This collimator, lying in the X"Y" plane, can rotate clockwise or counter-clockwise by an angle defined as ψ. A coordinate system, X'''Y'''Z''', stationary in the collimator plane is defined as a counter-clockwise rotation of the double primed frame through ψ degrees.

The couch rotates by an angle ϕ in the XY plane about the Z axis. The angle ϕ=0° corresponds to the couch positioned along the X axis, with a positive increase in angle given by a counter-clockwise rotation. For example, the couch positioned along the positive Y axis represents a couch angle of 90°. A prime frame is defined to remain fixed with respect to the couch, X'Y'Z'. The Z' axis coincides with the Z axis except that the directions are opposed. Note that the primed frame is simply a counter-clockwise rotation of the unprimed frame through an angle ϕ.

We thus have four coordinate systems which are all related to each other through a suitable transformation. The transformation parameters, the angles defining the rotations, are analogous to the Euler angles in classical mechanics (1). However, we chose our definition of angles to conform with angles already defined for the dynamic rotation on our linac. This avoids confusion when implementing calculations on the treatment machine.

The basis of the method to be described lies in the degrees of freedom discussed above. In the dynamic rotation radiosurgery, the couch and gantry rotate simultaneously. As described in detail in Chapter 1, the couch moves from ϕ=75° to ϕ=-75°, while the gantry concurrently rotates from θ=30° to θ=330°. Thus, there is a simple two to one correlation between θ and ϕ, with the gantry moving by two degrees for every couch degree. If we now consider the collimator rotation, it is conceivable that the collimator rotates so as to continuously follow the couch motion. A standard linac collimator defines a two dimensional field with longitudinal and lateral collimator openings. Thus the longitudinal opening of the collimator can be aligned with the longitudinal axis of a cylidrical or ellipsoidal target. The size of this opening will depend on the relative target, couch and gantry positions. Note that the lateral opening of the collimator can simply be fixed to correspond to the width of the target once the longitudinal axes have been aligned. A cylindrical volume will then be irradiated during the rotation of the gantry about the couch. The task is to find the collimator rotation and the longitudinal field size in relation to the gantry and couch motions of dynamic rotation, that results in a rectangular superposition of fields at a pre-determined target. To do this, we find the transformations that take an arbitrary vector in the couch coordinate frame, given by X'Y'Z', to the corresponding coordinates in the fixed collimator frame, X'''Y'''Z'''. The vector X'Y'Z' then represents the longitudinal axis of the target. The X''' coordinate corresponds to the longitudinal collimator setting necessary to treat a target of this length. The angle through which the collimator must rotate such that this longitudinal opening aligns itself with the target, as given by the angle ψ, must also be calculated.

5.3 Derivation of transformation matrices

In this section we derive the transformations taking a vector in the couch coordinate frame X'Y'Z' to the collimator coordinate frame X'''Y'''Z'''. Referring to Fig. 5.1 for definitions of all angles and axes, we consider the appropriate transformations. The equation

$$\vec{\mathbf{a}} = \mathbf{A}\,\vec{\mathbf{a}}' \,, \tag{5.1}$$

where the matrix **A** is given as

$$\mathbf{A} = \begin{pmatrix} \cos\phi & -\sin\phi & 0 \\ \sin\phi & \cos\phi & 0 \\ 0 & 0 & 1 \end{pmatrix}, \tag{5.2}$$

relates a vector in the primed coordinate system to its coordinates in the fixed frame of reference, the unprimed frame. This transformation corresponds to a counter-clockwise rotation of the XY plane through angle ϕ about the Z axis.

A clockwise rotation in the YZ plane about the X axis through angle θ, such as a rotation of the gantry, is characterized by a transformation matrix **B** given by

$$\mathbf{B} = \begin{pmatrix} 1 & 0 & 0 \\ 0 & \cos\theta & \sin\theta \\ 0 & -\sin\theta & \cos\theta \end{pmatrix} . \tag{5.3}$$

A vector undergoing this transformation from the double primed frame to the unprimed frame is given as follows:

$$\vec{\mathbf{a}} = \mathbf{B}\,\vec{\mathbf{a}}'' . \tag{5.4}$$

Finally, the rotation of the gantry head is characterized through a counter-clockwise rotation of the X'''Y''' plane about the Z'' axis. This transformation is given by,

$$\vec{\mathbf{a}} = \mathbf{C}\,\vec{\mathbf{a}}''' , \tag{5.5}$$

with the matrix **C** defined as follws:

$$\mathbf{C} = \begin{pmatrix} \cos\psi & -\sin\psi & 0 \\ \sin\psi & \cos\psi & 0 \\ 0 & 0 & 1 \end{pmatrix} . \tag{5.6}$$

We combine these transformations to obtain the coordinates of the triple primed frame, which is the fixed frame of the collimator, in terms of the coordinates of a vector in the frame stationary with the couch. Simple manipulations give us the following relationship:

$$\vec{a}''' = C^{-1}\, B^{-1} A\, \vec{a}' \;, \tag{5.7}$$

or

$$\vec{a}''' = \begin{pmatrix} \cos\psi\cos\phi+\sin\psi\cos\theta\sin\phi & -\cos\psi\sin\phi+\sin\psi\cos\theta\cos\phi & -\sin\psi\sin\theta \\ -\sin\psi\cos\phi+\cos\psi\cos\theta\sin\phi & \sin\psi\sin\phi+\cos\psi\cos\theta\cos\phi & -\cos\psi\sin\theta \\ \sin\theta\cos\phi & \sin\theta\cos\phi & \cos\theta \end{pmatrix} \vec{a}' . \tag{5.8}$$

Thus, the longitudinal opening of the collimator, as a function of the couch position, gantry position and longitudinal target axis, is given by,

$$\begin{aligned} x''' &= (\cos\psi\cos\phi + \sin\psi\cos\theta\sin\phi)\, x' \\ &\quad + (-\cos\psi\sin\phi + \sin\psi\cos\theta\cos\phi)\, y' - \sin\theta\sin\psi\, z' \;. \end{aligned} \tag{5.9}$$

To find the angle of collimator rotation ψ, which aligns the field with the target, we examine the longitudinal target vector in the coordinate system of the gantry head, the double primed frame as given by **a"**. ψ corresponds to the angle that the projection of vector a" makes in the X"Y" plane. We refer to the schematic diagram below, where we convert to spherical coordinates,

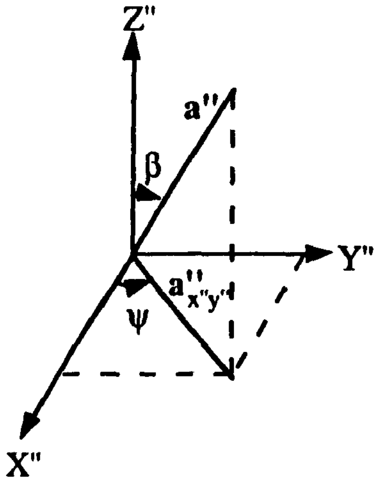

where

$$x'' = a'' \sin\beta \cos\psi \ , \tag{5.10}$$

$$y'' = a'' \sin\beta \sin\psi \ , \tag{5.11}$$

and

$$z'' = a'' \cos\beta \ . \tag{5.12}$$

The angle that the projected vector **a"** makes with the X" axis is given by

$$\tan\psi = \frac{y''}{x''} \ . \tag{5.13}$$

From the transformations in Equations (5.1) through (5.6), we can easily express x" and y" in terms of the target coordinates. We note that

$$\vec{\mathbf{a}}'' = \mathbf{B}^{-1}\, \mathbf{A}\, \vec{\mathbf{a}}' \ , \tag{3.14}$$

or

$$\vec{\mathbf{a}}'' = \begin{pmatrix} \cos\phi & -\sin\phi & 0 \\ \cos\theta \sin\phi & \cos\theta \cos\phi & -\sin\theta \\ \sin\theta \sin\phi & \sin\theta \cos\phi & \cos\theta \end{pmatrix} \vec{\mathbf{a}}' \ . \tag{5.15}$$

Thus,

$$x'' = x' \cos\phi - y' \sin\phi \ , \tag{5.16}$$

$$y'' = (x' \sin\phi + y' \cos\phi) \cos\theta - z' \sin\theta \ , \tag{5.17}$$

and so

$$\tan\psi = \frac{y''}{x''} = \frac{(x'\sin\phi + y'\cos\phi)\cos\theta - z'\sin\theta}{x'\cos\phi - y'\sin\phi} \ . \qquad (5.18)$$

For a given couch and gantry setting, we can calculate the collimator longitudinal opening and rotation with Equations (5.9) and (5.18), respectively. Given a vector **a'** in the couch coordinate system, which describes the longitudinal orientation of a cylindrical target for a fixed couch and gantry setting, the longitudinal collimator opening and the necessary collimator rotation can be calculated such that the length of this opening is aligned with the target.

With the collimator length adjusted to the longitudinal axis of the target volume, the short opening of the collimator must simply be fixed to one length which corresponds to the diameter of the target. A cylindrical target will then be irradiated during the gantry rotation. The short collimator opening must be set to the projection of the target's diameter in the X'Y' couch plane. If we consider the width of the target in the couch frame w', and the following coordinate system,

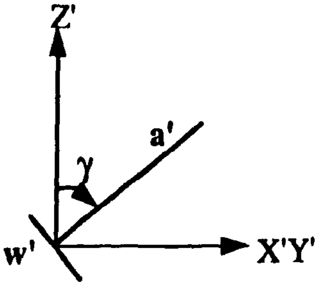

then

$$w'_{X'Y'} = w'\cos\gamma \ , \qquad (5.19)$$

where

$$\gamma = \frac{z'}{\sqrt{x'^2 + y'^2 + z'^2}} \ . \qquad (5.20)$$

The short collimator opening must thus be fixed at

$$w'' = w' \frac{z'}{\sqrt{x'^2 + y'^2 + z'^2}} , \qquad (5.21)$$

resulting in a cylindrical dose distribution of diameter w' obtained as the gantry rotates about the X axis.

Thus, as the couch and gantry follow their paths in dynamic rotation, with a 1:2 relationship between the two angles of rotation, the collimator longitudinal opening and rotation will also follow a route determined by the equations derived above. The lateral axis of the collimator, on the other hand, will remain fixed, depending on the diameter and orientation of the target within the couch coordinate system.

5.4 Preliminary studies of the cylindrically shaped targets

Preliminary studies were undertaken to determine the viability of the above method. Several longitudinal target orientations were chosen and the respective gantry, couch, and collimator openings, both lateral and longitudinal, as well as the collimator rotation were calculated. Prior to irradiation, film was placed between the central slices of the spherical phantom described in Chapter 2 and the plane of the film was oriented to the desired plane of observation. Unfortunately, the relationships governing the collimator rotation and collimator opening are quite complex, making continuous rotation of couch, gantry and collimator, in addition to a continuous adjustment of the collimator longitudinal opening difficult to implement. To circumvent these difficulties, it was decided to deliver the dose not in a continuous irradiation, but with several single beams at specified intervals. The route of the gantry from 30° to 330° was divided into 11 segments of equal arc. At each of these 11 gantry positions, corresponding couch, collimator rotation and collimator opening were determined from the equations derived above in order to simulate the dynamic rotation in conjunction with the collimator rotation and field size adjustment. Thus the paths of all continuous motions were divided into equal segments, with equal doses given as 1/11 of the total prescribed dose, delivered at each segment.

The first step of the study was to verify the accuracy of the machine collimator in terms of its rotation and size setting. As with any radiosurgical technique, all entry beams must superimpose at the target volume which is at the isocenter, during the rotation of the gantry. A cylinder oriented along the X' axis of the couch, with a length of 3 cm and a width of 1 cm was chosen as a target volume. The collimator was fixed to longitudinal and lateral openings corresponding to the longitudinal target axis and target diameter, respectively. With the couch and collimator in stationary positions, the gantry was rotated through 360° and delivered dose to the cylindrical target. The results of these irradiations are shown in Fig. 5.2. Observations were made in the transverse (Y'Z'), sagittal (X'Z') and coronal (X'Y') planes, as shown in Figures 5.2 (a), (b) and (c), respectively. The entrance and exit beams of the 11 individual irradiations which were used to achieve the dose distribution, are visible where the beams intersect the plane of the film. The transverse plane shows the lateral cross-section through the resulting cylindrical dose distribution with a width of ~1 cm, while the other two planes show longitudinal cross-sections each with a length of 3 cm. The dose from all 11 beams appears to superimpose at the target volume, showing the spatial accuracy of the machine collimator rotation about the isocenter. As the isocentricity of the machine collimator has been verified for this simple case, we can now implement the transformations to more complex radiosurgical techniques.

As a simplest conceivable target orientation, a cylindrical target volume lying in the couch plane along the couch X' axis, with its center at the machine isocenter was selected for irradiation. The length was chosen to be 3 cm and its diameter 1 cm. This is a similar target to the one chosen in the machine collimator isocentricity test of Fig. 5.2. The eleven collimator openings and rotations, which would ensure that the dose superimposed at the target volume for the given couch and gantry settings, were

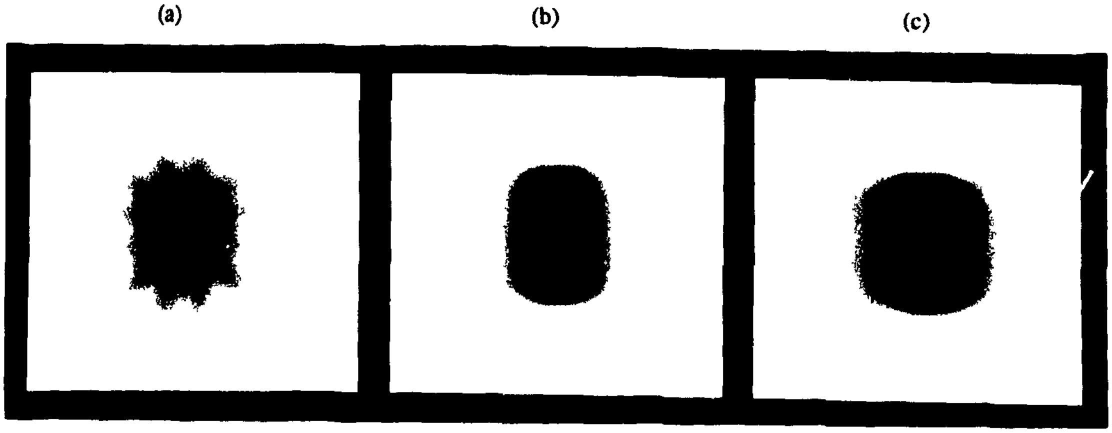

TRANSVERSE PLANE
(Y' Z')

SAGITTAL PLANE
(X' Z')

CORONAL PLANE
(X' Y')

FIGURE 5.2. Results of a test to determine the spatial accuracy of the machine collimator rotation about the isocenter. The machine collimator was set to give a longitudinal opening of 3 cm and a lateral opening of 1 cm at the isocenter. The couch remained stationary, while the gantry rotated through 360°. The dose was delivered in 11 equal intervals along the gantry's path. Part (a): dose distribution of a lateral cross-section of the cylinder as measured in the transverse (Y'Z') plane. Parts (b) and (c) show longitudinal cross-sectional views as measured in the sagittal (X'Z') and coronal (X'Z') planes, respectively. Measurements were made on a spherical phantom of radius 8 cm, using film as a detector.

calculated from Eq. (5.9) for the collimator opening and Eq. (5.18) for the collimator angle. The width of this target, lying in the X'Y' plane was 1 cm, thus the lateral collimator opening was set to this field size. The set of 11 irradiations was repeated for three planes of observation, with films placed in the transverse (Y'Z'), sagittal (X'Z') and coronal (X'Y') planes.

Figure 5.3 shows the results of these three irradiations. The measured dose distribution is shown in Fig. 5.3 (a) in the transverse plane, in Fig. 5.3 (b) in the sagittal plane and in Fig. 5.3 (c) in the coronal plane. These films clearly show the cylindrical dose distribution obtained with this technique. The transverse plane shows a lateral cross-sectional view of the target volume, with a circular dose distribution at the center of the film where all incoming beams superimpose. The other two films, through sagittal and coronal planes, are longitudinal cross-sections, and we see the dark rectangle at the center of the films representing the target dose distribution. These three films show clearly that the target is cylindrical in shape, with a width of ~1 cm and a length of ~3 cm. Entrance and exit beams on the films are only visible if they intersect the plane in question. Thus in the transverse plane, we see several entrance and exit beams, while in the sagittal and coronal planes we see only two. We can assume that the dose fall-off outside the target volume will be similar to that encountered in spherical dynamic rotation radiosurgery, as we follow the same gantry and couch paths and avoid all parallel-opposed beams.

To verify that the derived method will in fact irradiate an arbitrarily oriented cylindrical target volume, the collimator openings and rotations were calculated for a target whose longitudinal axis was oriented along a vector pointing from the origin to (0.75,0.75,1.1) in the couch frame. This correponds to a cylinder of length 3 cm, tilted at 45° to the X'Y' plane and at 45° to the X'Z' plane with the center of the cylinder at the machine isocenter. The width of the cylinder was chosen to be 1 cm. The results of these irradiations are shown in Fig. 5.4 and Fig. 5.5. In Fig. 5.4 we verify that the irradiated volume has the intended dimensions. These films were taken through the cross-sectional planes of the cylindrical target itself. Figure 5.4 (a) is the

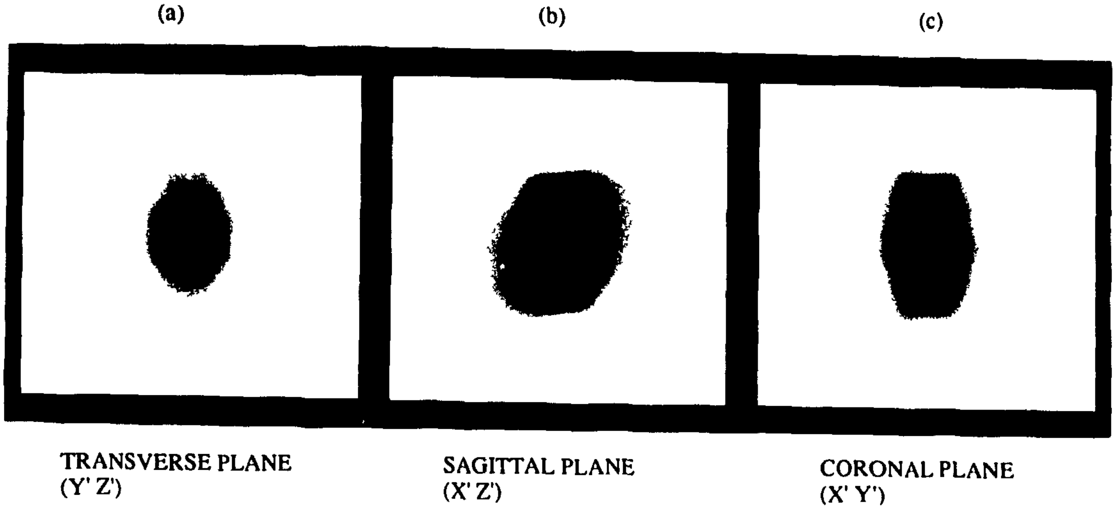

FIGURE 5.3. Dose distributions obtained by irradiating a cylindrical target volume lying in the couch plane along the couch X' axis, with its center at the machine isocenter. The target of diameter 1 cm and length 3 cm was irradiated with the cylindrical dynamic rotation technique utilizing the gantry, couch and collimator rotation, as well as adjustable collimator longitudinal opening. The dose was delivered in 11 equal fractions along the gantry's path of rotation. Part (a): dose distribution of a lateral cross-section of the cylinder as measured in transverse (Y'Z') plane. Parts (b) and (c): longitudinal cross-sectional views as measured in the sagittal (X'Z') and coronal (X'Y') planes, respectively. Measurements were made on a spherical phantom of radius 8 cm with film as a detector.

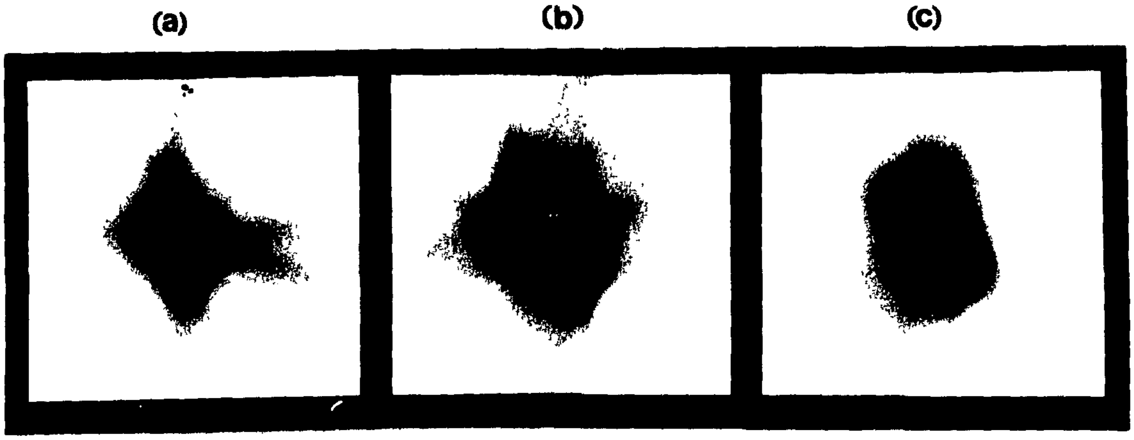

TRANSVERSE PLANE
TILTED 45°
(Y' COS45° Z')

SAGITTAL PLANE
TILTED 45°
(X' COS45° Z')

CORONAL PLANE
TILTED 45°
(X' COS45° Y')

FIGURE 5.4. Dose distributions obtained by irradiating a tilted cylindrical target with a longitudinal axis oriented along a vector pointing from the origin to (0.75,0.75,1.1) in couch frame of reference with the origin corresponding to the target center. The target of diameter 1 cm and length 3 cm was irradiated with the cylindrical dynamic rotation technique utilizing the gantry, couch and collimator rotation, as well as adjustable collimator longitudinal opening. The dose was delivered in 11 equal intervals along the gantry's path of rotation. Part (a): dose distribution of a lateral cross-section of the cylinder as measured in a plane tilted 45° with respect to the transverse plane (Y'cos45° Z') . Parts (b) and (c) show longitudinal cross-sectional views as measured in planes tilted by 45° from the sagittal plane (X'cos45° Z') and coronal plane (X'cos45° Y'), respectively. Measurements were made on a spherical phantom of radius 8 cm, using film as a detector.

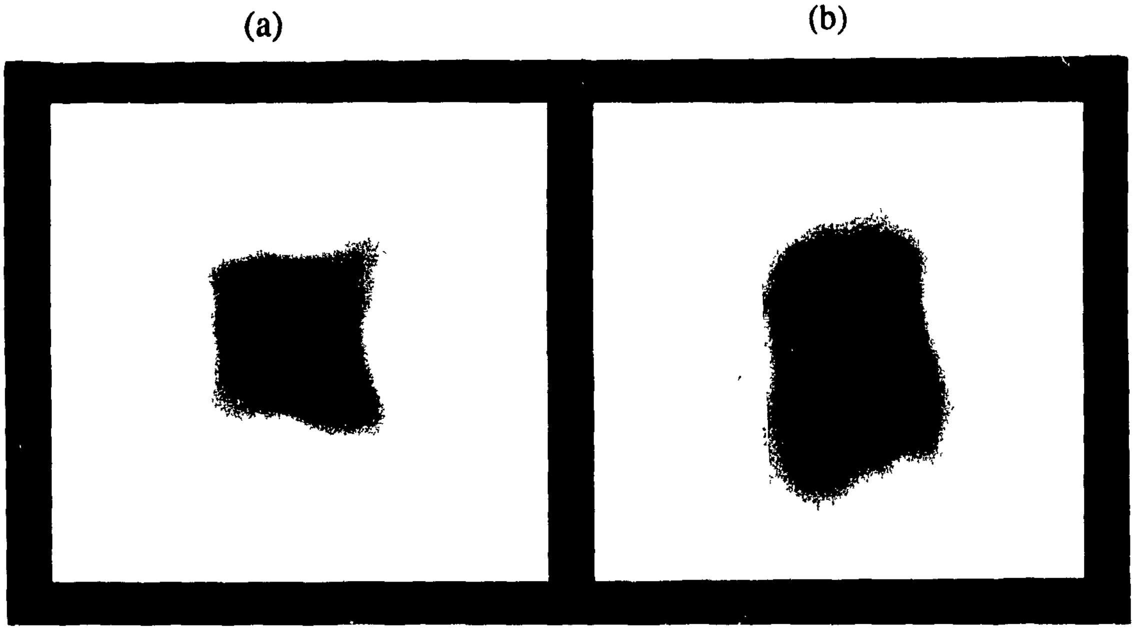

TRANSVERSE PLANE
(Y' Z')

CORONAL PLANE
(X' Y')

FIGURE 5.5. Dose distribution obtained by irradiating a tilted cylindrical target with a longitudinal axis oriented along a vector pointing from the origin to (0.75,0.75,1.1) in the couch frame of reference with the origin corresponding to the target center. The target of diameter 1 cm and length 3 cm was irradiated with the cylindrical dynamic rotation technique utilizing the gantry, couch and collimator rotation, as well as adjustable collimator longitudinal opening. The dose was delivered in 11 equal intervals along the gantry's path of rotation. Part (a): dose distribution as measured in the transverse plane of the couch (Y'Z'). Part (b) :dose distribution as measured in the coronal plane of the couch (X'Y'). Measurements were made on a spherical phantom of radius 8 cm using film as a detector.

lateral cross-sectional view, taken with the observation film oriented along the transverse plane tilted by 45°, (b) and (c) show the longitudinal cross-sections observed from the sagittal plane tilted by 45° and the coronal plane tilted by 45°, respectively. We see the cylindrical dose distribution in these films. Figure 5.5 shows the same irradiations, but the planes of observation correspond to the Y'Z' and X'Y' planes in (a) and (b), respectively. These films show a slice taken through the cylinder. All films verify that the method derived does in fact result in cylidrical dose distributions and that these distributions can be oriented in any arbitrary direction with the center of the cylinder placed into the isocenter of the linac.

5.5 Summary

Recent interest in radiosurgery has focussed on obtaining dose distributions of arbitrary shapes with arbitrary orientations within the brain. The first step will be from spherical to cylindrical isodose distributions. In this chapter we have derived a method, whereby the radiosurgical dynamic rotation can be adapted to include collimator rotation such that a cylindrical target volume is treated directly during irradiation. The method consists of rotating the collimator and adjusting its longitudinal opening during the paths followed by the couch and gantry, such that the collimator field is always aligned with the longitudinal target axis and has the projected length of this axis. Transformation matrices relating vectors in the coordinate system of the couch to that of the collimator enabled us to develop equations that allow the calculation of collimator opening and rotation as a function of gantry angle θ, couch angular position ϕ and the orientation of the target longitudinal axis in the couch coordinate frame given by (x',y',z').

Theoretically, continuous collimator motion is possible along with the simultaneous couch and gantry rotation but because the equations are somewhat complex this is difficult to implement in practice. In our preliminary studies, we overcame this difficulty by dividing the path of the gantry into 11 equal segments and delivering 1/11 of the total dose at each of these intervals. Preliminary studies showed that the method is viable indeed. Cylindrical dose distributions were achieved with several arbitrary longitudinal axis orientations. Furthermore, the clinically desired dose fall-off characteristics, resulting from spherical dynamic rotation radiosurgery, are maintained. This is because cylindrical dynamic rotation, in a similar manner to conventional dynamic rotation, avoids all parallel-opposed beams and spreads the entrance dose over a large surface area.

5.6 Reference

1. H. Goldstein, **Classical Mechanics**, 2nd edition, Addison-Wesley Publishing Company, Inc., Reading, Massachusettes, 1980, pp.132-148.

CHAPTER 6

CONCLUSIONS

6.1 Summary

Since the birth of radiosurgery in the 1950's, the subject has generated much clinical and experimental interest. With the recent advances in brain imaging and mapping this interest has increased greatly, and the role of radiosurgery has expanded to the treatment of a wide variety of brain diseases. Historically, the Gamma unit offered the first commercially viable means of performing radiosurgery. However, in recent years linear accelerator-based radiosurgery has been developed in several centers, and these techniques have become widespread in use. Radiosurgery with heavy charged particle beams, though developed before the Gamma unit, will never be a serious competitor to x-ray techniques because of the enormous costs of purchasing, operating and maintaining a cyclotron. In this thesis, we have focussed on radiosurgical techniques using linear accelerators, as this is the machine available for radiosurgery in our center. The specific linac-based radiosurgery techniques discussed in some detail were the single plane rotation, the multiple non-coplanar converging arcs (both 4 and 11 arcs) and the dynamic rotation radiosurgery.

We have covered a variety of aspects concerning radiosurgery in general, and more specifically, linac-based radiosurgery in particular. We have discussed the techniques themselves, the beams used to irradiate the targets and our ability to adequately measure the parameters of these beams, the dose distributions resulting from different radiosurgical techniques, and a means of modifying currently available techniques to allow for a more versatile dose distribution shaping.

The requirements put on linear accelerators used in radiosurgery are quite stringent, because of the high doses delivered and small volumes treated. Especially important is the spacial accuracy of dose delivery. This accuracy is essentially dependent on the isocentricity of both the gantry and the couch, and on the proper placement of additional circular field defining collimators about the machine's isocenter. Simple tests show that the spatial accuracy of linac-based radiosurgical techniques can be well within ±1 mm, the present limit of target localization techniques, providing that the linac is in a good mechanical condition and that radiosurgery is given with extreme care. Performing these tests prior to patient treatment will ensure proper placement of treatment field collimators and verify the isocenter accuracy of the linac.

Because of the small dimensions of radiosurgical beams, a suitable detector must be chosen to measure beam parameters. We found that small sized ionization chambers and semiconductor diodes were quite adequate for measurements not involving sharp dose gradients, such as percentage depth dose curves. In dose profile measurements, we found that these small detectors generally did not have the spatial resolution needed to precisely measure large changes in dose over short distances. Thus, a digital imaging system used in film analysis was developed for dosimetric purposes. The digital film densitometry system exhibited excellent spatial resolution, (~0.2 mm), making this detector very suitable for small scale measurements.

When measuring percent depth doses for the radiosurgical fields, it was observed that the depth of dose maximum changed with field size, becoming smaller with decreasing field diameter. This is contrary to what would be expected for larger conventional radiotherapy field sizes. By measuring the various scatter components of the beams, it was shown that the shift in the depth of dose maximum is not a result of collimator scatter, either photon or electron, but in fact is caused by electron scatter originating in the phantom. The effect was empirically explained using the probabilities of electron scatter as determined by Compton theory in terms of the electron recoil angle and the corresponding electron kinetic energy or range.

Dose distributions resulting from several linac-based radiosurgical techniques, single plane rotation, 4 converging arcs, 11 converging arcs and dynamic rotation, were calculated and compared. It was found that methods avoiding parallel-opposed beams result in very similar dose distributions at relatively large isodose values, at low isodose values, however, the differences in techniques begin to manifest themselves, in terms of more anisotropic and technique-specific dose distibutions. Comparing dose fall-offs down to the 20% isodose surface, 4 converging arcs, 11 converging arcs and the dynamic rotation have essentially the same dose distributions. Measured dose distributions of the same treatment techniques verified the conclusions drawn from the calculated distributions. Only at low isodose surfaces was a slightly greater discrepancy between measured and calculated dose fall-off distances observed. This was attributed to an over estimation of dose profile data, measured with an ionization chamber and used in the treatment planning system.

Recent interest in radiosurgery has focussed on obtaining cylindrical dose distributions. We derived a method whereby the rotation of a rectangular collimator and adjustment of its longitudinal opening during the paths followed by the couch and gantry results in a superposition of rectangular fields at the target volume. A cylindrical dose distribution is then obtained during rotation of the gantry. The equations governing collimator rotation and longitudinal opening are functions of the gantry angle, couch angle and target longitudinal axis coordinates in a frame of reference which is stationary with the couch. For a given target orientation and size, and for each couch and gantry position, the necessary collimator rotation and longitudial field size are calculated. The lateral collimator field size is set to the projection of the diameter of the target cylinder in the couch plane. Though subsequent work is still needed before implementing the method clinically, we have shown with preliminary studies that the proposed method is in fact viable.

6.2 Future work

Clinical radiosurgery has been in practice for many years now, including several years experience with linac-based radiosurgery. As a result, many of the technical aspects of radiosurgery, as well as the dose distributions resulting from specific radiosurgical techniques, are well known. However, even though the measurement of radiosurgical beam parameters may be relatively simple once proper detectors and measuring techniques are chosen, some of the implications of these measurements are not that easily understood. It is clear from the measurements discussed in Chapter 3, that narrow photon beams exhibit properties not observed in conventional radiotherapy beams. The radiosurgical beams have diameters of the same order of magnitude as the range of the electrons generated in tissue by the incoming photon beam. The implications of this have been observed with the shift in the depth of dose maximum. By means of the Compton equations governing scatter of recoil electrons, we can understand conceptually the events causing the observed effect. However, work has yet to be done to determine the actual paths of the various scattered electrons and photons and to determine exactly where they deposite their dose. Understanding this is the key to understanding these narrow radiation beams.

To accomplish this, a Monte Carlo simulation of the beam is needed. This would allow each interaction of the incoming photon with electrons and subsequently of the recoil electrons with other electrons and nuclei in the material to be monitored and thus understood. Future work on narrow radiation beams therefore involves a Monte Carlo calculation to follow the histories of the photons which comprise the beam. Effects of dose deposition which can be difficult to observe and are not well understood will then, hopefully, be clarified.

Another major aspect of future work, which has been introduced by this thesis, is the work still needed before the method for cylindrical dynamic rotation radiosurgery can be implemented clinically. Although our preliminary studies prove that the method does in fact result in cylindrical dose distributions, many further tests and measurements are necessary to progress to clinical application. These include both technical and dosimetric aspects. As well, studies should be undertaken to assess the possibility of treating targets of an even more general shape.

Technical considerations address mainly the field defining collimator. The machine collimator is used in these irradiations, and the criteria applying to the additional circular collimators used in conventional radiosurgery must also hold here. The accuracy of the field dimensions, in terms of labeled vs. actual field size, must be measured. Naturally, the degree of precision of field dimensions in radiosurgery needs to be much higher than in radiotherapy, and field sizes indicated on the machine must correspond exactly to the actual sizes at the isocenter. The sharpness of the defined field must also be determined. The additional collimators of spherical radiosurgery ensure that the beam penumbra is kept to a minimum, and thus make sharp dose fall-offs easier to achieve. A large penumbra will cause unnecessarily shallow dose fall-offs outside the target volume. If the machine collimator does not meet the criteria of accurately defined fields and a minimal penumbra, then additional rectangular collimators may have to be considered. These additional collimators would be analogous to the additional collimators of spherical radiosurgery, but would need the added feature of adjustable width and length settings to make them suitable for the cylindrical dynamic rotation technique.

The dosimetric aspects of future work are numerous, as essentially no dose measurements with non-spherical beams have yet been made. Dose distribution measurements resulting from treatment simulation with various target orientations must be made. This would allow measurement of the dimensions of the target defining isodose surface as compared to the collimator opening, i.e., it would establish at which isodose curve the field size is defined. Physically, the collimator openings must be set such that the 90% isodose surface encompasses the target volume. Because of a strong beam divergence or unprecise collimator settings, this may not be the case initially.

Beam parameters must be measured for each beam used in a single treatment. These parameters consist of dose profiles in several directions, percentage depth dose curves and relative dose factors. Furthermore, a means of determining the treatment time needed of each individual beam, to deliver a given dose to the target volume, must be found. These times will differ for each beam because of the differences in field sizes and consequently in the relative dose factors. Finally, the possibility of implementing this technique in a treatment planning system, which would calculate the appropriate tissue-maximum ratios, isodose distributions and treatment times should be investigated.

LIST OF FIGURES

FIGURE 1.1. The OBT stereotactic frame attached to the patient's head and patient positioned onto a linac treatment couch in preparation for radiosurgery. The frame, the head and therefore the target volume are immobilized by means of a bracket fixed to the couch which holds the frame in place. Clearly seen is the frame's cubic structure and the orthogonal coordinate system associated with it. Target localization plates, enabling transfer of diagnostic information to the patient, are shown in place.

FIGURE 1.2. Points of beam entry into the patient's skull for various radiosurgical techniques: (a) Gamma unit, (b) single plane rotation with a linear accelerator, (c) multiple non-coplanar arcs with a linear acelerator and (d) dynamic rotation with a linear accelerator.

FIGURE 1.3. Angle definitions and rotation directions for the gantry and couch rotation during linac-based radiosurgical procedures. In the single plane rotation, the couch is stationary at 0° and the gantry rotates from 0° to 360°, in the multiple converging arcs techniques a series of arcs is given each with a different stationary couch position, and in the dynamic rotation the gantry and couch rotate simultaneously and continuously, the gantry from 30° to 330° and the couch from 75° to -75°.

FIGURE 1.4. Example of a radiosurgical treatment in progress. The patient lies in a supine position on the linac couch, with the head hanging over the edge of the couch. The frame, in this case the OBT frame, is immobilized by means of the couch bracket. This ensures immobilization of the target with respect to the linac's isocenter. Both fiducial marker plates and target localization plates have been

removed to avoid interference with the radiation beam. The additional radiosurgical collimator is seen in the tray holder of the gantry. Couch and gantry are in the initial positions for the dynamic rotation technique, the gantry at 30°, the couch at 75°.

FIGURE 2.1. Schematic diagram of a typical isocentric linear accelerator showing the basic components.

FIGURE 2.2. Detailed schematic diagram of the linac head when operating in the photon mode.

FIGURE 2.3. Degrees of freedom for treatment set-up on a linear accelerator. The gantry rotates about a horizontal axis of rotation, the couch about a vertical axis and the collimator rotates about the beam axis. All axes of rotation intersect at the isocenter which is indicated by means of two side lasers and one ceiling laser.

FIGURE 2.4. Characteristic curves for radiographic film (Kodak XV II) used in our experiments. Optical density of irradiated films as measured with the RFA densitometer for different film batches is plotted against dose. The films were irradiated to different doses at a variety of depths in a polystyrene phantom.

FIGURE 2.5. Characteristic curves for radiographic film used in our experiments and measured with the digital video imaging system. Light intensity passing through the irradiated film and reaching the camera is related to a grey scale ranging from 0 to 250. The same film densities will result in different intensity readings for different lens aperture openings and camera magnifications. The films were irradiated to known doses in a polystyrene phantom at a depth of 2.5 cm.

FIGURE 3.1. Geometry of experimental set-up used in measurement of radiosurgical beam parameters. Shown is an example of an additional radiosurgical

field collimator and its positioning with respect to the machine collimator. Also shown is a tissue equivalent phantom at 100 cm from the target.

FIGURE 3.2. Tests to determine spatial accuracy of dose delivery in dynamic rotation radiosurgery. Part (a) is for single field data of vertical beams at isocenter. Superposition at isocenter of parallel-opposed fields for part (b) two vertical beams and part (c) two lateral beams. Part (d) is for the rotation of couch through 180° during irradiation at isocenter by a vertical beam. The tests are performed using film as a detector for a selection of treatment collimators used clinically at our center.

FIGURE 3.3. Alignment of several radiation fields defined by the 1 cm treatment collimator at isocenter. Part (a) alignment of two parallel-opposed vertical radiation fields and light field as indicated by a pin prick through the laser point marking the center of the light field. Parts (b), (c), and (d) show the alignment of four radiation fields. The film is placed at isocenter perpendicular to the vertical beam, parallel to the vertical beam and at a 45° angle to the vertical beam for films in parts (a), (b) and (c), respectively. The orientation of the film and the incident beams are shown schematically in the top portion of the figure.

FIGURE 3.4. Alignment of parallel-opposed vertical fields obtained with the 1 cm diameter treatment collimator shifted with respect to the laser indicated isocenter. Part (a): collimator is offset from central position by 0.5, 1 and 2 mm in the longitudinal direction, and part (b): collimator is offset by same amounts in the lateral direction.

FIGURE 3.5. Dose profiles as measured with a variety of detectors at a depth of 2.5 cm in a tissue equivalent phantom with a 10 mm diameter collimator in part (a) and a 30 mm diameter collimator in part (b).

FIGURE 3.6. Off-axis ratios measured with the digital imaging densitometry system at four depths in polystyrene phantom: 25 mm, 105 mm, 185 mm and 265 mm. Part (a) 10 mm diameter collimator and part (b) 30 mm diameter collimator.

FIGURE 3.7. Percentage depth doses measured with a variety of detectors in a tissue equivalent phantom for (a) 10 mm diameter collimator and (b) 30 mm diameter collimator.

FIGURE 3.8. Average percentage depth doses measured in a tissue equivalent phantom with a variety of detectors for several field sizes: 10 mm diameter collimator, 30 mm diameter collimator and a 10X10 cm^2 field.

FIGURE 3.9. Percentage depth doses for a 1 cm diameter collimator and a 10X10 cm^2 square field measured with a parallel plate ionization chamber in a polystyrene phantom at an SSD=100 cm. Shown is the build-up region for both fields from the surface of the phantom to a depth of 30 mm.

FIGURE 3.10. Depth of dose maximum plotted as a function of circular field diameter.

FIGURE 3.11. Percentage depth doses in the build-up region for an equivalent square field (17.7X17.7 mm^2) and a circular field (20 mm diameter) as measured with the parallel plate ionization chamber in a polystyrene phantom. Both fields have an area of 3.14 cm^2.

FIGURE 3.12. Compton differential scattering cross-section calculated for various incident photon energies as a function of electron scattering angle ϕ.

FIGURE 3.13. Compton differential scattering cross-section calculated for the

x-ray energy spectrum of a 10 MV linear accelerator as a function of electron scattering angle ϕ.

FIGURE 3.14. Probability per MeV that a Compton recoil electron scattered at a given angle ϕ will have a particular range R.

FIGURE 3.15. Schematic diagram explaining the observed shift in depth of dose maximum. Electrons are scattered at a most probable angle of ~8° with an average range of ~17 mm. In (a), (b), (c) and (d) as field size increases, the additional peripheral electrons contribute to the central axis dose, causing depth of dose maximum to increase. Yet if field size is further increased as in (e), the peripheral electrons will no longer have large enough range to reach the central axis, resulting in a saturation of the observed shift in d_{max}. The dashed horizontal line indicates the field size for each of the diagrams, and the solid vertical line represents the central axis.

FIGURE 4.1. Isodose distributions in three orthogonal planes (transverse, sagittal and coronal) for several treatment techniques, (a) single plane rotation, (b) 4 converging arcs, (c) 11 converging arcs and (d) dynamic rotation, as calculated for an 8 cm radius spherical tissue equivalent phantom with the 1 cm diameter collimator. Shown in each distribution are the 90%, 50%, 20%,10% and 5% isodose curves. In some cases the 5% and even the 10% isodose curves continue beyond the limits shown in the figures.

FIGURE 4.2. The steepest and shallowest dose fall-off curves for various linac-based radiosurgical techniques as calculated on a spherical phantom of radius 8 cm with the 1 cm diameter treatment collimator. Percentage doses are plotted as a function of distance, in mm, from the target center. All intermediate dose fall-offs lie in the shaded region between the two extreme curves. Shown are (a) single plane

rotation, (b) 4 converging arcs, (c) 11 converging arcs and (d) dynamic rotation.

FIGURE 4.3. The steepest and shallowest dose fall-off curves for various linac-based radiosurgical techniques as calculated on a spherical phantom of 8 cm radius with the 1 cm diameter collimator. The percentage doses are normalized to 100% at the isocenter and plotted as a function of distance from the target center. Curves (a) represent the steepest and shallowest fall-off for single plane rotation, curves (b) for 4 converging arcs, curves (c) for 11 converging arcs, curves (d) dynamic rotation and curves (e) for the Gamma unit (7). The curves are plotted on the same axes to facilitate comparison between dose fall-offs obtained with the various techniques.

FIGURE 4.4. The steepest and shallowest dose fall-off curves for various linac-based radiosurgical techniques as calculated on a spherical phantom of radius 8 cm with the 2 cm diameter treatment collimator. The percentage doses are normalized to 100% at the isocenter and plotted as a function of distance from the target center. All intermediate dose fall-offs lie in the shaded region between the two extreme curves. Shown are (a) single plane rotation, (b) 4 converging arcs, (c) 11 converging arcs and (d) dynamic rotation.

FIGURE 4.5. The steepest and shallowest dose fall-off curves for various linac-based radiosurgical techniques as calculated on a spherical phantom of radius 8 cm with the 3 cm diameter treatment collimator. The percentage doses are normalized to 100% at the isocenter and plotted as a function of distance from the target center. All intermediate dose fall-offs lie in the shaded region between the two extreme curves. Shown are (a) single plane rotation, (b) 4 converging arcs, (c) 11 converging arcs and (d) dynamic rotation.

FIGURE 5.1. Degrees of rotational freedom and definition of coordinate systems.

The XYZ coordinate frame is fixed in the treatment room with the origin at the isocenter. The X'Y'Z' is the coordinate frame fixed with respect to the couch and rotating with the couch through an angle ϕ in the XY plane about the Z axis. The X"Y"Z" frame is fixed in the gantry head, rotated through angle θ in the YZ plane about the X axis. Angle ψ gives the collimator rotation in the X"Y" plane about the Z" axis, which is also the beam axis. The triple primed frame X'''Y'''Z''' is the fixed frame rotated about this axis.

FIGURE 5.2. Results of a test to determine the spatial accuracy of the machine collimator rotation about the isocenter. The machine collimator was set to give a longitudinal opening of 3 cm and a lateral opening of 1 cm at the isocenter. The couch remained stationary, while the gantry rotated through 360°. The dose was delivered in 11 equal intervals along the gantry's path. Part (a): dose distribution of a lateral cross-section of the cylinder as measured in the transverse (Y'Z') plane. Parts (b) and (c) show longitudinal cross-sectional views as measured in the sagittal (X'Z') and coronal (X'Z') planes, respectively. Measurements were made on a spherical phantom of radius 8 cm, using film as a detector.

FIGURE 5.2. Results of a test to determine the spatial accuracy of the machine collimator rotation about the isocenter. The machine collimator was set to give a longitudinal opening of 3 cm and a lateral opening of 1 cm at the isocenter. The couch remained stationary, while the gantry rotated through 360°. The dose was delivered in 11 equal intervals along the gantry's path. Part (a): dose distribution of a lateral cross-section of the cylinder as measured in the transverse (Y'Z') plane. Parts (b) and (c) show longitudinal cross-sectional views as measured in the sagittal (X'Z') and coronal (X'Z') planes, respectively. Measurements were made on a spherical phantom of radius 8 cm, using film as a detector.

FIGURE 5.4. Dose distributions obtained by irradiating a tilted cylindrical target

with a longitudinal axis oriented along a vector pointing from the origin to (0.75,0.75,1.1) in couch frame of reference with the origin corresponding to the target center. The target of diameter 1 cm and length 3 cm was irradiated with the cylindrical dynamic rotation technique utilizing the gantry, couch and collimator rotation, as well as adjustable collimator longitudinal opening. The dose was delivered in 11 equal intervals along the gantry's path of rotation. Part (a): dose distribution of a lateral cross-section of the cylinder as measured in a plane tilted 45° with respect to the transverse plane (Y'cos45° Z') . Parts (b) and (c) show longitudinal cross-sectional views as measured in planes tilted by 45° from the sagittal plane (X'cos45° Z') and coronal plane (X'cos45° Y'), respectively. Measurements were made on a spherical phantom of radius 8 cm, using film as a detector.

FIGURE 5.5. Dose distribution obtained by irradiating a tilted cylindrical target with a longitudinal axis oriented along a vector pointing from the origin to (0.75,0.75,1.1) in the couch frame of reference with the origin corresponding to the target center. The target of diameter 1 cm and length 3 cm was irradiated with the cylindrical dynamic rotation technique utilizing the gantry, couch and collimator rotation, as well as adjustable collimator longitudinal opening. The dose was delivered in 11 equal intervals along the gantry's path of rotation. Part (a): dose distribution as measured in the transverse plane of the couch (Y'Z'). Part (b) :dose distribution as measured in the coronal plane of the couch (X'Y'). Measurements were made on a spherical phantom of radius 8 cm using film as a detector.

LIST OF TABLES

TABLE 3.1 The relative contributions to scatter into various components, relative dose factor, collimator factor and scatter factor for different radiosurgical field sizes. Data for a standard 10x10 cm^2 radiotherapy field is included for comparison.

TABLE 3.2 Depth of dose maximum measured in a tissue equivalent phantom with a parallel plate ionization chamber for several radiosurgical field sizes. The depth of dose maximum for the 10x10 cm^2 field is included for comparison.

TABLE 4.1. Minimum and maximum dose fall-off distances in mm from 90% isodose surface to 50%, 20% and 10% isodose surfaces as calculated with the treatment planning system for single plane rotation, 4 converging arcs, 11 converging arcs and dynamic rotation. The calculations were done on a spherical phantom of radius 8 cm with (a) the 1 cm diameter collimator, (b) 2 cm diameter collimator and (c) 3 cm diameter collimator. In some cases, for the single plane rotation, maximum dose fall-offs extend beyond the range of the calculated distribution and are therefore not available.

BIBLIOGRAPHY

Arcovito, G., Piermattei, A., D'Abramo, G. and Bassi, F.A., **Dose measurements and calculations of small radiation fields for 9-MV x-rays,** Med. Phys. **12**: 779-784, 1985. (66)

Attix, F.H., **Introduction to radiological physics and radiation dosimetry,** John Wiley & Sons, Toronto, 1986. (28)

Betti, O.O. and Derchinsky, V.E., **Hyperselective encephalic irradiation with linear accelerator,** Acta Neurochir. **33**: 385-390, 1984. (5, 10)

Biggs, P.J. and Ling, C.C., **Electrons as the cause of the obseved d_{max} shift with field size in high energy photon beams,** Med. Phys. **6**: 291-295, 1979. (61)

Cheirego, G., Marchetti, C., Avanzo, R.C., Pozza, F. and Colombo, F., **Dosimetric considerations on multiple arc stereotaxic radiotherapy,** Radiotherap. and Oncology **12**: 141-152, 1988. (10)

Colombo, F., Benedetti, A., Pozza, F., Avanzo, R.C., Chierego, C., Marchetti, C. and Zanardo, A., **External stereotactic irradiation by linear accelerator,** Neurosurgery **16**:154-160, 1985. (10)

Curry, T.S., Dowdey, J. E. and Murry, R. C., **Christensen's introduction to the physics of diagnostic radiology,** 3rd edition, Lea & Febiger, Philadelphia, 1984. (28)

Dahlin, H. and Sarby, B., **Destruction of small intracranial tumours with ^{60}Co gamma irradiation,** Acta Radiol. TPB **14**: 209-227, 1975. (7, 42)

Fabricant, J.I., Lyman, J.T. and Hosobuchi, Y., **Stereotactic heavy-ion Bragg peak radiosurgery for intra-cranial vascular disorders: method for treatment of deep arteriovenous malformations,** Brit. J. Radiol. **57**: 479-490, 1984. (93)

Goldstein, H., **Classical Mechanics,** 2nd edition, Addison-Wesley Publishing

Company, Inc., Reading, Massachusettes, 1980. (100)

Hartmann, G.H., Schegel, W., Sturm, V., Kober, B., Pastyr, O. and Lorenz, W.J., **Cerebral radiation surgery using moving field irradiation at a linear accelerator facility**, Int. J. Radiat. Oncol. Biol. Phys. **11**: 1185-1192, 1985. (10)

Hartmann, G.H., Schlegel, W., Sturm V. and Lorenz, W.J., **A fast algorithm to calculate three dimensional dose distributions for radiosurgery**, in "Proceedings of the eighth international conference on the use of computers in radition therapy", IEEE Computer Society Press, Silver Springs, MD, 1984. (10)

Houdek, P.V., Fayos, J.V., Van Buren, J.M. and Ginsberg, M.S., **Stereotaxic radiotherapy technique for small intracranial lesions**, Med. Phys. **12**: 469-472, 1985. (10)

Johns, H. and Cunningham, J. R., **The physics of radiology**, 4th edition, Charles C. Thomas, Springfield, Illinois, 1983. (33, 54, 67)

Khan, F.M., Sewchand, W., Lee, J. and Williamson, J.F., **Revision of tissue-maximum ratio and scatter-maximum ratio concepts for cobalt 60 and higher energy x-ray beams**, Med. Phys. **7**: 230-237, 1980. (57)

Karzmark, C.J. and Morton, R.J., **A primer on theory and operation of linear accelerators in radiation therapy**, U.S. Department of Health and Human Services, Food and Drug Administration, Bureau of Radiological Health, Rockville, Maryland, 1981. (22)

Kjellberg, R.N., Sintani, A., Frantz, A.G. and Kliman, B., **Proton beam therapy in acromegaly**, N. Engl. J. Med. **278**: 689-695, 1968. (3)

Larsson, B., Leksell,L., Rexed, B., Sourander, P., Mair W. and Anderson, B., The **high energy proton beam as a neurosurgical tool**, Nature **182**: 1222-1223, 1958. (3)

Larsson, B., Liden, K. and Sarby, B., **Irradiation of small structures through intact skull**, Acta Radiol. TPB **13**: 513-534, 1974. (3)

Lawrence, J.H., Tobias, C.A., Born, J.L., Wang C. and Linfoot, J.A., **Heavy-particle irradiation in neoplastic and neurologic disease**, J. Neurosurg. **19**: 717-722, 1962. (3)

Leksell, L., **The stereotaxis method and radiosurgery of the brain**, Acta Chir. Scan. **102**: 316-319, 1951. (3)

Leksell, L., **Gezielte Hirnoperationen**, in Handbuch der Neurochirurgie, (vol. VI) Olivecrona, H. and Tonnis, W. editors Springer Verlag, New York, 1957. (3)

Leksell, L., **Cerebral radiosurgery I Gamma thalamotomy in two cases of intractable pain**, Acta Chir. Scan. **134**: 385-395, 1968. (3)

Lutz, W., Winston, K.R. and Maleki, N., **A system for stereotactic radiosurgery with a linear accelerator**, Int. J. Radiat. Oncol. Biol. Phys. **14**: 373-381, 1988. (12)

Marbach, J.R. and Almond, P.R., **Scattered photons as the cause for the observed d_{max} shift with field size in high-energy photon beams**, Med. Phys. **4**:310-314, 1977. (61)

McGinley, P.H., Butker, E.K., Crodker, I.R. and Landry, J.C., **A patient rotator for stereotactic radiosurgery**, Phys. Med. Biol. **35**: 649-657, 1990. (5)

Milan, J. and Bentley, R.E., **The storage and manipulation of radiation dose data in a small digital computer**, Brit. J. Radiol. **47**:115-117, 1974.

Mohan, R., Chui, C. and Lidofsky, L., **Energy and angular distributions of photons from medical linear accelerators**, Med. Phys. **12**:592-597, 1985. (60, 68)

Olivier, A., Peters, T.M. and Bertrand, G., **Stereotaxic systems and apparatus for use with MRI, CT, and DSA**, Appl. Neurophysiol. **48**: 94-96, 1986. (80)

Pastyr, O., Hartmann, G.H., Schlegel, W., Schabbert, S., Treuer, H., Lorenz, W.J. and Sturm, V., **Stereotactically guided convergent beam irradiation with a linear accelerator: localization-technique**, Acta Neurochir.

(Wien) **99**: 61-64, 1989. (5)

Peters, T.M., Clark, J.A., Olivier, A., Marchand, A.P., Mawko, G., Dieumegarde, M., Muresan, L.V. and Ethier, R., **Integrated stereotaxic imaging with CT, MR imaging and Digital Subtraction Angiography**, Radiology **161:** 821-826, 1986. (4, 5, 42, 80)

Phillips, M.H., Frankel, K.A., Lyman, J.T., Fabrikant, J.I. and Levy, R.P, **Comparison of different radiation types and irradiation geometries in stereotactic radiosurgery**, Int. J. Radiat. Oncol. Biol. Phys. **18**: 211-220, 1990. (21)

Pike, G.B., Podgorsak, E.B., Peters, T.M. and Pla, C., **Dose distributions in dynamic stereotactic radiosurgery**, Med. Phys. **14**:780-789, 1987. (78, 79, 81, 92)

Pike, G.B., Podgorsak, E. B., Peters, T.M., Pla, C., Olivier, A. and Souhami, L., **Dose distributions in radiosurgey**, Med. Phys. **17**: 296-304, 1990. (78)

Podgorsak, E.B., Olivier, A., Pla, M., Lefebvre, P.Y. and Hazel, J., **Dynamic stereotactic radiosurgery**, Int. J. Radiat. Oncol. Biol. Phys. **14**:115-125, 1988. (10, 12)

Podgorsak, E.B., Olivier, A., Pla, M., Hazel, J., de Lotbinière, A. and Pike, G.B., **Physical aspects of dynamic stereotactic radiosurgery**, Appl. Neurophysiol. **50**: 63-68, 1987. (12)

Podgorsak, E.B., Pike, G.B., Olivier, A., Pla, M. and Souhami, L., **Radiosurgery with high energy photon beams: a comparison among techniques**, Int. J. Radiat. Oncol. Biol. Phys. **16**: 857-865, 1989. (82, 87)

Podgorsak, E.B., Pike, G.B., Pla, M., Olivier, A. and Souhami, L., **Radiosurgery with photon beams: physical aspects and adequacy of linear accelerators**, Radiotherapy and Oncology **17**: 349-358, 1990. (43)

Rice, R.K., Hansen, J.L., Svensson, G.K. and Siddon, R.L., **Measurements of dose distributions in small beams of 6 MV x-rays**, Phys. Med. Biol. **32**: 1087-1099, 1987. (66)

Siddon, R.L. and Barth, N.H., **Stereotaxis localization of intracranial targets,** Int. J. Radiat. Oncol. Biol. Phys. **13**:1241124-6, 1987. (5)

Walton, L., Bomford, C.K. and Ramsden, D., **The Sheffield stereotactic radiosurgery unit: physical characteristics and principles of operation,** Brit. J. Radiol. **60**: 897-906, 1987. (7, 42, 84, 86)

Winston, K.R. and Lutz, W., **Linear accelerator as a neurosurgical tool for stereotactic radiosurgery,** Neurosurg. **22**: 454-464, 1988. (12)

Wyckoff, H.O., Chairman, **Stopping powers for electrons and positrons,** ICRU report 37, 1984. (70)